

EARTHQUAKE-INDUCED GROUND DEFORMATION EFFECTS ON BURIED  
PIPELINES

A Dissertation

Presented to the Faculty of the Graduate School  
of Cornell University

In Partial Fulfillment of the Requirements for the Degree of  
Doctor of Philosophy

by

Dimitra Bouziou

January 2015

© 2015 Dimitra Bouziou  
ALL RIGHTS RESERVED

# EARTHQUAKE-INDUCED GROUND DEFORMATION EFFECTS ON BURIED PIPELINES

Dimitra Bouziou, Ph. D.

Cornell University 2015

The primary subject of this thesis is the evaluation of pipeline performance during earthquakes through analytical and experimental studies, spatial analysis, and probabilistic methodologies. Permanent ground deformations caused by liquefaction are also addressed through spatial and statistical analysis, and are compared to foundation deformations caused by liquefaction effects estimated through building damage surveys.

This thesis starts with a comprehensive analytical and experimental assessment of segmented pipeline response to transient ground deformation before and after rehabilitation with in situ lining technologies. The different modes of segmented pipeline deformation caused by seismic wave propagation are investigated through finite element analyses to show that the most prominent form of deformation at weak pipeline joints and circumferential pipe cracks are in the axial direction. They exceed the levels of all other forms of pipeline deformation by several orders of magnitude. Nonaxial deformations have negligible effects on pipeline performance under seismic body wave propagation. Pipeline performance after rehabilitation with in situ linings is studied through large-scale testing and the effectiveness of in situ lining technology for seismic retrofit of critical lifelines is evaluated.

Pipeline performance during earthquakes is also investigated through spatial analysis of the Christchurch water distribution system response to transient and permanent ground deformations during the 22 February 2011 Christchurch earthquake, New Zealand (NZ). Repair regressions for different pipe types are developed using spatial data sets that are unique in size and complexity, including dense array ground motion records, detailed mapping of areas affected by soil liquefaction, as well as spatial data sets for the water distribution system, geocoded repair records, and high resolution Light Detection and Ranging (LiDAR) measurements of vertical and horizontal movements. This study expands on previous work in several important ways, and provides a detailed framework of the analytical processes for repair regressions that assists in future investigations with data of similar size and complexity.

A probabilistic model is presented in which the expected value of the ground strain in the axial pipeline direction within a strain field is calculated by assuming that pipeline orientation with respect to the strain field is uniformly distributed and by accounting for possible differences in tensile and compressive strains with a weighting factor. The proposed methodology is applied in regression analysis of pipeline damage caused by lateral ground strains during the 22 February 2011 Christchurch earthquake, NZ, and can be used for future investigations to improve the assessment of ground strains affecting segmented pipelines.

Permanent ground deformation during the 2010-2011 Canterbury Earthquake Sequence, NZ, is evaluated through statistical analysis of vertical and lateral ground displacements, as well as differential vertical displacements and lateral ground strains, calculated from high resolution LiDAR surveys. Ground deformation patterns are

identified with respect to topographic characteristics through the use of LiDAR ground displacement measurements. Foundation deformations caused by liquefaction effects are estimated using damage survey data in residential properties in Christchurch and are evaluated with respect to liquefaction-induced ground deformations.

## BIOGRAPHICAL SKETCH

Dimitra Bouziou was born in Athens, Greece, on April 1986, to parents Ioannis Bouzios and Alexandra Bouziani. After graduating from the 2<sup>nd</sup> Unified Upper Secondary School in Sparta, Greece, she attended the School of Civil Engineering in the National Technical University of Athens, Greece, where she received a Diploma in Civil Engineering in July 2010. She joined the M.S./Ph.D. program in Civil and Environmental Engineering at Cornell University in August 2010, where she earned a Master of Science in January 2013.

Dr. Bouziou pursued her doctoral studies within the Geotechnical Group at the School of Civil and Environmental Engineering at Cornell University, with minors in Geotechnical Engineering, Structural Mechanics, and Advanced Composite Structures. During her doctoral studies at Cornell University, she worked as a graduate research assistant under the supervision of Thomas R. Briggs Professor Thomas D. O'Rourke and as a teaching assistant in the School of Civil and Environmental Engineering.

Dr. Bouziou has presented her research at the 15<sup>th</sup> World Conference in Earthquake Engineering (2012) and the Quake Summit 2012. She is working as a geotechnical engineer at Edafos Consulting Engineers S.A. in Athens, Greece.

*To my family*

*“Earthquakes move mountains. But so do imagination and ingenuity — when matched with implementation.”*

*Charles Richter*

## ACKNOWLEDGEMENTS

This dissertation would not have been made possible without the invaluable and continuous contribution of Thomas R. Briggs Professor Thomas D. O'Rourke. Professor O'Rourke's guidance during my studies at Cornell University helped me overcome the difficulties and complete the research related to this dissertation. I am sincerely grateful for Professor O'Rourke's support as an advisor and as a Special Committee Chair. The experience and knowledge I have gained during my studies under his supervision are the most valuable assets I am taking with me as I depart from Ithaca.

During my work as a graduate research assistant at the George E. Brown Jr. Network for Earthquake Engineering Simulation (NEES) facility at Cornell University, I had the chance to collaborate with Professor Harry E. Stewart, Tim Bond, Brad Wham, Michael Wickham, Joe Chipalowski, Michael Palmer, and the undergraduate students at Cornell University, as well as with Professor Andre Filiatrault, Professor Amjad Aref and Zilan Zhong from the University at Buffalo, all of which coordinated and/or participated in our NEES research projects. I would like to thank all the aforementioned faculty, students and staff for the productive teamwork and their help during my studies.

I would also like to express my profound gratitude to Professor Steve DeGloria for his unconditional help in my effort to become familiar with spatial analysis and for his reviews on my work related to Geographic Information Systems (GIS) and included in this dissertation. Special thanks to Mr. Stephen Smith and Professor D.G. Rossiter from the Crop and Soil Sciences Section for their valuable guidance in resolving

problems during my work related to GIS. I am truly grateful for having worked with Professor Sang Soo Jeon and Professor Selcuk Toprak. Their help and advice played an important role in my work related to GIS and kept me motivated and productive.

I would like to thank the members of my Special Committee, Professor Mircea D. Grigoriu, Professor Stuart L. Phoenix, and Professor Amjad J. Aref for their continuous support during my research as a Ph.D. candidate. I would also like to express my appreciation to the staff and faculty at the School of Civil and Environmental Engineering at Cornell University for their support during my studies and for offering me the opportunity to work as a teaching assistant in 2010-2011.

I was privileged to have Christina Argyrou as an office mate during my years at Cornell. She provided me support and help, and I am thankful for her friendship and understanding during my hardest times. I am also sincerely thankful for being surrounded by the Greek community in Ithaca and by all the members of Greeks@Cornell, especially Theo, who were my second family in Ithaca.

I truly appreciate the financial support for my graduate research assistantships that I received from the National Science Foundation (NSF) through NEES and Rapid Response Research (RAPID).

George was my anchor during the last and hardest year of my studies, his devoted love and concern helped me overcome the greatest difficulties upon completion of this dissertation. I am deeply thankful for his presence in my life during this hard period.

The love and support of my family have been the most important driving forces throughout my studies. I reserve my most heartfelt gratitude and appreciation for my parents, Alexandra and John, and my brother Nick, who have been always by my side reminding me the most important principles in life and keeping me healthy and strong.

## TABLE OF CONTENTS

<b>INTRODUCTION .....</b>	<b>1</b>
1.1 Overview .....	1
1.2 Motivation of Study.....	2
1.3 Objectives.....	4
1.3.1 Seismic Evaluation of In Situ Linings .....	5
1.3.2 Evaluation of Water Distribution System Performance During Earthquakes.....	5
1.3.3 Probabilistic Approach to Axial Pipeline Strain.....	6
1.3.4 Statistical Evaluation of LiDAR Ground Movements .....	7
1.4 Scope and Organization.....	7
REFERENCES .....	9
<b>SEISMIC BODY WAVE INTERACTIONS WITH BURIED PIPELINES BEFORE AND AFTER REHABILITATION WITH IN SITU LININGS.....</b>	<b>13</b>
Abstract.....	13
2.1 Introduction .....	14
2.2 Body Wave Effects on Pipelines .....	17
2.3 Modeling Methodology .....	21
2.4 Numerical Analysis of Pipeline Response Before Rehabilitation.....	23
2.4.1 Axial Pipeline Deformation .....	23
2.4.2 Transverse Lateral and Vertical Pipeline Deformation.....	26
2.4.3 Transverse Lateral and Vertical Pipeline Rotation .....	29
2.4.4 S-Wave Effects on Pipelines for the Highest Recorded Levels of PGV and PGA.....	31
2.5 Numerical Analysis of Pipeline Response After Rehabilitation .....	34
2.6 Experimental Evaluation of CIPP Seismic Performance .....	39
2.7 Conclusions .....	44
REFERENCES .....	47
<b>WATER DISTRIBUTION SYSTEM RESPONSE TO THE 22 FEBRUARY 2011 CHRISTCHURCH EARTHQUAKE .....</b>	<b>50</b>
Abstract.....	50
3.1 Introduction .....	51
3.2 GIS Database .....	53
3.2.1 Strong Motion Datasets.....	54
3.2.2 Areas of Liquefaction.....	55
3.2.3 High Resolution LiDAR Datasets.....	56
3.2.4 Pipeline Repair Datasets .....	57
3.3 Spatial Analysis of Water Pipeline Damage .....	59
3.4 Screening Criteria.....	61

3.5 Analytical Process for Peak Ground Velocity.....	63
3.6 Analytical Process for Differential Vertical Ground Movement .....	66
3.7 Analytical Process for Lateral Ground Strain .....	71
3.8 Combined Effects of Differential Vertical Ground Movement and Lateral Ground Strain .....	77
3.9 Conclusions .....	79
REFERENCES .....	83
<b>A PROBABILISTIC APPROACH TO AXIAL PIPELINE STRAIN CAUSED BY PERMANENT GROUND DEFORMATIONS.....</b>	<b>86</b>
Abstract.....	86
4.1 Introduction .....	87
4.2 Background.....	88
4.3 Axial Ground Strain Affected by Pipeline Orientation .....	91
4.4 Geospatial Data for the 22 February 2011 Christchurch Earthquake.....	96
4.5 Regression Analysis with Expected Value of Ground Strain.....	100
4.6 Combined Effects of Expected Value of Lateral Ground Strain and Differential Vertical Ground Movement.....	103
4.7 Conclusions .....	107
REFERENCES .....	110
<b>EVALUATION OF GROUND DEFORMATIONS DURING THE 2010-2011 CANTERBURY EARTHQUAKE SEQUENCE.....</b>	<b>113</b>
Abstract.....	113
5.1 Introduction .....	114
5.2 LiDAR Data.....	116
5.3 Study Area .....	119
5.4 Statistical Screening for Ground Deformation Patterns .....	122
5.5 Probability Distributions .....	125
5.6 Ground Angular Distortion and Vertical Movement.....	126
5.7 Lateral Ground Movement and Lateral Ground Strain .....	130
5.8 LiDAR-Based Ground Deformations vs Foundation Deformations .....	134
5.9 Conclusions .....	142
REFERENCES .....	145
<b>CONCLUSIONS AND RECOMMENDATIONS .....</b>	<b>149</b>
6.1 Seismic Wave Interactions with Buried Pipelines Before and After Rehabilitation With In Situ Linings .....	149
6.2 Regression Analysis of Pipeline Damage During the 22 February 2011 Christchurch Earthquake .....	151
6.3 Probabilistic Approach to Axial Pipeline Strain Caused by Permanent Ground Deformations .....	153

6.4 Statistical Analysis of Ground Deformations During the 2010-2011 Canterbury Earthquake Sequence.....	154
--	-----

**APPENDIX A**

Repair Rate (RR) Correlations with the Geometric Mean Peak Ground Velocity (GMPGV)

**APPENDIX B**

Repair Rate (RR) Correlations with Ground Angular Distortion  $\beta$

**APPENDIX C**

Repair Rate (RR) Correlations with Lateral Ground Strain  $\epsilon_{HP}$

**APPENDIX D**

Contour Plots of Differential Vertical Displacement

## LIST OF ABBREVIATIONS

AAM	AAM Brisbane
AC	Asbestos cement
ALA	American Lifelines Association
CBD	Central Business District
CCC	Christchurch City Council
CERA	Canterbury Earthquake Recovery Authority
CES	Canterbury Earthquake Sequence
CI	Cast Iron
CIPP	Cast -In-Place Pipe
DCDT	Direct Current Displacement Transducer
DEM	Digital Elevation Model
DI	Ductile Iron
EW	East-West
FE	Finite Element
FRP	Fiber Reinforced Polymer
GEV	Generalized Extreme Value
GIS	Geographic Information Systems
GMPGV	Geometric Mean Peak Ground Velocity
GPS	Global Positioning System
ITI	Insituform Technologies, Inc.
LADWP	Los Angeles Department of Water and Power
LiDAR	Light Detection And Ranging
LINZ	Land Information New Zealand

MMI	Modified Mercalli Intensity
MPVC	Modified Polyvinyl Chloride
NZAM	New Zealand Aerial Mapping
NZ	New Zealand
NS	North-South
PEER	Pacific Earthquake Engineering Research
PGA	Peak Ground Acceleration
PGD	Permanent Ground Deformation
PGV	Peak Ground Velocity
PVC	Polyvinyl Chloride
RR	Repair Rate
SCIRT	Stronger Christchurch Infrastructure Rebuild Team
SEESL	Structural Engineering and Earthquake Simulation Laboratory
TGD	Transient Ground Deformation
T&T	Tonkin and Taylor
UB	University at Buffalo

## LIST OF SYMBOLS

$A$		horizontal ground acceleration
$A_a^y$	apparent horizontal ground acceleration perpendicular to pipeline axis	
$A^z$		vertical ground acceleration
$A_p$		pipe cross sectional area
$A_{IMain}$		IMain® liner cross sectional area
$A_{Starline}$		Starline2000® liner cross sectional area
$C$		wave propagation velocity
$C_a^x$	apparent wave propagation velocity parallel to pipeline axis	
$D$		pipe outer diameter
$d_x$		maximum axial joint offset
$d_y$		maximum transverse lateral joint offset
$d_z$		maximum transverse vertical joint offset
$E_p$		pipe Young's modulus
$E_{IMain}$		IMain® liner Young's modulus
$E_{Starline}$		Starline2000® liner Young's modulus
$f$	axial shear resistance between pipe and soil per unit length	
$f(\theta)$		probability density function of $\theta$
$k$	weighting factor for joint resistance to tension and compression	
$K_g^{xy}$		horizontal ground curvature
$K_g^{xz}$		vertical ground curvature
$l_{12}$		horizontal distance between points 1 and 2

$M_w$	earthquake moment magnitude
$N_{qh}$	maximum dimensionless soil lateral force
$N_{qv}$	maximum dimensionless soil upward movement force
$p$	actual number of repairs
$p_w$	internal water pressure
$P_u^x$	peak joint axial pullout force
$r^2$	coefficient of determination
$t$	pipe wall thickness
$t_m$	time
$V$	particle velocity
$V_a^x$	apparent horizontal ground particle velocity parallel to pipeline axis
$V_a^y$	apparent horizontal ground particle velocity perpendicular to pipeline axis
$V^z$	vertical ground particle velocity
$X$	distance
$x$	sampling length
$z_p$	pipe cross sectional area
$\alpha$	fraction of actual pipe repairs
$\beta$	angular distortion
$\beta_c$	confidence interval
$\gamma$	soil unit weight
$\gamma_g^y$	horizontal ground shear strain perpendicular to pipeline axis
$\gamma_g^z$	vertical ground shear strain perpendicular to pipeline axis
$\gamma_{GEV}$	shape parameter for generalized extreme value distribution

$\gamma_i$	wave angle of incidence
$\gamma_{xy}$	shear strain in the xy-plane
$\delta z_1$	vertical movement at point 1
$\delta z_2$	vertical movement at point 2
$\varepsilon$	net strain in the ground parallel to the pipeline
$\varepsilon_e$	expected value of ground strain
$\varepsilon_{HPB}$	absolute maximum value of foundation lateral strain
$\varepsilon_{HP}$	absolute maximum value of lateral ground strain
$\varepsilon_m$	mean strain
$\varepsilon_g^x$	ground strain parallel to pipeline axis
$\varepsilon_p^x$	pipe axial strain
$\varepsilon_u^x$	peak joint pullout strain
$\varepsilon_x$	lateral strain in the x-direction
$\varepsilon_y$	lateral strain in the y-direction
$\varepsilon_{1,2}$	principal strains
$\theta$	pipeline orientation with respect to principal strain field
$\theta_{xy}$	maximum lateral joint rotation
$\theta_{xz}$	maximum vertical joint rotation
$\theta_1$	pipeline orientation with respect to principal strain field at which the net strain is zero
$\mu$	mean
$\mu_{GEV}$	location parameter for generalized extreme value distribution
$\sigma$	standard deviation

$\sigma_{\text{GEV}}$	scale parameter for generalized extreme value distribution
$\varphi$	soil effective friction angle
$\varphi^{-1}(\beta_c)$	standard normal deviate

# CHAPTER 1

## INTRODUCTION

### 1.1 Overview

Pipeline networks are key assets of critical infrastructure and their protection is essential for public health, safety and economic well-being. Water distribution systems, in particular, are critical for fire protection, drinking and sanitary purposes, domestic and industrial activities, irrigation, hydropower and recreation. Their serviceability and resilience are important within any modern society, and critical for emergency services and community recovery in response to natural hazards.

Earthquake damage to water distribution systems is caused by transient ground deformation (TGD) or permanent ground deformation (PGD), or both. PGD is associated with ground movements that are permanent and usually generated by ground failure, but also by more moderate shear and volumetric soil strains that lead to irreversible deformation [1.1]. Earthquake-induced PGD is caused by surface faulting, liquefaction, landslides, tectonic uplift and subsidence, and soil densification [1.2] [1.3] [1.4]. PGD hazards generally affect smaller geographical areas than TGD hazards, but result in locally higher damage rates for water distribution systems [1.5] [1.6]. PGD, especially liquefaction-induced lateral and vertical ground movements, are the most prevalent causes of pipeline damage during earthquakes [1.7] [1.8] [1.9]. Numerous investigators have studied the effects of large lateral and vertical ground

movements induced by liquefaction on lifelines and buildings [1.7] [1.9] [1.10] [1.11] [1.12].

TGD is associated with seismic wave propagation and results in smaller ground strains relative to those generated by PGD. TGD can cause soil cracks and fissures triggered by pulses of strong motion that exceed the soil shear strength near the ground surface [1.2]. The residual deformation after shaking has stopped is normally less than the maximum TGD during the event.

The principal causes and types of TGD and PGD have been summarized by Bird et al. [1.3]. There are certain cases where the magnitude of TGD has a significant effect on pipeline system integrity such as surface wave propagation in large sedimentary basins, valley vibration effects, and ground oscillation in liquefiable soil [1.3] [1.13]. TGD generally affects larger areas than PGD and, hence, the overall extent of pipeline damage due to TGD can be of equal or greater significance to the more severe and local damage caused by PGD [1.4] [1.7]. The geographic variability of damage requires that pipeline response to earthquakes be evaluated at both the component and systems level of performance [1.6] [1.14].

## **1.2 Motivation of Study**

Over the past two decades in situ pipe lining technologies have evolved into a well-established industry that increases the service life of existing utilities without

expensive and disruptive excavation and replacement [1.15] [1.16] [1.17]. The methodology involves the installation of polymeric linings remotely inside existing, underground pipelines with minimum disturbance to the surrounding infrastructure through trenchless construction procedures [1.15] [1.18] [1.19] [1.20]. The linings allow continuity of pipeline flow, prevent leakage and soil intrusion, and provide variable degrees of structural reinforcement. The capability of in situ pipe linings to support structurally deteriorated pipelines is particularly beneficial for seismic retrofit [1.21] [1.22]. However, the lack of experimental and analytical evaluation of this technology is a barrier against its use for seismic reinforcement of underground infrastructure. Although empirical approaches can be incorporated into the rehabilitation of existing pipelines, as proposed by Eiding et al. [1.11], experimental and analytical research focused on the seismic performance of pipelines rehabilitated with in situ linings is needed to quantify the level of improved seismic performance.

To improve the seismic performance of pipelines using in situ linings or any rehabilitation technique, in general, apart from experimental and analytical research, it is also important to develop an understanding of pipeline network vulnerability to earthquakes. The collection of information about pipeline damage during earthquakes provides for improved understanding of pipeline performance, and by extension, supports the effective use of in situ pipeline rehabilitation for seismic retrofit. Remote sensing technologies, in particular, such as Light Detection and Ranging (LiDAR), and Geographic Information Systems (GIS), in combination with field reconnaissance,

allow for collection and analysis of geographically distributed information about the response of lifeline systems to extreme events.

Airborne and terrestrial LiDAR has been used extensively for monitoring and evaluating ground displacements caused by natural hazards such as earthquakes, floods, landslides and debris flows [1.23] [1.24] [1.25] [1.26]. LiDAR data also help with the assessment of spatially distributed pipeline damage and allow for the development of pipeline fragility relationships. The use of LiDAR data for spatial analysis of pipeline damage, in particular, requires LiDAR surveys of high resolution and accuracy, resulting in data collections of large size and complex analytical processes. Therefore, it is important to develop methodologies for systematic documentation and efficient manipulation of large and complex data sets that assist in future investigations of the distribution of pipeline damage.

### **1.3 Objectives**

The principal goals of this thesis are to evaluate the seismic performance of pipelines reinforced with in situ polymeric linings; analyze the performance of the Christchurch, New Zealand (NZ), water distribution system in response to the 2010-2011 Canterbury Earthquake Sequence (CES); develop and evaluate a probabilistic approach for characterizing pipeline performance that accounts for orientation within earthquake-induced ground strain fields; and perform a statistical assessment of

ground movements measured by high resolution LiDAR surveys during the CES. These research objectives are discussed under the subheadings that follow.

### **1.3.1 Seismic Evaluation of In Situ Linings**

One of the principal objectives is the evaluation of in situ lining technology for seismic retrofit of existing pipelines through experimental and analytical investigations. The effects of TGD on aging pipelines, which have lost structural integrity, are explored through numerical simulation to determine the most prominent form of pipeline deformation. The response of pipelines rehabilitated with in situ linings is investigated through numerical modeling and experimental simulations. The results allow for the comparison of pipeline response before and after rehabilitation as well as the quantification of their effectiveness for seismic retrofit.

### **1.3.2 Evaluation of Water Distribution System Performance During Earthquakes**

The seismic performance of water distribution systems is evaluated through spatial analysis with Geographical Information Systems (GIS). Pipeline damage due to PGD and TGD during the 22 February 2011 Christchurch earthquake, NZ, is assessed using geospatial data of unprecedented size and complexity, collected during the CES. Screening criteria are developed for selecting statistically robust data used in linear regressions between pipeline repair rates (repairs/km) and both TGD and PGD.

The regression analyses are used to quantify the relative performance of different types of pipelines under different levels of earthquake-induced ground deformation. The use of GIS in the analytical process is described in detail to assist in future investigations with data sets of similar size and complexity.

### **1.3.3 Probabilistic Approach to Axial Pipeline Strain**

Previous methods for pipeline repair correlation with ground strain that use damage statistics, ground motion records, and ground deformation measurements from previous earthquakes do not account for the orientation of the pipeline within the earthquake-induced lateral ground strain field. The expected value of ground strain in the axial direction of the pipeline is derived by assuming a uniform distribution of pipeline orientation with respect to the strain field. Data from LiDAR ground surface measurements acquired before and after the 22 February 2011 Christchurch earthquake, NZ, are used in combination with geocoded repair records for the Christchurch water distribution system to develop linear regressions of pipeline repair rate with respect to the expected value of axial ground strain. The relative vulnerability of different types of pipelines to tensile and compressive ground strain is also explored through the proposed probabilistic approach.

### **1.3.4 Statistical Evaluation of LiDAR Ground Movements**

An analysis is performed to determine the statistical characteristics of lateral and vertical ground displacements, lateral ground strains, and differential vertical ground deformations derived from LiDAR surveys in Christchurch, NZ. The results from the statistical analyses are used to identify the locations of highest ground deformation and investigate their relationship with respect to landforms and water courses within and adjacent to the Christchurch flood plain. The statistical analyses are also used to identify mathematical expressions that best describe the distributions.

Data from detailed damage surveys of 12 residential properties in Christchurch are used to evaluate foundation damage, expressed as lateral strain at concrete perimeter footings and differential vertical ground floor displacement, with respect to liquefaction-induced lateral ground strain and angular distortion, respectively, that are derived from LiDAR surveys.

## **1.4 Scope and Organization**

This thesis consists of six chapters, the first of which provides introductory and background information, explains the thesis objectives, and describes the scope and organization of the work. Chapters 2 to 5 are organized in the format of four individual research papers. Chapter 2 deals with seismic wave interactions with underground pipelines before and after rehabilitation with in situ linings. It provides

an evaluation of how in situ lining technology improves the seismic performance of pipelines. Chapter 3 involves the evaluation of the water distribution system response during the 22 February 2011 earthquake in Christchurch, NZ, through spatial analysis with geocoded data and LiDAR survey data, and repair regressions for different types of pipeline with comprehensive screening criteria. Chapter 4 describes a probabilistic approach for evaluating the expected value of axial pipeline strain and provides correlations of pipeline damage with liquefaction-induced ground deformation, expressed in terms of the expected value of pipeline strain. Chapter 5 presents a statistical assessment of ground deformations measured by successive LiDAR surveys in Christchurch. This chapter explores how metrics of ground deformation can be spatially correlated with landforms and water ways in Christchurch, and investigates the relationship between lateral ground strain and differential vertical ground movement with the damage documented in residential buildings. Chapter 6 presents the conclusions of this work, and provides recommendations for future research.

## REFERENCES

- [1.1] O'Rourke TD. Lessons learned for lifeline engineering from major urban earthquakes. *Proceedings of the 11<sup>th</sup> World Conference on Earthquake Engineering*, 1996, Acapulco, Mexico.
- [1.2] O'Rourke TD. An overview of geotechnical and lifeline earthquake engineering. Geotechnical earthquake engineering and soil dynamics III, *Proceedings of the 1998 Specialty Conference on Geotechnical Earthquake Engineering and Soil Dynamics*, 1998, Seattle, Washington.
- [1.3] Bird J, O'Rourke TD, Bracegirdle A, Bommer J, Tromans I. A framework for assessing earthquake hazards for major pipelines. *Proceedings of the International Conference on Terrain and Geohazards Facing Onshore Oil and Gas Pipelines*, 2004, London, UK.
- [1.4] O'Rourke MJ, Liu JX. *Seismic design of buried and offshore pipelines*. Monograph No. 4: Multidisciplinary Center for Earthquake Engineering Research, Buffalo, NY, 2012.
- [1.5] Elhmadi K, O'Rourke MJ. Seismic damage to segmented buried pipelines. *Earthquake Engineering & Structural Dynamics* 1990; **19**(4): 529–539.
- [1.6] O'Rourke TD, Jeon S-S. Seismic zonation for lifelines and utilities. *Proceedings of the 6th International Conference on Seismic Zonation*, 2000, Palm Springs, CA.
- [1.7] Hamada M, O'Rourke TD., Eds. Case studies of liquefaction and lifeline performance during past earthquakes. *Japanese Case Studies Technical Rep. NCEER-92-0001*, Vol.1: National Center for Earthquake Engineering Research, Buffalo, NY, 1992.
- [1.8] Bray JD, O'Rourke TD, Cubrinovski M, Zupan JD, Jeon S-S, Taylor M, Toprak S, Hughes M, van Ballegooy S, Bouziou D. Liquefaction impact on critical infrastructure in Christchurch. *Final Technical Report*, U.S.G.S. award

number G12AP20034, 2013, available at <http://earthquake.usgs.gov/research/external/reports/G12AP20034.pdf>.

- [1.9] O'Rourke TD, Jeon S-S, Toprak S, Cubrinovski M, Hughes M, van Ballegooy M, Bouziou D. Earthquake response of underground pipeline networks in Christchurch, NZ. *Earthquake Spectra* 2014; **30**(1): 183-204.
- [1.10] Hamada M, Isoyama R, Wakamatsu K. Liquefaction induced ground displacement and its related damage to lifeline facilities. *Soils Foundations* 1996; **36**(1): pp. 81-97.
- [1.11] Eidinger J, Castro L, Ma D. The 1906 Earthquake impacts on the San Francisco and Santa Clara water systems-what we learned, and what we are doing about it. *Earthquake Spectra* 2006; **22**(2): S113-S134.
- [1.12] Scawthorn C, O'Rourke TD, Blackburn FT. The 1906 San Francisco earthquake and fire-enduring lessons for fire protection and water supply. *Earthquake Spectra* 2006; **22**(S2): S135-S158.
- [1.13] Pease JW, O'Rourke TD. Seismic response of liquefaction sites. *J. Geotechn. Geoenviron. Eng.* 1997; **123**(1): 37-45.
- [1.14] O'Rourke TD. Geohazards and large, geographically distributed systems. *Geotechnique* 2010; **60**(7): 505.
- [1.15] Kramer SR, McDonald WJ, Thomson JC. *An introduction to trenchless technology*. Van Nostrand Reinhold, New York, NY, 1992.
- [1.16] American Water Works Association (AWWA). *Rehabilitation of water mains*. Manual of Water Supply Practices M28, Denver, CO, 2001.
- [1.17] Sterling RL. No-dig techniques and challenges. *Journal of GeoEngineering* 2010; **5**(3): 63-67.

- [1.18] Barsoom J. Trenchless pipeline technology. *ASTM Standardization News* 1995, **23**:18-18.
- [1.19] Abraham DM, Gillani SA. Innovations in materials for sewer rehabilitation. *Tunneling and Underground Space Technology* 1999; **14**(S1): 43-56.
- [1.20] Matthews J, Condit W, Wensink R, Lewis G. Performance evaluation of innovative water main rehabilitation cured-in-place pipe lining product in Cleveland, OH. *EPA/600/R-12/012 Report*: USEPA, Edison, NJ, 2012.
- [1.21] Lund LV. Pipeline seismic mitigation using trenchless technology. *Proceedings of the 8<sup>th</sup> US-Japan workshop on earthquake resistant design lifeline facilities and countermeasures against liquefaction*, 2003, Tokyo, Japan.
- [1.22] Bouziou D, Wham BP, O'Rourke TD, Stewart HE, Palmer MC, Zhong Z, Filiatrault A, Aref A. Earthquake response and rehabilitation of critical lifelines. *Proceedings of the 15th World Conference on Earthquake Engineering*, 2012, Lisbon, Portugal.
- [1.23] Oskin ME, Arrowsmith JR, Corona AH, Elliott AJ, Fletcher JM, Fielding EJ, Gold PO, Gonzales-Garcia JJ, Hudnut KW, Liu-Zeng J, Teran OJ. Near-field deformation from the El Mayor–Cucapah earthquake revealed by differential LIDAR. *Science* 2012; **335**(6069): 702-705.
- [1.24] Olsen MJ, Cheung KF, Yamazaki Y, Butcher SM, Garlock M, Yim S, Piakowsky S, Robertson I, Burgos L, Young YL. Damage assessment of the 2010 Chile earthquake and tsunami using ground-based LiDAR. *Earthquake Spectra* 2012; **28**(S1): 179-197.
- [1.25] Kayen R, Pack RT, Bay J, Sugimoto S, Tanaka H. Terrestrial-LIDAR visualization of surface and structural deformations of the 2004 Niigata Ken Chuetsu, Japan, earthquake. *Earthquake Spectra* 2006; **22**(S1):147-162.
- [1.26] Chen RF, Chang KJ, Angelier J, Chan YC, Deffontaines B, Lee CT, Lin ML. Topographical changes revealed by high-resolution airborne LiDAR data: The

1999 Tsaoling landslide induced by the Chi–Chi earthquake. *Engineering Geology* 2006; **88**(3): 160-172.

## CHAPTER 2

### SEISMIC BODY WAVE INTERACTIONS WITH BURIED PIPELINES BEFORE AND AFTER REHABILITATION WITH IN SITU LININGS

#### **Abstract**

This chapter deals with the seismic response of underground pipelines that are rehabilitated with in situ fiber reinforced polymer (FRP) linings, and the analysis and design of full-scale testing to quantify the response of FRP-reinforced pipelines to seismic wave interaction. Soil-pipeline interaction in the pipeline axial, transverse lateral and transverse vertical directions is considered using elasto-plastic models in finite element simulations to determine the most prominent form of pipeline deformation caused by seismic body waves. Sensitivity analysis is performed to investigate the effect of soil stiffness and pipe diameter on pipeline deformation. Results indicate that axial pipeline deformation under seismic waves is from two to four orders of magnitude greater than deformations induced in other directions, and that induced pipeline rotations are negligible. The axial response of pipelines rehabilitated with cured in place pipe lining technology to transient ground deformation is studied both numerically and experimentally. Pipeline performance before and after rehabilitation is compared, and the effectiveness of in situ lining technology for seismic retrofit is evaluated. The full-scale test results show that in situ FRP polymer linings reduce axial deformation under seismic waves by 40% to 85%.

Therefore, the use of in situ linings for pipeline rehabilitation provides substantial seismic strengthening against transient ground deformations.

## **2.1 Introduction**

Significant damage in buried pipelines caused by transient ground deformation (TGD) has been observed during past earthquakes, such as the 1985 Michoacan [2.1] [2.2], and the 1994 Northridge earthquakes [2.3]. Analytical studies by Elhmadi and O'Rourke [2.4] and O'Rourke et al. [2.5] show that joint displacements due to seismic wave propagation are related to variations in joint pullout resistance and stiffness, and the largest joint deformations are concentrated at the weakest joints. Moreover, experience with segmented pipelines during past earthquakes shows that seismic failure is most often concentrated at the joints [2.6] [2.7] [2.8]. Pipelines affected by aging and loss of structural integrity are vulnerable to TGD due to high concentrations of movement at weak joints or locations of cracks and breaks [2.9]. Similarly, segmented pipelines are susceptible to TGD-induced damage in areas where axial pipeline forces, caused by tensile ground strains, exceed the pull-out capacity of locally weak joints.

Figure 2.1 shows the modes of deformation of a pipeline with a weak joint or circumferential crack. Assuming that deformation due to TGD is concentrated at a locally weak joint or circumferential crack, there are six possible deformations that can occur: axial, vertical and transverse horizontal displacement, vertical and

horizontal rotation, as well as torsion. No evidence exists for torsion in pipelines due to TGD during past earthquakes, and, thus, further attention is not given to this case. Previous research suggests that pipelines are primarily affected by TGD in the axial direction, whereas angular rotations associated with bending strains generated by TGD are generally small [2.6] [2.8]. A systematic, detailed assessment of the different modes of segmented pipeline response to seismic waves is not available in the technical literature. Such a study is important to establish the most prominent pipeline deformation modes, and thereby develop analytical models and testing protocols to evaluate seismic retrofit options.

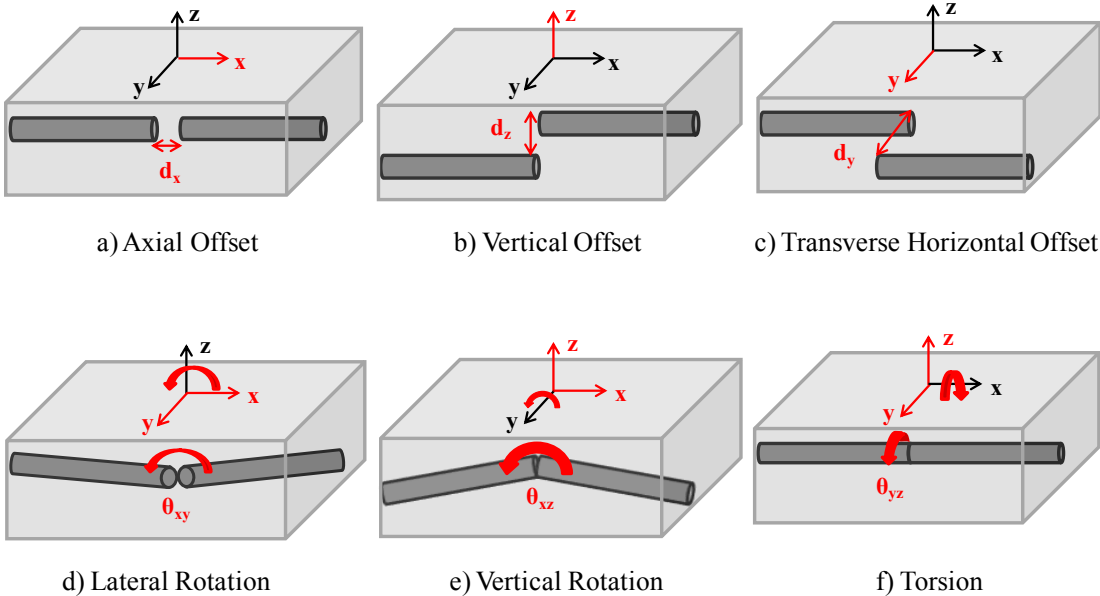


Figure 2.1. Deformations at a weak joint or circumferential crack due to seismic wave interactions with segmented pipelines or pipelines with circumferential cracks.

In situ pipe lining technologies have been used extensively for rehabilitation of existing lifelines without expensive excavation and disruptive methods of installation [2.10] [2.11] [2.12]. They involve the installation of polymeric linings remotely inside existing, underground pipelines. The linings allow continuity of pipeline flow, prevent leakage and intrusion, and provide variable degrees of structural reinforcement to support the operation of deteriorated pipelines. Despite these benefits, their application for seismic retrofit is not included in current design and construction practices due to lack of analytical and experimental studies that quantify their effectiveness.

The effects of TGD on aging pipelines, which have lost structural integrity, are explored through numerical simulation of the seismically induced deformation modes illustrated in Figure 2.1a through Figure 2.1e. The numerical simulation is predicated on a pipeline with a weak joint or circumferential crack that provides negligible resistance to deformation. As a worst case for pipeline continuity, this case provides an upper bound on local pipeline deformation.

The axial response of a pipeline rehabilitated with in situ linings is investigated both numerically and experimentally. The results of full-scale dynamic tests, conducted at the twin re-locatable shake table facility of the Structural Engineering and Earthquake Laboratory (SEESL) at the University at Buffalo (UB), are presented. Comparison of pipeline response before and after rehabilitation with in situ linings demonstrates and quantifies the effectiveness of in situ lining technology for seismic retrofit.

## 2.2 Body Wave Effects on Pipelines

Underground pipelines may be affected by body and surface waves. It is well known that near source motions are accompanied by large velocity pulses with the potential for high levels of pipeline axial strain and joint displacement [2.9]. Ground motion records from the 1999 Chi Chi earthquake [2.13], for example, show a strong velocity pulse of 306 cm/sec and a predominant period of nearly 10 sec. This velocity pulse with respect to pipeline damage is equivalent to surface wave effects observed and analyzed for pipeline performance during the 1985 Michoacan earthquake [2.14]. Given the high potential for pipeline damage and well-recognized importance of near source ground motions, body waves, in the form of S-waves with high velocity pulses, are taken as the prime source of seismic wave interaction in this study.

Body wave effects on underground pipelines are generated primarily by S-waves that intersect the pipeline at an angle of incidence,  $\gamma_i$ , illustrated in Figure 2.2 [2.15]. The ground strain due to TGD parallel to the pipeline axis,  $\varepsilon_g^x$ , is

$$\varepsilon_g^x = V_a^x / C_a^x \quad (2.1)$$

where  $V_a^x$  and  $C_a^x$  are the particle velocity and apparent wave propagation velocity, respectively, along the longitudinal pipeline axis, x:

$$C_a^x = \frac{C}{\sin \gamma_i} \quad (2.2)$$

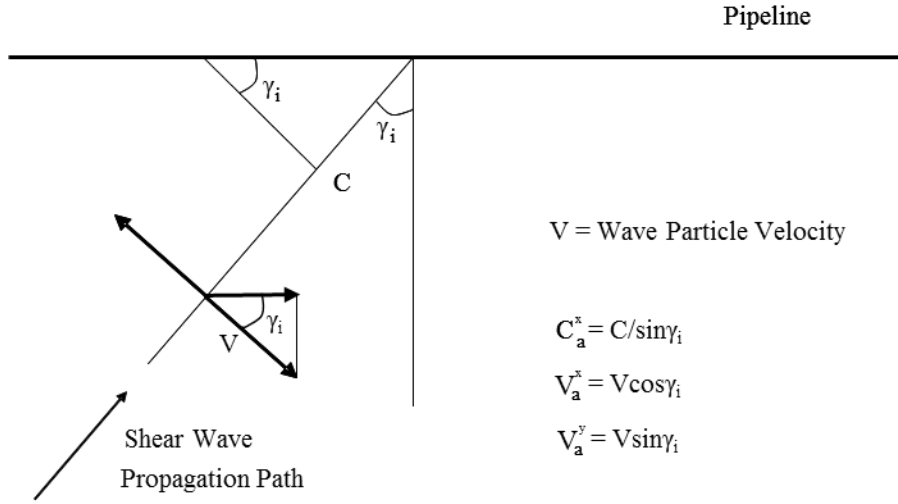


Figure 2.2. Pipeline subjected to S-wave propagation.

$$V_a^x = V \cos \gamma_i \quad (2.3)$$

Combining Equations 2.1 through 2.3 provides the maximum axial ground strain,  $\epsilon_g^x$ , parallel to the pipeline, which is

$$\epsilon_g^x = \frac{V \sin 2\gamma_i}{2C} \quad (2.4)$$

S-waves intersecting the pipeline at an angle of incidence,  $\gamma_i$ , also impose ground displacements perpendicular to the pipeline axis, resulting in deformations in the transverse lateral pipeline direction. The horizontal ground shear strain,  $\gamma_g^y$ , generated by S-wave propagation along the pipeline is

$$\gamma_g^y = \tan^{-1} \frac{V_a^y}{C_a^x} \quad (2.5)$$

where  $C_a^x$  is given by Equation 2.2, and  $V_a^y$  is the horizontal particle velocity perpendicular to the pipeline:

$$V_a^y = V \sin \gamma_i \quad (2.6)$$

Combining Equations 2.2, 2.5 and 2.6 provides the maximum horizontal ground shear strain,  $\gamma_g^y$ , perpendicular to the pipeline, which is

$$\gamma_g^y = \tan^{-1} \frac{V \sin^2 \gamma_i}{C} \quad (2.7)$$

The vertical component of S-waves generates ground shear strains in the vertical direction that affect pipelines. Similar to horizontal ground shear strains, the vertical ground shear strain along the pipeline is

$$\gamma_g^z = \tan^{-1} \frac{V^z}{C_a^x} \quad (2.8)$$

where  $C_a^x$  is given by Equation 2.2, and  $V_z$  is the vertical particle velocity.

Combining Equations 2.2 and 2.8 provides the maximum vertical ground shear strain,  $\gamma_g^z$ , perpendicular to the pipeline, which is

$$\gamma_g^z = \tan^{-1} \frac{V^z \sin \gamma_i}{C} \quad (2.9)$$

S-waves also induce horizontal ground curvatures,  $K_g^{xy}$ , perpendicular to the pipeline [2.8]. If a segmental pipeline contains joints that rotate, ground curvature can result in relative rotation at the pipeline joints as the pipeline deforms segmentally in response to the seismically induced curvature. The horizontal ground curvature,  $K_g^{xy}$ , perpendicular to the pipeline is

$$K_g^{xy} = \frac{A_a^y}{C_a^x} \quad (2.10)$$

where  $C_a^x$  is given by Equation 2.2, and  $A_a^y$  is the apparent horizontal ground acceleration perpendicular to the pipeline axis, x:

$$A_a^y = A \sin \gamma_i \quad (2.11)$$

Combining Equations 2.2, 2.10 and 2.11 provides the maximum ground horizontal curvature,  $K_g^{xy}$ , perpendicular to the pipeline, which is

$$K_g^{xy} = \frac{A \sin^2 \gamma_i}{C} \quad (2.12)$$

Similar to the case of horizontal ground rotation, S-wave propagation also generates vertical ground curvatures,  $K_g^{xz}$ , perpendicular to the pipeline that result in relative vertical rotation at the pipeline joints as the pipeline deforms segmentally in response to the seismically induced curvature. The vertical ground curvature,  $K_g^{xz}$ , perpendicular to the pipeline axis is

$$K_g^{xz} = \frac{A^z}{C_a^x} \quad (2.13)$$

where  $C_a^x$  is given by Equation 2.2, and is the vertical ground acceleration.

Combining Equations 2.2 and 2.13 provides the maximum vertical ground curvature,  $K_g^{xz}$ , which is

$$K_g^{xz} = \frac{A^z \sin \gamma_i}{C} \quad (2.14)$$

### 2.3 Modeling Methodology

A finite element (FE) model for seismic wave interactions with pipelines was developed using the numerical code ABAQUS 6.9-2. The modeling approach was based on the model developed by O'Rourke et al. [2.5] for the axial displacement of a locally weak joint in response to seismic wave interaction. The FE model is illustrated in Figure 2.3a. The length of the pipe elements for flexural deformation and joint rotation was equal to 0.18 m, which is much lower than the criterion for maximum element length by Borelli et al. [2.16]. The pipeline element length for axial displacement analyses was determined by mesh convergence studies to be 3.5 m, which is on the order of approximately 1/1000<sup>th</sup> of the wavelength of the body waves used in this study.

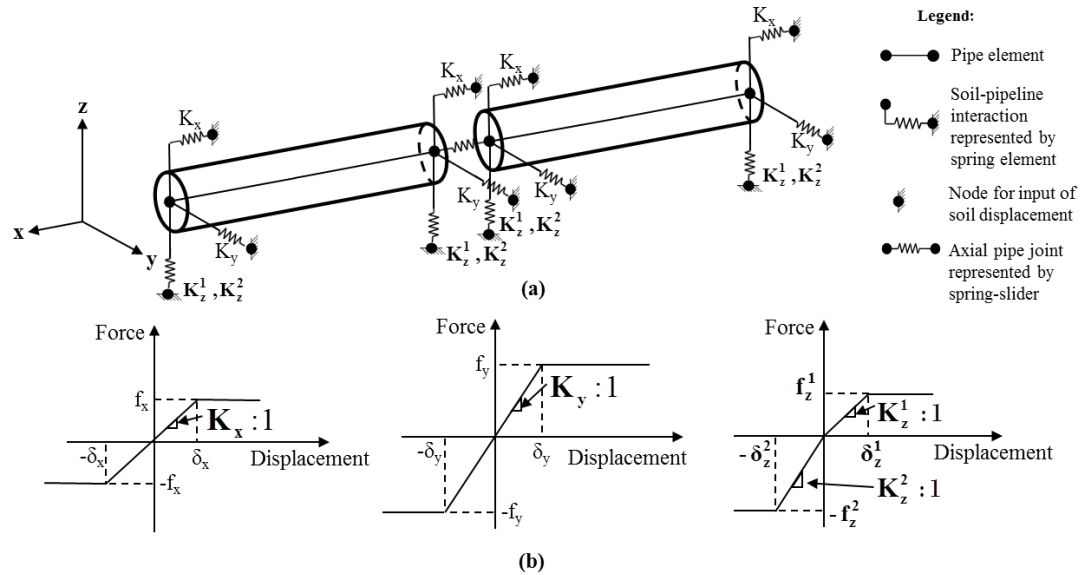


Figure 2.3. a) Schematic of FE model, and, b) bilinear force vs displacement relationships at pipe-soil interface based on the elasto-plastic models by ASCE [2.17].

Soil-pipeline interactions were considered using elasto-plastic models proposed by ASCE [2.17] to characterize spring elements spaced at distances equal to element length used for each case. Schematics of the bilinear force vs. displacement relationships in the pipeline axial, transverse lateral and vertical directions are presented in Figure 2.3b. The pipeline was assumed to have a circumferential crack, represented by an axial spring with negligible tensile stiffness, whereas the compressive stiffness was set equal to the pipeline axial stiffness,  $E_p A_p$ , where  $E_p$  is the pipe Young's modulus and  $A_p$  is the cross sectional pipe area. The shear stiffness of the crack in the transverse lateral and vertical direction, and the bending stiffness of the circumferential crack were assumed to be negligible.

The ground motion record at the Rinaldi receiving station during the 1994 Northridge earthquake was used as input motion to study S-wave interactions with

pipelines. The record was obtained from the NGA Database in the PEER library of ground motions [2.18]. Figure 2.4 shows the time history of horizontal ground velocity at the Rinaldi receiving station at N228E azimuth which contains a horizontal peak ground velocity, PGV=148 cm/sec. This PGV is the largest horizontal PGV recorded in the U.S.

The ground motion time records were converted to displacement versus distance records for S-wave interactions with pipelines. It was assumed that  $X = C_a^x t_m$ , in which  $X$  is distance,  $t_m$  is time from the strong motion recording, and  $C_a^x$  is calculated from Equation 2.2, using  $C \approx 2.5$  km/sec, which is the wave propagation velocity frequently used for crustal conditions in California.

## **2.4 Numerical Analysis of Pipeline Response Before Rehabilitation**

### **2.4.1 Axial Pipeline Deformation**

Pipelines representing approximately 66% of the U.S. water distribution system are composed of nominal 150- and 200-mm-diameter pipelines [2.19]. Because of their prominence in water delivery systems, nominal 150-mm-diameter pipelines were selected for large scale testing and attendant numerical simulations. A nominal 150-mm-diameter ductile iron (DI) pipeline with 175-mm outer diameter,  $D$ , and 6.35-mm wall thickness,  $t$ , was used as the baseline case for FE analysis and experimental design. The pipe axial stiffness was  $E_p A_p = 556,740$  kN. The pipeline was assumed to

be buried at  $z_p = 1.22$  m depth to the top of pipe in partially saturated sand with an effective friction angle  $\phi' = 38^\circ$  and unit weight  $\gamma = 19.64$  kN/m<sup>3</sup>. However, for the FE sensitivity analyses, the pipeline burial conditions were varied to represent a wide range of conditions bounded by 0.6 and 1.2 m in  $z_p$  and  $33^\circ$  to  $45^\circ$  in  $\phi'$  pertaining to the lowest and highest cases of soil resistance, respectively.

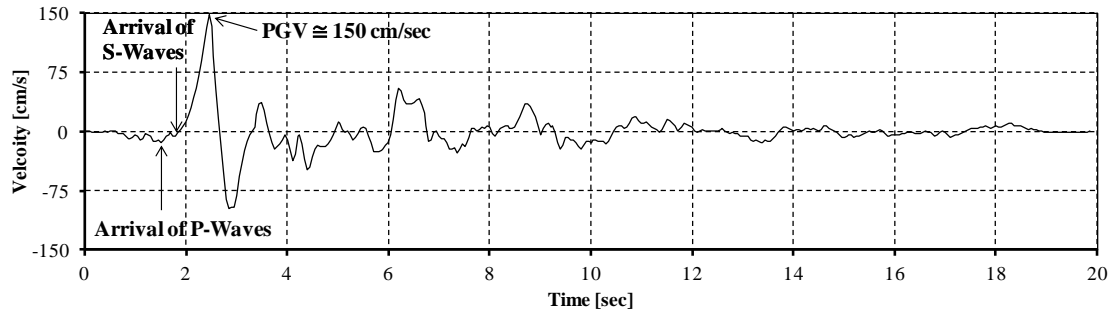


Figure 2.4. Horizontal ground velocity time history at N228E azimuth recorded at Rinaldi station during the 1994 Northridge earthquake [2.18].

The pipeline in the baseline case was subjected to the original Rinaldi ground motion recorded at N228E azimuth during the 1994 Northridge earthquake, as shown in Figure 2.4. The maximum recorded velocity, corresponding to fault normal motions was assumed to intersect the pipeline at  $\gamma_i = 45^\circ$  with  $C = 2.5$  km/sec to produce the maximum  $\epsilon_g^x$  presented in Equation 2.4.

Figure 2.5a shows the maximum relative axial displacement of the circumferential crack, which is distributed in a slightly asymmetric manner on either side of the cracked joint to reflect the shape of the ground strain pulse. The maximum axial offset,  $d_x$ , is 9.64 mm at the location of the circumferential crack. Figure 2.5b shows

the numerical results for pipe and ground axial strains,  $\epsilon_p^x$  and  $\epsilon_g^x$ , respectively, surrounding the circumferential crack. The pipeline response shown in Figure 2.5 is consistent with the behavior presented by O'Rourke et al. [2.5] for a pipeline that is axially flexible with respect to ground strain accumulation. It is assumed that the pipeline is continuous on either side of the circumferential crack.

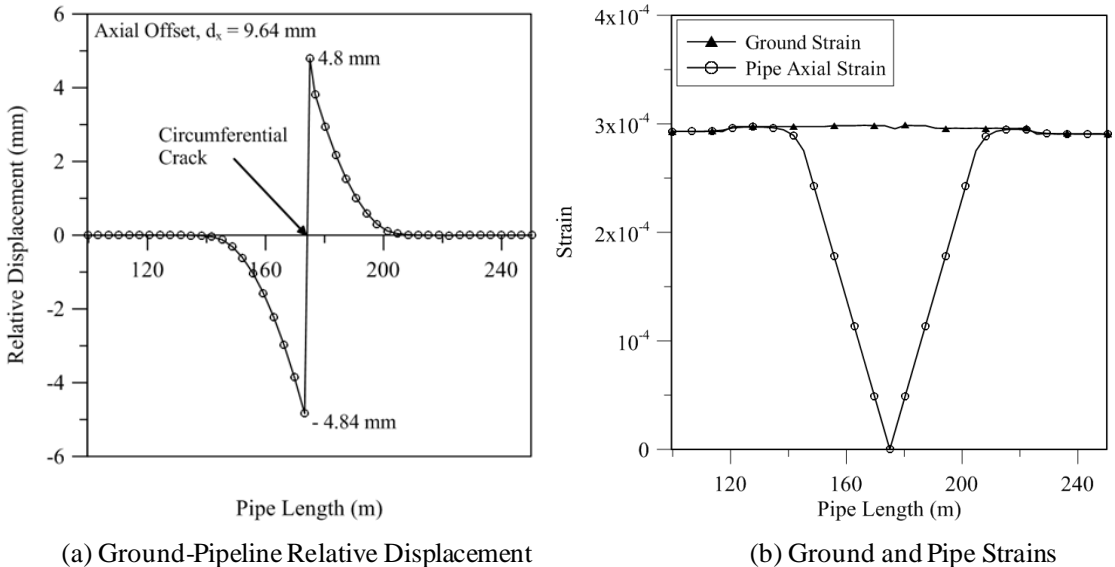


Figure 2.5. FE results for pipeline with circumferential crack subjected to the Rinaldi record during the 1994 Northridge earthquake.

Using the same analytical model, a sensitivity analysis was performed to investigate the effect of pipeline diameter,  $D$ , and axial shear resistance between pipe and soil,  $f$ , on the maximum axial offset,  $d_x$ . Pipelines that are commercially available with outer diameters and wall thicknesses, respectively, of 17.5 and 0.64; 33.5 and 0.71; 65.5 and 1.09; 97.3 and 1.42 cm, buried in variable ground conditions, were subjected to the Rinaldi ground motion. Figure 2.6 shows the maximum induced  $d_x$

with respect to  $D$  and the dimensionless expression for  $f$ . Power function fitting curves based on the analytical results for each case of  $D$  and  $t$  are also presented in Figure 2.6. The baseline case of a 17.5-cm diameter pipeline buried in partially saturated medium dense sand shown in Figure 2.5 is also highlighted in Figure 2.6. The axial offset  $d_x$  caused by the Rinaldi ground motion, shown in Figure 2.6, increases with  $D$ , and decreases for higher axial soil frictional resistance. The decay rate of  $d_x$  with respect to  $f$  follows an exponential function for all pipeline diameters. Values of  $d_x$  range from 0.8% of  $D$ , for the case of  $D = 97.3$  cm with dimensionless  $f$  equal to 7.4, to 16% of  $D$ , for the case of  $D = 17.5$  cm with dimensionless  $f$  equal to 0.8.

#### **2.4.2 Transverse Lateral and Vertical Pipeline Deformation**

The transverse lateral and vertical response of a pipeline with a circumferential crack subjected to S-wave propagation was also studied through numerical analysis. Pipelines with diameters ranging from 17.5 to 97.3 cm, and buried in variable ground conditions, were subjected to the Rinaldi ground motion to determine the maximum induced lateral and vertical offsets.

During FE simulations, it was assumed that the maximum lateral offset,  $d_y$ , of the circumferential crack coincides with the location and direction of maximum horizontal ground shear strain in Equation 2.7. Based on Equation 2.7, the maximum  $d_y$  occurs when the maximum recorded horizontal velocity in the Rinaldi record intersects the pipeline at  $\gamma_i = 90^\circ$  with  $C = 2.5$  km/sec and therefore causes the maximum  $\gamma_g^y$ .

Similarly, the maximum vertical offset caused by S-waves,  $d_z$ , coincides with the location and direction of the maximum  $\gamma_g^z$  in Equation 2.9. In this case, the maximum  $d_z$  occurs when the maximum recorded vertical velocity in the Rinaldi record intersects the pipeline at  $\gamma_i = 90^\circ$  with  $C = 2.5$  km/sec and causes the maximum  $\gamma_g^z$  in Equation 2.9.

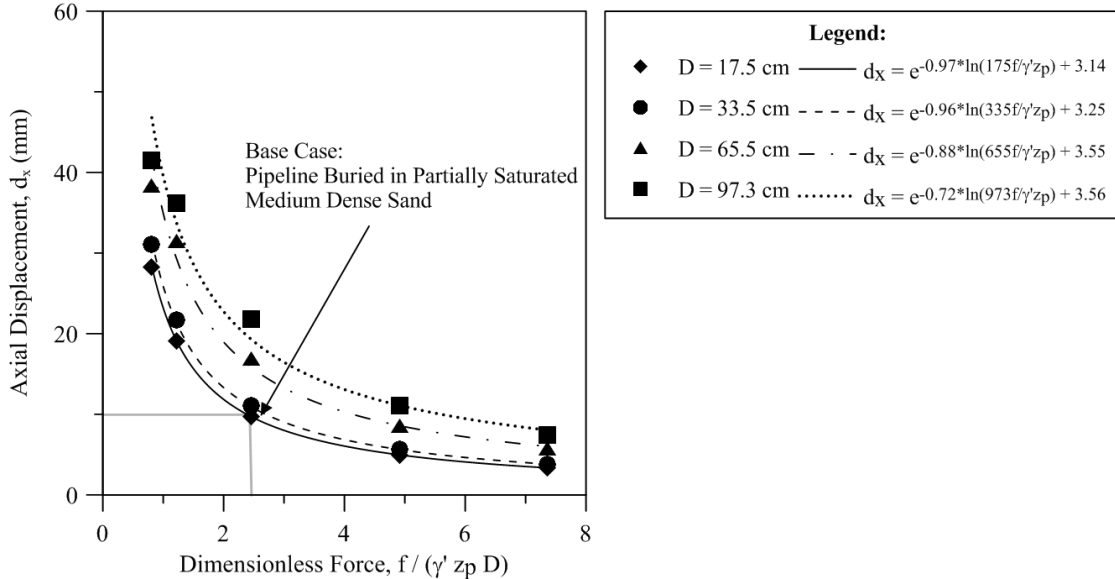


Figure 2.6. Sensitivity analysis of axial pipeline offset at circumferential crack subjected to the Rinaldi record during the 1994 Northridge earthquake.

Figures 2.7a and 2.7b show the maximum  $d_y$  and  $d_z$ , respectively, caused by the Rinaldi ground motion with respect to  $D$  and maximum dimensionless soil lateral force,  $N_{qh}$ , by Jung et al. [2.20], and maximum dimensionless soil upward movement force,  $N_{qv}$ , by Jung et al. [2.21]. The soil upward resistance  $N_{qv}$  was selected as a variable that reflects soil resistance because the maximum recorded velocity in the Rinaldi record is associated with upward ground movements in the vicinity of the

circumferential crack, and therefore, induces upward pipeline movements at this location.

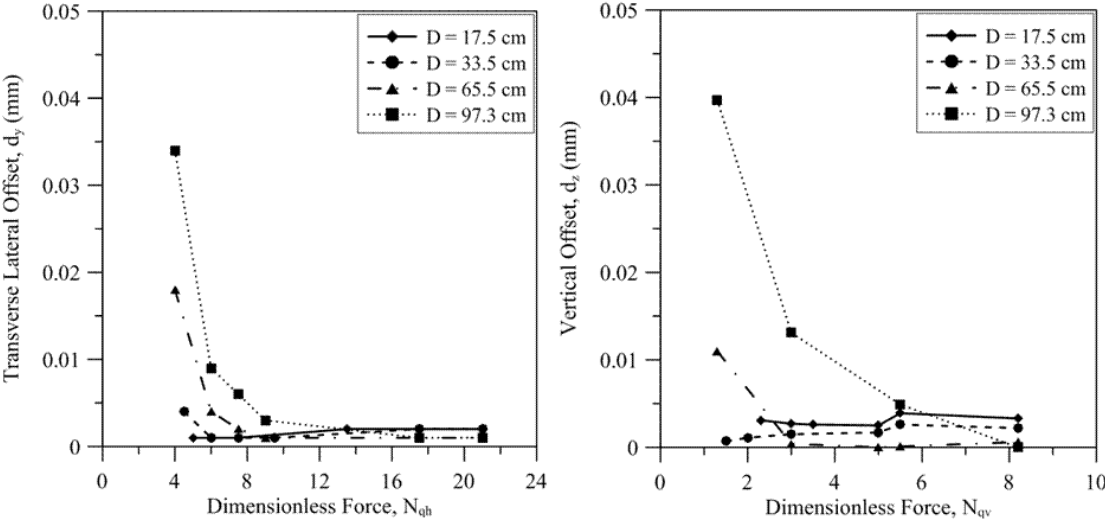


Figure 2.7. Sensitivity analysis of a) transverse lateral, and b) transverse vertical pipeline offset at circumferential crack caused by the Rinaldi record during the 1994 Northridge earthquake.

The lateral offset,  $d_y$ , caused by the Rinaldi ground motion in Figure 2.7a increases with  $D$  for  $N_{qh} \leq 9$ , and is very small for stiffer ground conditions for any  $D$ . As shown in Figure 2.7b,  $d_z$  caused by the Rinaldi ground motion is sensitive to  $N_{qv}$  for  $D = 97.3$  cm, whereas it remains generally insensitive to  $N_{qv}$  for smaller diameters. Pipelines with greater diameter have greater bending stiffness, and, thus, are more rigid relative to the ground. As a result, pipelines with greater diameters are generally associated with larger values of  $d_y$  and  $d_z$  in Figures 2.7a and 2.7b, respectively. Analytical results of pipeline response to S-waves in the transverse lateral and vertical direction

indicate negligible offset values at the circumferential crack, and underscore the relative importance of pipeline deformation due to TGD in the axial direction.

### **2.4.3 Transverse Lateral and Vertical Pipeline Rotation**

The maximum rotation of a pipeline with a circumferential crack in the horizontal and vertical planes caused by S-waves was studied through the FE model previously discussed. According to Equation 2.12, the maximum lateral rotation at the circumferential crack,  $\theta_{xy}$ , induced by S-wave propagation, occurs when the ground surrounding the circumferential crack is subjected to the maximum recorded horizontal acceleration associated with S-wave propagation. Hence, it was assumed that the Rinaldi ground motion intersects the pipeline at  $\gamma_i = 90^\circ$  with  $C = 2.5$  km/sec to produce the maximum  $K_g^{xy}$  presented in Equation 2.12, and, hence, maximum  $\theta_{xy}$ . Similarly, the maximum vertical rotation at the circumferential crack,  $\theta_{xz}$ , due to S-wave propagation occurs when the ground surrounding the circumferential crack is intersected by the maximum recorded vertical acceleration associated with S-wave propagation at  $\gamma_i = 90^\circ$  with  $C = 2.5$  km/sec to produce maximum  $K_g^{xz}$  presented in Equation 2.14.

The FE results of  $\theta_{xy}$  and  $\theta_{xz}$  for pipelines with outer diameters 17.5, 33.5, 65.5, and 97.3 cm, buried in variable ground conditions, and subjected to the Rinaldi ground motion during the 1994 Northridge earthquake are presented in Figure 2.8a and Figure 2.8b, respectively. Figure 2.8a shows the results of sensitivity analysis of maximum

$\theta_{xy}$  caused by S-waves to D and  $N_{qh}$  [2.20]. The maximum induced lateral rotation is insensitive to both D and  $N_{qh}$  and significantly small ( $\theta_{xy} \approx 0.002^\circ$ ). The results of sensitivity analysis on the maximum  $\theta_{xz}$  caused by S-waves to D and  $N_{qv}$  [2.21] are shown in Figure 2.8b and indicate that the maximum induced  $\theta_{xy}$  is insensitive to both D and  $N_{qv}$  and negligible ( $\theta_{xz} \approx 0.02^\circ$ ).

The numerical results presented in Figure 2.5 through Figure 2.8 indicate that the most important form of deformation in pipelines with weak joints and circumferential cracks subject to S-wave propagation occurs in the axial pipeline direction. S-wave effects in terms of transverse lateral and vertical offset and rotation are negligible. The dominant axial deformation occurs as a separation at the circumferential crack.

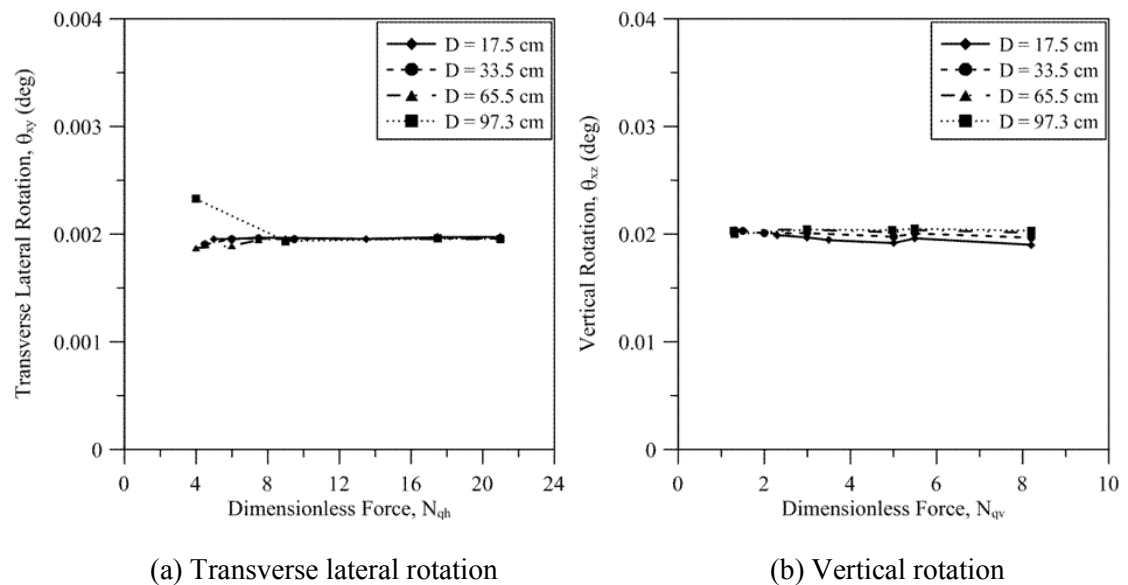


Figure 2.8. Sensitivity analysis of a) transverse lateral, and b) transverse vertical pipeline rotation at circumferential crack caused by the Rinaldi record during the 1994 Northridge earthquake.

#### **2.4.4 S-Wave Effects on Pipelines for the Highest Recorded Levels of PGV and PGA**

The results presented in Figure 2.5 through Figure 2.8 provide a comparative study among the different modes of deformation, but they do not reflect the maximum possible levels of pipeline deformation. The highest recorded vertical and horizontal peak ground accelerations (PGAs) and peak ground velocities (PGVs) are reported by Anderson [2.13], and the Rinaldi record was scaled according to these values to approximate the highest levels of  $d_x$ ,  $d_y$ ,  $d_z$ ,  $\theta_{xy}$  and  $\theta_{xz}$  due to body wave effects. The baseline case of a pipeline with a circumferential crack that was previously discussed was used in the FE analyses. Table 2.1 provides information about the recording station, earthquake, and amplitude of highest vertical and horizontal components of PGA and PGV on record. The ratio of the highest recorded PGA or PGV to the PGA or PGV of the Rinaldi record in each respective direction is also presented as the scale ratio in Table 2.1.

The Rinaldi record was scaled upwards 2.1 times to reflect the maximum recorded horizontal PGV at the TCU068 receiving station during the 1999 Chi-Chi earthquake. The Rinaldi record was also scaled upwards 4.6 times to reach the amplitude of vertical PGV during the same earthquake. The same record was scaled up 2.3 times for the case of  $\theta_{xy}$  to represent the horizontal PGA recorded at the MYGO12 station during the 2011 Tohoku earthquake, and 4.1 times for the case of  $\theta_{xz}$  to represent the vertical PGA recorded at the ITWH25 Ichinoseki\_W station during the 2008 Southern

Iwake earthquake. Although such scaling does not account for the period, or frequency, of the maximum pulse, it does allow for pipeline deformation to be compared under wave interaction approximating upper bound conditions.

Table 2.1. Highest recorded components of PGA and PGV and their relationship to the Rinaldi record during the 1994 Northridge earthquake.

Parameter:	PGA (g)		PGV (cm/sec)	
Component:	Vertical	Horizontal	Vertical	Horizontal
Station Name:	ITWH25 Ichinoseki_W	MYG012	TCU068	TCU068
Earthquake Name:	2008 Southern Iwake (Iwake)	2011 Tohoku	1999 Chi-Chi	1999 Chi-Chi
Parameter Amplitude:	3.92	2.02	195.5	306
Scale Ratio:	4.1	2.3	4.6	2.1

The maximum values of  $d_x$ ,  $d_y$ ,  $d_z$ ,  $\theta_{xy}$  and  $\theta_{xz}$  from FE analyses using the scaled Rinaldi record and baseline case are summarized in Table 2.2. Also shown in the table are the deformations prior to scaling. The maximum  $d_x$ ,  $d_y$ ,  $d_z$ ,  $\theta_{xy}$  and  $\theta_{xz}$  deformations after scaling provide upper bounds and approximations of pipeline deformation. The maximum  $d_x$  is approximately three to two orders of magnitude larger than the maximum  $d_y$  before and after scaling, respectively, and nearly three orders of magnitude larger than  $d_z$  both before and after scaling. Such differences indicate that axial movement has by far the greatest potential to affect pipeline performance when compared with other non-axial deformations induced by seismic waves.

The analytical results show that the  $d_y$ ,  $d_z$ ,  $\theta_{xy}$  and  $\theta_{xz}$  deformations are very small, with negligible effect on seismic performance for pipelines before and after

rehabilitation. The problem of seismic wave interaction with segmented pipelines can therefore be simplified in terms of  $d_x$  response. These sensitivity studies facilitate future analyses and design by showing that an effective seismic wave interaction model needs to focus on axial deformation at the joints or discontinuities in the pipeline. The sensitivity studies also facilitate the experimental design for large-scale testing to focus exclusively in the axial pipeline direction. It should be recognized that the sensitivity studies assume homogeneous soil conditions and that the presence of abrupt changes in soil properties in the vicinity of locally weak joints or cracks may increase the non-axial components of deformation. Given the very low levels of non-axial deformation for homogeneous soil conditions, a substantial contrast in subsurface properties is required to generate significant non-axial deformation effects.

Table 2.2. FE Results using the Rinaldi record during the 1994 Northridge earthquake scaled according to the highest recorded components of PGA and PGV during past earthquakes.

	Deformation before scaling	Deformation after scaling	Rinaldi Record Scale Ratio
$d_x$ (mm)	9.64	41.97	2.10
$d_y$ (mm)	0.002	0.093	2.10
$d_z$ (mm)	0.003	0.014	4.60
$\theta_{xy}$ (deg)	0.002	0.0045	2.30
$\theta_{xz}$ (deg)	0.02	0.0816	4.10

## 2.5 Numerical Analysis of Pipeline Response After Rehabilitation

Similar to pipeline response with a circumferential crack before rehabilitation, the effects of seismic wave propagation on pipelines rehabilitated with in situ linings were investigated through numerical and experimental studies. The baseline case of a nominal 150-mm pipeline, consisting of a 175-mm outer diameter and 6.35-mm wall thickness DI pipe, was also used to investigate lined pipeline seismic response.

Two different linings were used in this study to evaluate the effectiveness of in situ lining technology for improved pipeline seismic performance: 1) IMain® liner manufactured by Insituform Technologies, LLC, Chesterfield, MO, and 2) Starline2000® liner manufactured by Progressive Pipeline Management, LLC, West Deptford, NJ. The lining installation involves the insertion of a tube saturated with a thermosetting resin, which cures inside the existing pipeline. The IMain® installation results in a relatively stiff, structural tube, and is referred to as a cast-in-place pipe (CIPP). The Starline2000® installation results in a more flexible tube, and is referred to as a CIPP lining.

As shown in Figure 2.9a, the IMain® liner is composed of unwoven polyester felt impregnated with epoxy resin and reinforced with a central 3-layer system of glass fibers oriented at +/- 45° and 90° with respect to the pipeline axis. The IMain® liner has 150 mm outer diameter and 7.11 mm wall thickness, with axial deformation stiffness  $E_{IMain}A_{IMain} = 15,840$  kN, when cured. As shown in Figure 2.9b,

Starline2000® liner consists of woven polyester yarns coated with thermoplastic polyurethane elastomer. The cured Starline2000® woven hose liner has 150 mm outer diameter and 1.47 mm wall thickness, with  $E_{\text{Starline}}A_{\text{Starline}} = 2,042 \text{ kN}$ , and is significantly thinner and more flexible than IMain® liner. Both linings are bonded to the interior pipe surface by epoxy that cures in place during and after installation.

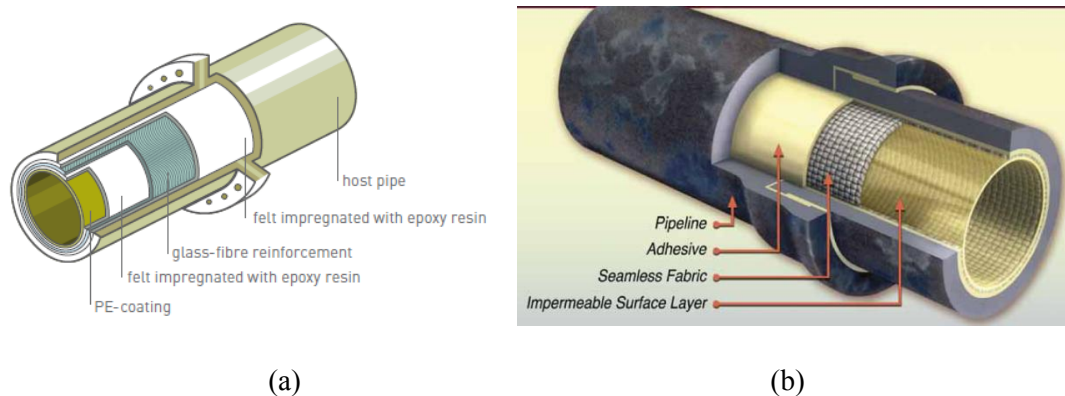


Figure 2.9. a) 3-dimensional view of the three-layer In situ Main® lining system after the installation in the host pipe, and b) 3-dimensional view of the three-layer Starline2000® lining system after the installation in the host pipe.

The FE model illustrated in Figure 2.3 was used in the numerical analysis. The analytical model used in FE simulations was based on the model described by O'Rourke et al. [2.5] and Bouziou et al. [2.22] for the axial displacement of a locally weak joint on a pipeline that is relatively flexible with respect to the surrounding ground and subjected to seismic wave propagation. The performance of a weak joint is similar to that of a circumferential crack rehabilitated with an in situ lining. Figure 2.10 provides an illustration of the analytical model. The pipeline either side of the weak joint is assumed to have full capacity joints and behave as a continuous pipeline.

As shown in Figure 2.10, the pipeline is axially flexible with respect to ground strain accumulation due to wave propagation, and deforms as much as the surrounding ground resulting in  $\epsilon_p^x = \epsilon_g^x$  everywhere the pipeline is continuous. The maximum axial force,  $P_u^x$ , that the weak joint can sustain corresponds to the pullout strain,  $\epsilon_u^x = P_u^x / EA$ . When the axial force at the weak joint exceeds  $P_u^x$ , the joint yields. As the seismic wave passes across the weak joint, strain in the pipeline on each side of the weak joint will accumulate linearly from  $\epsilon_p^x = P_u^x / EA$  to  $\epsilon_p^x = \epsilon_g^x$  at a slope of  $f/EA$ . The shaded area in the figure is the integration of the differential strain between pipeline and ground, which equals  $d_x$ .

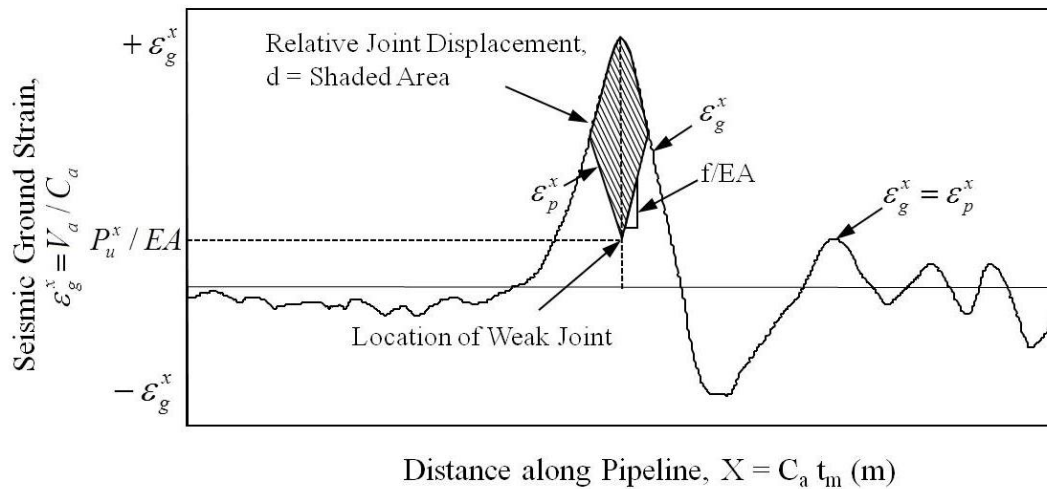


Figure 2.10. Relative joint displacement from seismic wave interaction with a pipeline rehabilitated with an in situ lining.

In all FE analyses it was assumed that the lining was installed in a DI pipeline with a weak joint or circumferential crack. The circumferential crack reinforced with the liner was represented by an axial spring in the FE model. Axial pull-out tests were

performed on lined DI pipe specimens to characterize the axial force vs displacement relationship for the lined joints used in FE simulations.

The axial pull-out tests were performed on several specimens of 150 mm nominal diameter (175 mm outer diameter) DI pipe joints with lengths ranging between 2.14 m and 2.65 m. Figure 2.11a is a cross-section of a standard push-on joint of a nominal 150-mm-diameter ductile iron (DI) pipeline. The DI joint lacks both pullout and moment capacity with a small separation between bell and spigot (1~4 mm) and, thus, it was used in the experimental work as a mechanical equivalent of a weak joint or circumferential crack, typically found in aging cast iron (CI) pipelines. The test setup for an axial pull test is presented in Figure 2.11b for which the lined pipe specimen has been fabricated with a 4-mm gap to simulate a circumferential crack. As shown in Figure 2.11b, axial pull forces were applied with a 25-tonne MTS actuator, while displacement across the circumferential gap was measured with DCDTs.

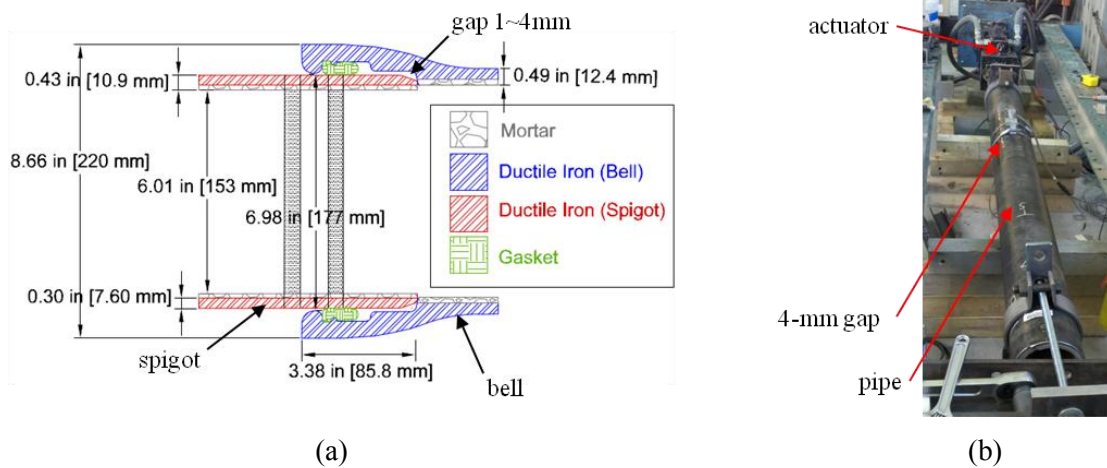


Figure 2.11. (a) Ductile iron joint cross-section. (b) Experimental setup for lined pipe pullout tests.

Results from axial pull-out tests on two DI specimens lined with IMain® and two DI specimens lined with Starline2000® are shown in Figure 2.12a and Figure 2.12b, respectively. The axial response of the more flexible Starline2000® is sensitive to internal water pressure,  $p_w$ , applied in the lined DI specimen during testing to reflect field conditions. Therefore, Starline2000® was tested for two cases: 1) without any internal water pressure (Specimen CU G1), and 2) with  $p_w = 517$  kPa (Specimen CU G4) which is typical of many water mains in service. The results from the axial pull tests for DI specimens lined with IMain® and Starline2000® in Figure 2.12a and Figure 2.12b, respectively, were used to develop bilinear fitting curves, also shown in Figure 2.12a and Figure 2.12b, to capture joint behavior during TGD in the FE simulations.

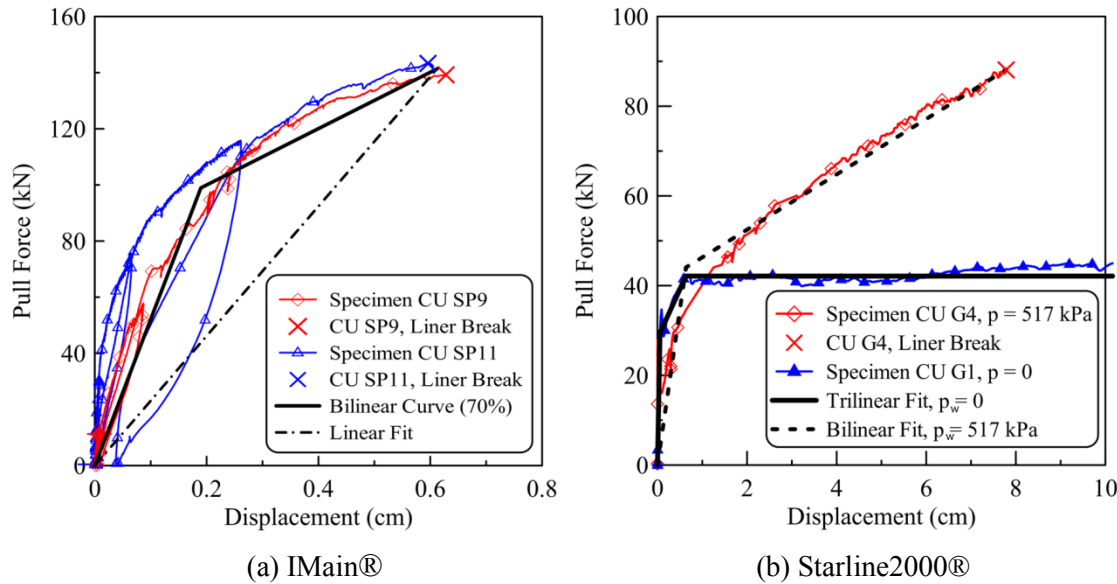


Figure 2.12. Axial response of (a) DI pipe specimens lined with IMain®, and (b) DI pipe specimens lined with Starline2000®.

The bilinear force vs. displacement relationships in Figure 2.12a and Figure 2.12b were introduced in the FE model, and the baseline case was modified to account for rehabilitation with each of the IMain® and Starline2000® liners. The numerical results for a lined pipeline crack with the bilinear relationships in Figure 2.12a and Figure 2.12b show mobilized force and displacements in response to the Rinaldi ground motions for the baseline case of 112.3 kN and 1.48 mm for the IMain® liner, and 75.9 kN and 5.81 mm for the Starline2000® liner. These forces and displacements are significantly smaller than the liner failure loads and displacements from pull-out tests. Additional numerical analyses show that liner failure occurs at 200% Rinaldi for the IMain® and 260% for Starline2000® liner.

## **2.6 Experimental Evaluation of CIPP Seismic Performance**

The seismic performance of pipelines rehabilitated with CIPP linings was also investigated experimentally in the twin re-locatable shake table facility of the Structural Engineering and Earthquake Laboratory (SEESL) at the University at Buffalo (UB). Full scale dynamics tests were performed on DI pipelines lined with IMain® and Starline2000® to investigate the limits on their seismic response [2.23].

All DI specimens used in this work were supplied by the Los Angeles Department of Water and Power (LADWP) with an interior 3.3 mm-thick mortar coating, consistent with LADWP practice. Pipeline test sections were lined from one end to the other in accordance with typical field installation procedures by Insituform

Technologies, Inc. (ITI) and Progressive Pipeline Management, LLC. The pipeline specimens used in full-scale testing were 9.14-m long and contained two lined DI joints at a separation of 3.75m. Test specimens were also prepared in a similar fashion for pull-out and flexure tests on typical lined joints.

The tests were performed to investigate the force vs displacement behavior of the lined joints and the potential for debonding of the lining between the joints. For this case, it was not known if the liner would detach from the host pipe over the pipeline length between the joints.

Figure 2.13a shows a typical test setup for the simulation of seismic wave propagation across two adjacent push-on joints in a pipeline. Strain gages, displacement transducers, accelerometers, differential pressure cells, and several video cameras were installed to monitor the seismic response. Acoustic emission and ultrasonic guided waves inspections were carried out for tests on specimens lined with IMain® to evaluate the extent of debonding between the DI pipe and the liner. Figure 2.13b shows a photo of a DI joint with acoustic monitors, strain gages, and DCDTs. As shown in Figure 2.13a, the pipeline specimens were clamped to two shake tables with a support pedestal at the center of the test specimen.

Axial joint movements were derived from the FE simulations of seismic wave interaction with jointed CIPPs, as previously discussed. Joint input motions derived from FE simulations account for soil-pipeline interaction, and, therefore, no soil was

required in the experiments. The pipeline specimens were pressurized internally with  $p_w \approx 345 \text{ kPa}$  before and during each test to simulate field conditions. Asynchronous translational motions, derived from FE simulations, were applied to the east and west shake tables causing differential axial movements at the joints.

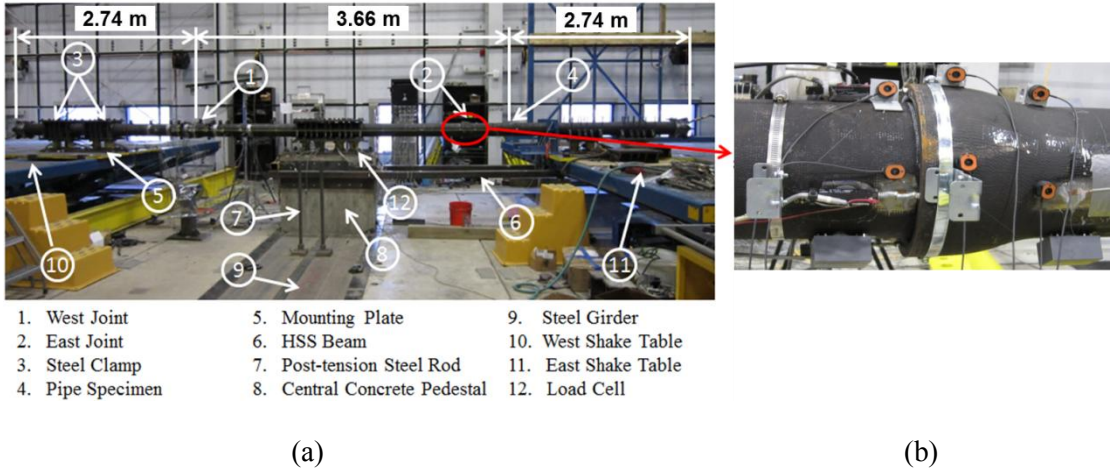


Figure 2.13. (a) Overview of dual table tests. (b) Close-up view of tested joints and instrumentation [2.23].

The axial joint motions from FE simulations with the Rinaldi ground motion record were scaled from 50% to approximately 200% during testing with IMain®, and from 50% to 310% during testing with Starline2000®, and were applied to the shake tables. Figure 2.14 and Figure 2.15 show results from the dual shake table tests on double-joint DI pipeline specimens that were lined with IMain® and Starline2000®, respectively. The results from the dynamic tests in Figure 2.14 and Figure 2.15 were provided by Zhong [2.23]. Figure 2.14a and Figure 2.14b show the hysteretic response at the west and east joint, respectively, of a double joint specimen lined with IMain® that was subjected to the Rinaldi ground motion scaled up to 200%. Also shown is the

bilinear fit curve based on the axial pull tests with IMain® that are presented in Figure 2.12a. The bilinear force vs displacement curve compares well with both the axial pull and shake table test results in Figure 2.12a and Figure 2.14. The west joint axial displacement at liner failure was 6.6 mm at a force 148 kN. The liner in the east joint did not fail, and its hysteretic response is shown in Figure 2.14b. Test results after failure in Figure 2.14a show the absence of axial load capacity and stiffness at the west joint.

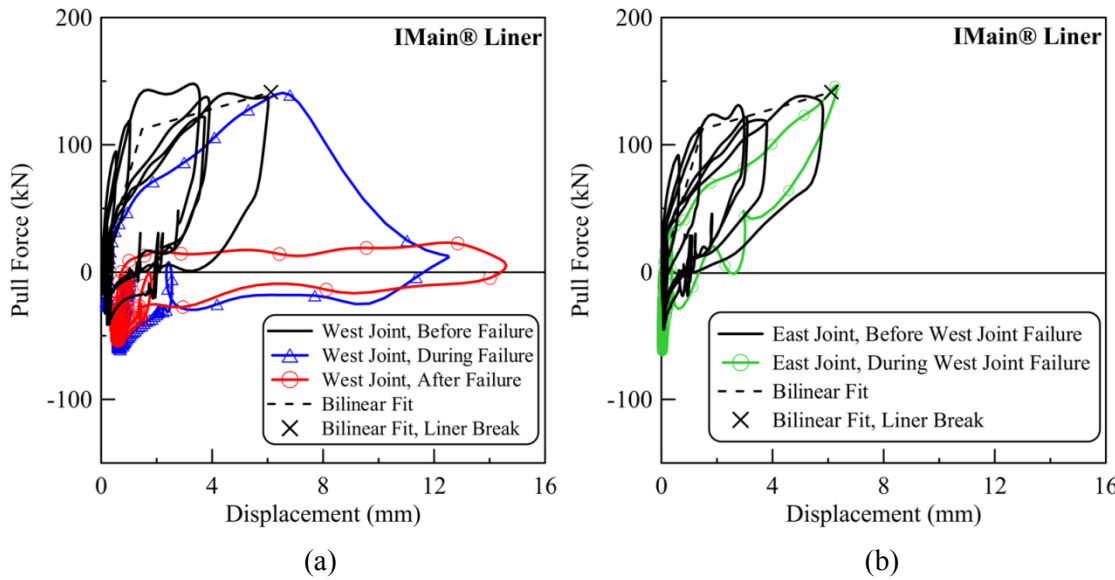


Figure 2.14. Force vs joint opening hysteretic response from dynamic testing: (a) West joint IMain® liner before failure, IMain® liner during failure at 200% of Rinaldi, IMain® liner after failure at 200% of Rinaldi, and bi-linear force vs displacement curve. (b) East joint IMain® liner before West Joint IMain® liner failure, IMain® liner at 200% of Rinaldi and bi-linear force vs displacement curve.

Figure 2.15a and Figure 2.15b show the hysteretic response of the west and east joint, respectively, of a double joint specimen lined with Starline2000® during the application of the Rinaldi record. Both joints demonstrated highly ductile behavior in

the longitudinal direction which is reflected through flat peak force plateaus in Figure 2.15a and Figure 2.15b in addition to significant de-bonding and delamination between the liner and pipeline during dynamic testing [2.23]. The liner in the west joint failed at peak force of 57 kN and joint offset 42.2 mm during the application of Rinaldi scaled at an equivalent of 310% of the original Rinaldi motion. The liner in the east joint did not fail, and its hysteretic response is shown in Figure 2.15b. The test results after failure in Figure 2.15a confirm the absence of axial load capacity and stiffness at the west joint due to failure.

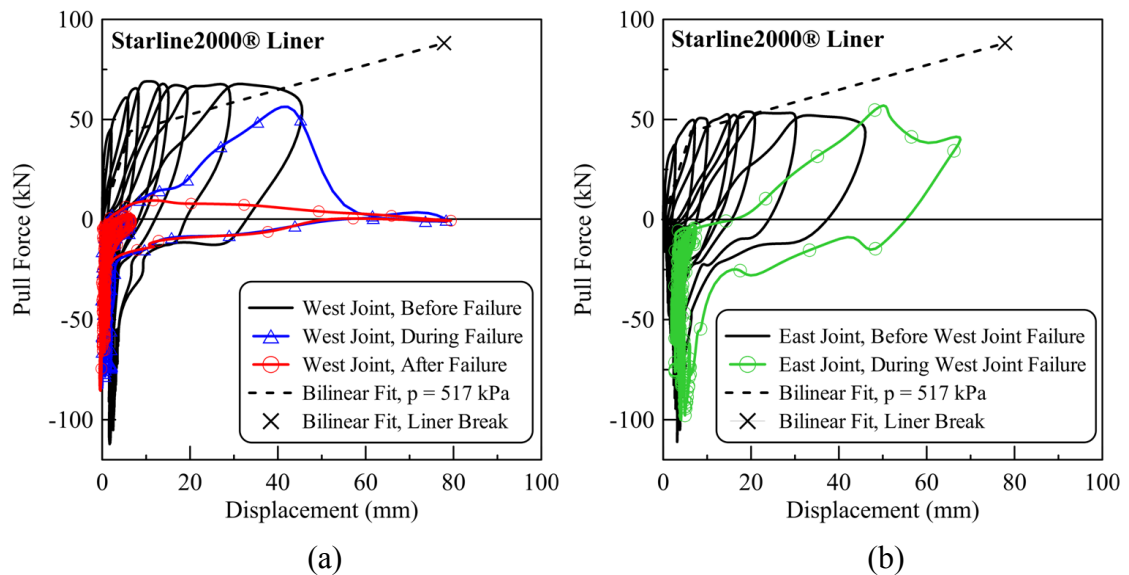


Figure 2.15. Force vs joint opening hysteretic response from dynamic testing: (a) West joint Starline2000® liner before failure, Starline2000® liner during failure at 310% of Rinaldi, Starline2000® liner after failure, and bi-linear force vs displacement curve. (b) East joint before West joint Starline2000® liner failure, Starline2000® liner at 310% of Rinaldi, and bi-linear force vs displacement curve.

Shown in the figures is the bilinear fit derived from axial pull tests on specimens with Starline2000® under pressure  $p_w = 517$  kPa that was previously presented in

Figure 2.12b. The bilinear joint response does not fit the force vs displacement test data as well as the IMain® bilinear response matches the dynamic test results. Repetitive loading of the Starline2000® liner was accompanied by significant debonding and relatively large axial movement before failure. Although the lined joints showed lower axial loads compared to those of the pull-out tests, they were more flexible and able to accommodate more displacement. Debonding adjacent to the joints was confirmed through visual inspections of the interior of the lined DI specimens as well as through acoustic emission and guided ultrasonic wave inspections before and after the tests. Full debonding for the Starline2000® liner was confirmed to distances equivalent to 4 diameters adjacent to the joints. Such debonding allows the liner to stretch and accommodate axial movements, but is confined locally. Separation of the lining and pipe did not propagate for long distances between the joints. Some cracking of the mortar coating of the pipe specimens did occur, and was reflected in elevated acoustic emission signals after testing.

## **2.7 Conclusions**

Numerical studies and sensitivity analyses were performed to determine the most prominent form of deformation due to transient ground deformation (TGD) and used in the experimental design for full-scale testing on pipelines rehabilitated with cured-in-place pipe (CIPP) lining technology subject to seismic wave interaction. The following conclusions are drawn from the numerical and experimental results:

- The most prominent form of deformation in pipelines with weak joints and circumferential cracks subject to seismic wave propagation occurs in the axial pipeline direction. Non-axial deformations have negligible effect on seismic performance of pipelines before and after rehabilitation. The maximum axial deformation is approximately two to three orders of magnitude larger than non-axial deformations.
- The problem of seismic wave interaction with pipelines containing round cracks and segmented pipelines with locally weak joints can be simplified by considering only pipeline axial response. Analytical models and experimental design may likewise be simplified to focus on the axial pipeline direction.
- Pipeline diameter and especially soil shear resistance in the axial direction affect the maximum axial deformation,  $d_x$ , due to seismic wave interaction, with a decay rate that is described by power fitting curves with respect to soil shear resistance in the axial direction, and less significant reduction with respect to smaller pipe diameter.
- Numerical studies of the response of underground pipelines lined with CIPP linings to seismic wave interaction indicate mobilized forces and displacements in response to the Rinaldi ground motion significantly smaller than the liner failure loads and displacements from pull-out tests. Additional

numerical analyses show that liner failure occurs at amplitudes that are approximately 2 to 3 times greater than the Rinaldi record.

- Full-scale tests show that CIPP liners are able to accommodate successfully high intensity ground motions. The IMain® liner was able to sustain seismic wave interaction effects for as much as 200% of the Rinaldi ground motion, and the Starline2000® liner was able to maintain up to 310% of the Rinaldi ground motion effects. These experimental results compare favorably with numerical simulations using the same ground motions.

Large-scale dynamic tests show full debonding of the Starline2000® liner for distances of approximately 4 diameters from the joints. However, separation of the lining and pipe did not propagate over larger diameters, thus indicating that debonding was restricted to the vicinity of the joints.

The numerical and experimental studies of pipelines with structural discontinuities reinforced with CIPP liners show substantial improvements in pipeline response to seismic wave interaction. Pipelines retrofitted with two different types of linings, representing relatively rigid and flexible products, were able to accommodate substantial seismic velocity pulses. CIPP lining technology therefore provides significant benefits for seismic retrofitting in addition to the repair and increased longevity of aging in situ pipelines.

## REFERENCES

- [2.1] Toprak S, Taskin F. Estimation of earthquake damage to buried pipelines caused by ground shaking. *Natural hazards* 2007; **40**(1):1-24.
- [2.2] Ayala AG, O'Rourke M. Effects of the 1985 Michoacan earthquake on water systems and other buried lifelines in Mexico. *Technical Report*: US National Center for Earthquake Engineering Research (NCEER), 1989.
- [2.3] Jeon S-S, O'Rourke TD. Northridge earthquake effects on pipelines and residential buildings. *Bulletin of the Seismological Society of America* 2005; **95**(1): 294-318.
- [2.4] Elhmadi K, O'Rourke MJ. Seismic damage to segmented buried pipelines. *Earthquake Engineering & Structural Dynamics* 1990; **19**(4):529-539.
- [2.5] O'Rourke TD, Wang Y, Shi P. Advances in lifeline earthquake engineering. *Proceedings of the 13th World Conference on Earthquake Engineering*, Vancouver, British Columbia, Canada, 2005.
- [2.6] Ariman, T, Muleski GE. A review of the response of buried pipelines under seismic excitations. *Earthquake Engineering & Structural Dynamics* 1981; **9**(2):133-152.
- [2.7] Sun S, Shien S. Analysis of seismic damage to buried pipelines in Tangshan earthquake. Earthquake behavior and safety of oil and gas storage facilities, buried pipelines and equipment, PVP-77: American Society of Mechanical Engineers, New York, 1983, p. 365-7.
- [2.8] O'Rourke MJ, Liu JX. *Seismic design of buried and offshore pipelines*. Monograph No. 4: Multidisciplinary Center for Earthquake Engineering Research, Buffalo, NY, 2012.
- [2.9] O'Rourke TD. Lessons learned for lifeline engineering from major urban earthquakes. *Proceedings of the 11<sup>th</sup> World Conference on Earthquake Engineering*, Acapulco, Mexico, 1996.

- [2.10] Kramer SR, McDonald WJ, Thomson JC. *An introduction to trenchless technology*. Van Nostrand Reinhold, New York, NY, 1992.
- [2.11] American Water Works Association (AWWA). *Rehabilitation of water mains*. Manual of Water Supply Practices M28, Denver, CO, 2001.
- [2.12] Sterling RL. No-dig techniques and challenges. *Journal of GeoEngineering* 2010; **5**(3): 63-67.
- [2.13] Anderson JG. Extension of database on exceptional strong motion accelerogram. *Final Technical Report*: United States Geological Survey (USGS), 2012, available at <http://earthquake.usgs.gov/research/external/reports/G12AP20024.pdf>.
- [2.14] Shi P. *Seismic response modeling of water supply systems*. Ph.D. Dissertation: Cornell University, Ithaca, NY, 2006.
- [2.15] O'Rourke MJ, Bloom MC, Dobry R. Apparent propagation velocity of body waves. *Earthquake Engineering & Structural Dynamics* 1982; **10**(2):283–94.
- [2.16] Boresi AP, Sidebottom OM, Seeley FB, Smith JO. *Advanced mechanics of materials*. John Wiley & Sons. Inc. ( Vol.5): New York, 1978.
- [2.17] American Society of Civil Engineers (ASCE). Guidelines for the seismic design of oil and gas pipeline systems. Committee on Gas and Liquid Fuel Lifelines, ASCE Technical Council on Lifeline Earthquake Engineering: New York, 1984.
- [2.18] Pacific Earthquake Engineering Research Center (PEER). NGA Database, available at: <http://peer.berkeley.edu/nga/>. [accessed August 2011]
- [2.19] Folkman S. Water main breaks rates in the USA and Canada: a comprehensive study. *Technical report*: Utah State University Buried Structures Laboratory, City of Logan, Utah, 2012.

- [2.20] Jung JK, O'Rourke TD, Olson NA. Lateral soil-pipe interaction in dry and partially saturated sand. *J. Geotech. Geoenviron. Eng.* 2013; **139**(12):2028–2036.
- [2.21] Jung JK, O'Rourke TD, Olson NA. Uplift soil-pipe interaction in granular soil. *Can. Geotech. J.* 2013; **50**(7):744–753.
- [2.22] Bouziou D, Wham BP, O'Rourke TD, Stewart HE, Palmer MC, Zhong Z, Filiatrault A, Aref A. Earthquake response and rehabilitation of critical lifelines. *Proceedings of the 15th World Conference on Earthquake Engineering*, 2012, Lisbon, Portugal.
- [2.23] Zhong Z. Earthquake response and rehabilitation of critical underground lifelines reinforced with cured in place pipe liner technologies under transient ground deformations. PhD Dissertation: University at Buffalo, 2015. (In press)

## CHAPTER 3

### WATER DISTRIBUTION SYSTEM RESPONSE TO THE 22 FEBRUARY 2011 CHRISTCHURCH EARTHQUAKE

#### **Abstract**

The response of the Christchurch water distribution system to transient and permanent ground deformations (TGD and PGD, respectively) during the Canterbury Earthquake Sequence (CES) is evaluated in this chapter through spatial analysis. Repair regressions for different pipeline types are developed using the most accurate and complete water pipeline repair record data sets, and an assessment of earthquake-induced ground deformation is performed using high resolution light detection and ranging (LiDAR) data acquired before and after each of the main seismic events. The sensitivity of repair regressions to the degree of data resolution is addressed and quantified. Improvements in the screening criteria are discussed and applied in the data screening process. Repair regressions are developed through correlation of repair rates, expressed as repairs/km, with 1) spatial distribution of peak ground velocity outside liquefaction areas, and 2) differential ground surface vertical movement and lateral strain within areas affected by liquefaction. A detailed description of the analytical processes for repair regressions is included in this chapter and provides a documented framework for future investigations with data sets of similar size and complexity.

### **3.1 Introduction**

The Canterbury Earthquake Sequence (CES) in New Zealand involved four main earthquake events with magnitudes ranging from  $M_w$  5.8 and 5.9 to  $M_w$  7.1, and multiple events of lesser magnitude, including approximately 60 over  $M_w$  5.0, that affected the infrastructure of Christchurch [3.1]. Each main seismic event induced multiple episodes of widespread and severe liquefaction with large permanent ground deformation (PGD) levels that caused severe damage to underground lifelines. Systematic mapping and recording of damage in the water distribution system, as well as observations and measurements of transient ground motion and permanent ground surface movements, resulted in data unique in size and detail. The geospatial database discussed in this chapter includes high resolution Light Detection and Ranging (LiDAR) surveys before and after each main seismic event, maps of areas of liquefaction interpreted by aerial photography and lateral spreading observations, and detailed repair records of thousands of km of underground pipelines in the water distribution system. This chapter provides significant updates to and expansion of investigations by O'Rourke et al. [3.2] for analysis of underground pipeline performance during the CES.

The present study uses the most recent and improved water distribution network repair records provided by the Stronger Christchurch Infrastructure Rebuild Team (SCIRT). Additional information, removal of inconsistencies, and adjustments in repair locations have been made over several years during the reconstruction of

Christchurch that result in modifications to approximately 10% of the records used in the previous work. This study uses the most accurate and complete set of water distribution records.

High resolution LiDAR lateral movements on 4-m spacing were acquired for this study. These data represent a significantly higher degree of resolution than those associated with 56-m spacing, which originally were released by the Canterbury Earthquake Recovery Authority (CERA) [3.3] and used in the previous study. Not only does the higher degree of resolution support a more detailed assessment of lateral movements, but it also allows for an evaluation of the effects of scale by comparing the 4-m and 56-m data.

The use of higher resolution data and improvements in the data screening criteria are applied in this study to provide better correlations among pipeline damage, liquefaction-induced lateral ground strains, and liquefaction-induced differential vertical ground movements. Moreover, refinements in the geostatistical processing of ground motion data to include the effects of anisotropy are used in this work to develop correlations between pipeline damage and peak ground velocity (PGV).

This chapter provides a detailed description of the analytical processes for calculation of pipeline damage with respect to 1) spatially distributed PGV outside liquefaction areas, and 2) lateral ground strain and differential vertical ground movement within areas affected by liquefaction. Flow charts illustrating the steps in

the geospatial analysis are presented. The work described in this chapter involves processing and analysis of geospatial ground movement and infrastructure repair data sets of unprecedented size, and it is therefore important to document the methods for developing the data both for clarity and to assist in future investigations with data sets of similar size and complexity.

This chapter begins with a description of the GIS database, followed by a description of the spatial analysis of water pipeline damage. Probabilistic screening criteria are derived and applied in the analytical processes to develop robust correlations of pipeline damage with transient ground motion and permanent ground surface movement data.

### **3.2 GIS Database**

Geospatial data of the Christchurch water system, locations of pipeline repairs, and areas of observed liquefaction effects were collected from different sources and integrated into the database discussed in this study. The database also includes strong motion data available in the national earthquake information database by GNS Science [3.4] that were used to analyze the spatial distribution of the peak ground velocity (PGV) for each seismic event. High resolution LiDAR data, available through CERA [3.3], were used to analyze ground surface movements for each seismic event.

The database included in this study was used to evaluate the performance of the water distribution system in the Christchurch area during the 22 Feb. 2011 earthquake. Accurate system wide repair records are not available for the 4 Sept. 2010 earthquake. At the time of 13 June 2011 earthquake, the pipeline system was substantially affected by widespread damage and repairs such that its physical condition differed appreciably from what would normally be encountered in a pre-earthquake water distribution system. Focusing on the effects of the 22 Feb. 2011 earthquake, therefore, provides the best basis for developing relationships between pipeline damage and transient ground deformation (TGD) and PGD for the prediction of earthquake effects on other water distribution systems.

### **3.2.1 Strong Motion Datasets**

As explained by O'Rourke et al. [3.5], ground motion records from 40 stations were selected for spatial analysis related to the 22 Feb. 2011 earthquake. The selected records are located in the Christchurch area and were fully processed by GNS Science [3.4] to provide acceleration, velocity, and displacement time histories and response spectra. The processed data from GNS Science [3.4] are derived using a filter with corner frequencies of 25 Hz and 0.25 Hz, meaning that the ground motions are screened to focus on periods between 0.04 and 4 sec. The geometric mean peak ground velocity (GMPGV) was calculated for each station as the mean of the natural logs of the two maximum values of horizontal PGV recorded at the station and

available through GNS Science [3.4]. The spatial distribution of GMPGV for the 22 Feb. 2011 earthquake was estimated using the ground motion records. Detailed information about the methodology that was followed and the resulting contour map of GMPGV for the 22 Feb. 2011 earthquake are provided in this chapter.

### **3.2.2 Areas of Liquefaction**

The areas of liquefaction were interpreted from aerial photography and site observations. Observed liquefaction effects include sand ejecta, as well as ground cracking, lateral spreading and differential surface settlement. A GIS shapefile, available through the Canterbury Geotechnical Database [3.6] and showing the areas of observed liquefaction effects for the 22 Feb. 2011 earthquake, was used in this study. The mapped boundaries of the liquefaction zones were defined by visible surface features, and thus, do not include the effects of liquefaction at depth outside the areas with surface evidence. The areas of observed liquefaction were therefore expanded to account for a zone of influence at the perimeter of the liquefaction areas that affects underground pipelines. The zone of influence of underground pipeline damage was taken as 125 m, which is approximately one-half a typical street length in a residential neighborhood and is consistent with the distance that significant pullout forces can be transmitted longitudinally along underground pipelines [3.7]. These areas are described in this chapter as the areas of liquefaction effects.

### 3.2.3 High Resolution LiDAR Datasets

Airborne LiDAR data were collected before and after each of the four main earthquakes. LiDAR surveys were conducted by AAM Brisbane (AAM) and New Zealand Aerial Mapping (NZAM) after each of the significant earthquakes [3.8]. Pairs of these data were used by GNS Science [3.4] under contract with Tonkin & Taylor Pty Ltd (T&T), Christchurch, New Zealand, to determine horizontal and vertical ground movements developed during the CES.

LiDAR lateral movements on 56-m spacing are available through the Canterbury Geotechnical Database [3.9]. In addition, LiDAR movements were acquired in this study to evaluate lateral and vertical movements on a consistent high resolution basis of 4-m and 5-m spacing, respectively. Acquisition of lateral and vertical movement data on 4-m and 5-m grids, respectively, provides resolution of movement at a scale similar to a typical segmented pipeline length of 6 m.

The NZAM LiDAR give a fundamental vertical accuracy of  $\pm 10$  cm for areas of open ground with hard surfaces, and the AAM LiDAR give a fundamental vertical accuracy of  $\pm 7$  to  $\pm 15$  cm [3.8]. The AAM LiDAR horizontal accuracy, compared to land survey measurements supplied by the Christchurch City Council (CCC), Land Information New Zealand (LINZ) and Environment Canterbury, is 40 to 55 cm [3.8].

The vertical and horizontal ground surface movements developed by pairs of LiDAR data sets were used to develop grids of differential vertical ground movement

and lateral ground surface strain, respectively, which are discussed in detail in this chapter. Pipeline damage assessments were performed in areas of liquefaction through correlation of pipeline damage with these data sets.

### **3.2.4 Pipeline Repair Datasets**

Approximately 1700 km of water pipelines, which were geocoded by CCC and SCIRT, were used in this study to represent the pipeline network before the 22 Feb. 2011 earthquake. The water distribution system spatial dataset developed by SCIRT, and sourced originally by CCC, provides the most complete picture of the system as of 4 Sept. 2010 and includes information about the type, diameter, material, length, and year of installation for each individual pipe in the network [3.10]. The water distribution system under study includes water mains and trunk lines with diameters between 75 and 600 mm, conveying the largest flows in the system. It does not include repairs to smaller diameter submains and customer service laterals.

Figure 3.1 shows the distribution of water mains and trunk lines in Christchurch City and Littleton Harbor superimposed on areas of liquefaction effects during the 22 Feb. 2011 earthquake. Further information about the development, statistics and quality of the water network database is provided also by O'Rourke et al. [3.2] and Cubrinovski et al. [3.10].

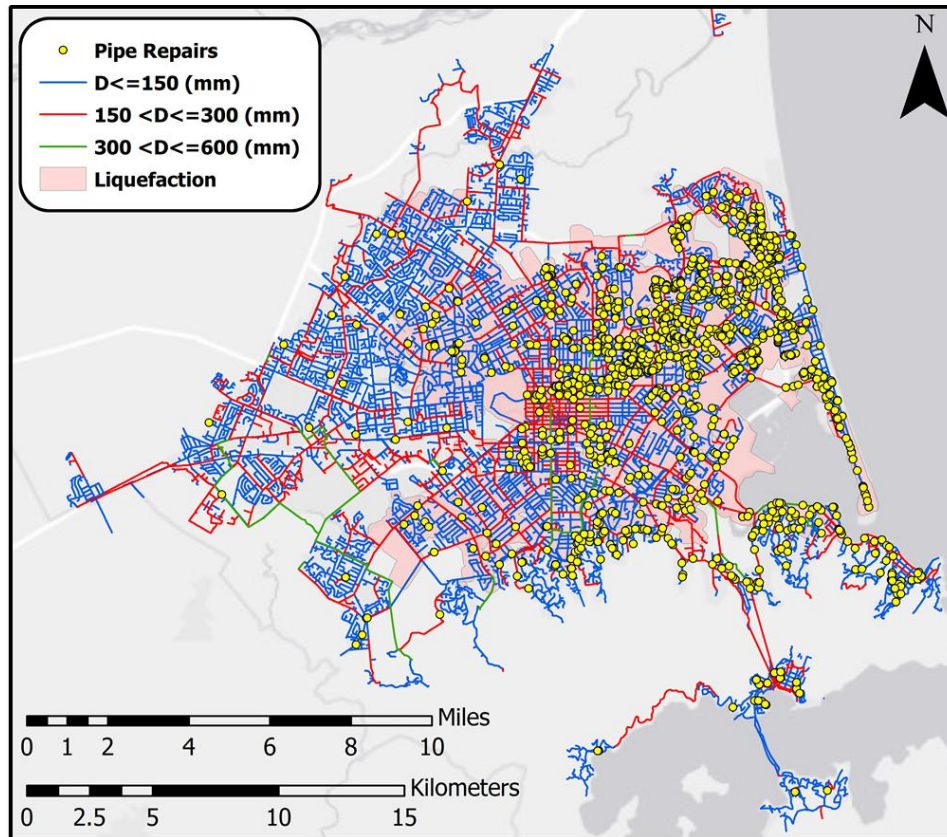


Figure 3.1. Potable water mains and trunk lines in Christchurch City and Littleton Harbor according to pipe diameter, and pipeline repairs for the 22 Feb. 2011 earthquake.

The water repair database provided by SCIRT and discussed in this chapter includes information on continuous daily repair records for re-establishment of services between the period from February 23, 2011 to March 11, 2013, after the occurrence of the 13 June 2011 and 23 December 2011 earthquakes and numerous aftershocks. O'Rourke et al. [3.2] studied the cumulative frequency of repairs in the water distribution system during the CES and determined the end of repair activities directly related to each main seismic event. Similar to the study by O'Rourke et al. [3.2], water distribution system repair records in the latest data set dating from

February 23, 2011 to April 15, 2011 were related to the 22 Feb. 2011 earthquake and used in this study.

Each repair record provides information on type of repair, location, and time, but in some cases it does not provide enough information to determine if the mode of failure is a leak or pipe break (loss of continuity due to joint pullout or pipe separation after rupture). Information about the pipe material, diameter, and length was assigned to each repair record based on a unique pipe identifier that was included in both the repair and the network spatial data sets.

### **3.3 Spatial Analysis of Water Pipeline Damage**

Pipeline repair rates (RRs), expressed as repairs/km, were evaluated through spatial analysis with respect to 1) areas outside of liquefaction effects where TGD is likely to be the primary cause of damage, and 2) areas inside of liquefaction effects, where PGD is likely to be the primary cause of damage. Using the databases described above, the spatial distribution of damage in the water distribution system during the 22 Feb. 2011 earthquake was quantified and is summarized in Table 3.1. The table provides information pertaining to pipeline length, repairs, and RRs for asbestos cement (AC), cast iron (CI), polyvinyl chloride (PVC), and modified polyvinyl chloride (MPVC) pipes in the water distribution system, including locations inside and outside areas of liquefaction effects. The category of “other” includes pipe types that

were individually present in the network in quantities too small to provide statistically robust correlations.

The use of RR as a normalized indicator of pipeline damage allows for comparison of the vulnerability of different pipe types relative to their total length in the water distribution network. As shown in Table 3.1, the RRs for AC and CI pipes are similar and approximately 4 times greater than PVC pipe RRs, and 6 to 15 times greater than MPVC pipe RRs. The average RRs inside the liquefied areas are at least 4 times greater than RRs in areas without liquefaction effects for all pipe types.

Table 3.1. Statistics of water main and trunk line pipeline repairs and repair rates in both liquefaction and non-liquefaction areas for different water pipe types.

	Pipe Material	Pipe Length (km)	Repairs	Overall Average RR	% Repairs in LIQ <sup>1</sup> areas	% Pipeline in LIQ <sup>1</sup> areas	% Damaged Pipeline in LIQ <sup>1</sup> areas	% Damaged Pipeline in Non LIQ <sup>1</sup> areas	Average RR in LIQ <sup>1</sup> areas	Average RR in Non LIQ <sup>1</sup> areas
22 February 2011	AC	867.2	1024	1.18	85%	47%	16%	3%	2.15	0.33
	CI	194.4	255	1.31	89%	67%	14%	3%	1.73	0.44
	PVC	213.6	68	0.32	93%	52%	5%	1%	0.56	0.05
	MPVC	149.7	13	0.09	100%	33%	2%	0%	0.27	0.00
	Other	305.4	142	0.47	83%	83%	4%	4%	0.46	0.47
	Total	1730.3	1502	0.87	86%	55%	11%	2%	1.36	0.27

<sup>1</sup> LIQ: Areas of liquefaction effects.

Table 3.1 also provides information about the distribution of repairs and pipelines inside and outside the areas of liquefaction effects that verifies prevalence of damage in the liquefied zone. More than 80% of repairs for each pipe type are located inside the expanded areas of liquefaction effects, whereas the percentage of pipelines for each pipe type inside the liquefied zone is not as high. The percentage of damaged

pipelines inside and outside the areas of liquefaction effects is also used in Table 3.1 as an indicator of damage and shows that pipeline damage was mostly concentrated inside the liquefied zone. According to Table 3.1, AC and CI pipes were most severely affected by the 22 Feb. 2011 earthquake, whereas PVC and MPVC pipes performed significantly better.

### 3.4 Screening Criteria

When sampling data to correlate RR with respect to ground deformation it is important to ensure that the intervals of pipeline length selected for calculating RR are sufficient to produce meaningful correlations. The screening criteria developed by O'Rourke et al. [3.2] were used to ensure that pipeline intervals of sufficient length were chosen.

As recommended by previous researchers [3.11] [3.12], pipeline damage is assumed to follow a Poisson distribution, from which the sampling length is selected in accordance with

$$(1 - \alpha)p \leq (RR)x \leq (1 + \alpha)p \quad (3.1)$$

in which  $p$  is the actual number of repairs,  $\alpha$  is a fraction of actual repairs,  $RR$  is repair rate, and  $x$  is sampling length. For a Poisson distribution, the mean is  $\mu = (RR)x$  and standard deviation is  $\sigma = [(RR)x]^{1/2}$ .

The confidence level corresponding to the sampled number of repairs falling within  $\pm \alpha$  of the actual repairs can be estimated by recognizing that the sampled repairs follow a normal distribution in accordance with the central limit theorem. For a confidence interval,  $\beta_c$ , and standard normal deviate,  $\phi^{-1}(\beta_c)$ , the lower and upper bounds of Equation 3.1 are

$$\mu \pm \phi^{-1}(\beta_c)\sigma = (1 \pm \alpha)p \quad (3.2)$$

Combining Equations 3.1 and 3.2 with  $p = (RR)x$  results in

$$x \geq \frac{[\phi^{-1}(\beta_c)]^2}{\alpha^2(RR)} \quad (3.3)$$

This expression provides the minimum sampling length,  $x$ , needed for a confidence interval,  $\beta_c$ , that the actual number of repairs falls with  $\pm \alpha$  of the mean value  $(RR)x$ . It allows for sampling, or data screening, criteria to be administered by selecting  $\beta_c$  and  $\alpha$ . For this study  $\alpha$  was chosen as 0.5, and a relatively high confidence interval  $\geq 90\%$  was applied in most cases. As discussed later, the confidence interval was reduced in some cases to produce additional RR data so that the linear regressions derived from these data would cover a broader range of ground deformation parameters.

The screening criteria are reflected in Equation 3.3 which is straightforward and simple to apply. Equation 3.3 was developed to provide a rational means for data sampling, and its application improved dramatically the data screening process.

### **3.5 Analytical Process for Peak Ground Velocity**

As previously described, the response of the water distribution system in Christchurch outside the areas of observed liquefaction was evaluated through pipeline RR correlations with GMPGV. The spatial distribution of GMPGV was estimated from spatial interpolation using recorded ground motions processed and provided by GNS Science [3.4]. The spatial interpolation technique employs an ordinary kriging model with a spherical variogram similar to the study by Jeon and O'Rourke [3.13]. The spherical variogram used in this study accounts for anisotropy to incorporate the influence of direction dependency. Figure 3.2a and Figure 3.2b show the areas of liquefaction effects, water distribution pipelines, repairs outside liquefied areas, and 10 cm/sec contours of GMPGV for the 22 Feb. 2011 earthquake, pertaining to AC and CI distribution mains and trunk lines, respectively. The figures illustrate the framework for the data screening analytical process.

ArcMap 10.1 software [3.14] was used to perform spatial data analysis, and details of the analytical process are provided in Appendix A. Spatial interpolation of the ground motion data with ordinary kriging, and the assumption of anisotropy, was used to generate the GMPGV surface in intervals of 10 cm/sec as shown in Figure 3.2.

Areas of liquefaction effects, also shown in Figure 3.2, were used to identify pipelines and repairs affected by liquefaction. Pipelines and repairs inside these areas were excluded from the analytical process based on the assumption that they were primarily associated with PGD effects. Pipelines affected by landslides and rock falls during the 22 Feb. 2011 earthquake were also removed in a similar manner assuming that pipelines at elevation above 50 m in Port Hills were primarily affected by landslide-related PGD.

Using the spatially located pipelines and repairs, the RR for a given interval of GMPGV was calculated by dividing the number of repairs for a particular type of pipeline by the kilometers of that pipeline type within a contour interval of 10 cm/s. The resulting RR was then associated with a value of GMPGV and was used as a single data point in the RR correlations that followed. A similar process was adopted inside the areas of liquefaction effects, as described later in the chapter.

Following the calculation of RR in each interval of GMPGV was the application of the screening criteria in Equation 3.3 with the appropriate confidence level and GMPGV interval size to produce meaningful RR correlations. Regression analyses were performed for RR vs GMPGV for AC and CI pipelines using data points derived from the analytical process described in Appendix A, and the results are presented in Figure 3.3a and Figure 3.3b. A sufficient number of PVC pipeline repairs was not available to develop RR vs GMPGV correlations even for relatively low confidence levels while screening the data. The RRs for AC pipelines and various GMPGVs for

the 22 Feb. 2011 earthquake shown in Figure 3.3a were combined with similar data reported by Jeon [3.15] for AC pipelines damaged during the 1994 Northridge earthquake. The linear regression for both earthquakes is statistically robust with  $r^2 = 0.94$  and random distribution of residuals.

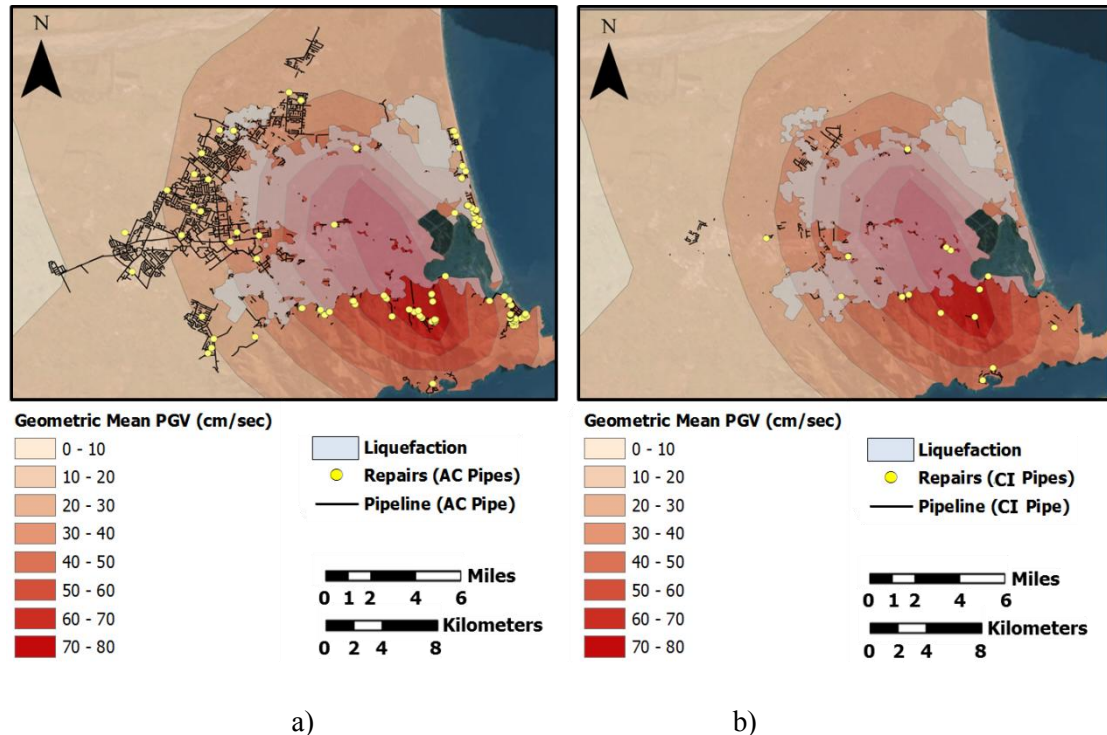


Figure 3.2. a) 22 Feb. 2011 earthquake AC pipeline layout and repairs; map of GMPGV and liquefaction is the background. b) 22 Feb. 2011 earthquake CI pipeline layout and repairs; map of GMPGV and liquefaction is the background.

Using similar techniques for CI pipelines, two data points for the 22 Feb. 2011 earthquake are combined with historical data reported by Jeon and O'Rourke [3.13] to develop the linear regression in Figure 3.3b. The data for the 22 Feb. 2011 earthquake are related to relatively high GMPGVs, and plot slightly above the linear regression using historical data. The linear regression combining all earthquakes provides good

fit of the data with  $r^2 = 0.84$ . The linear regressions for AC and CI pipelines using data from the 22 Feb. 2011 and previous earthquakes are comparable and indicate similar response between AC and CI pipelines to PGV.

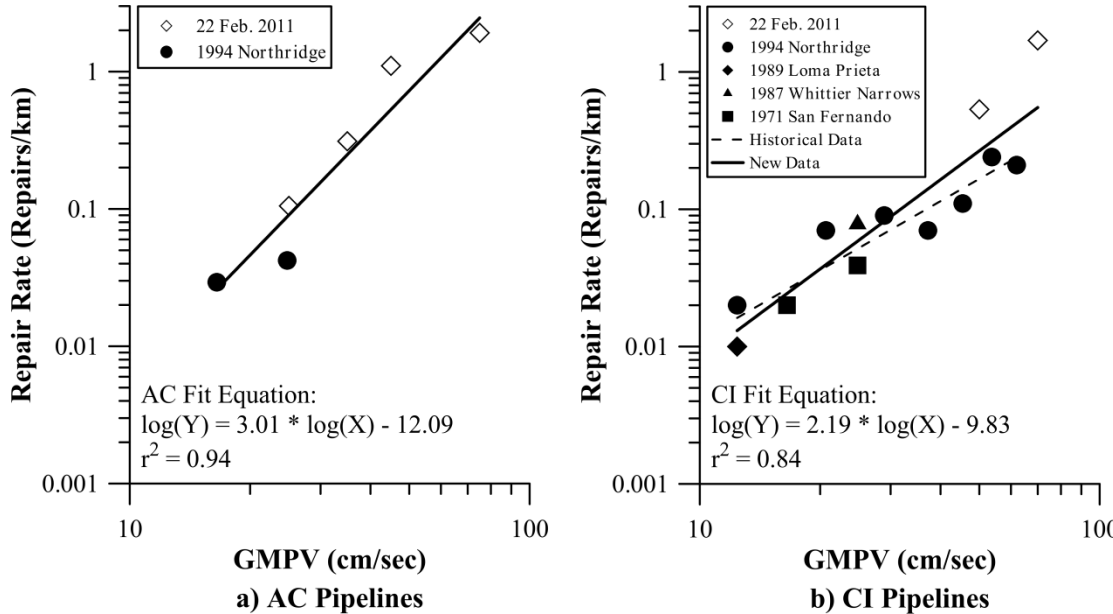


Figure 3.3. Repair rate vs. GMPGV for a) AC pipelines and b) CI pipelines.

**3.6 Analytical Process for Differential Vertical Ground Movement**

Measurements of ground surface elevation before and after each main seismic event were acquired through high resolution LiDAR surveys in Christchurch area and a digital elevation model (DEM) was developed for each LiDAR set [3.16]. Differential vertical ground surface movements were subsequently calculated both for each individual main seismic event and for sets of consecutive earthquakes as differences between pairs of DEMs. The set of vertical ground surface movements before and

after the 22 Feb. 2011 earthquake was used to develop RR correlations with differential vertical ground movement for the 22 Feb. 2011 earthquake. A dislocation model of the vertical tectonic movements during the 22 Feb. 2011 earthquake provided by GNS Science [3.4] was applied to the set of vertical ground surface movement to correct the data for tectonic movement. Figure 3.4 shows the LiDAR area in Christchurch combined with the water distribution pipeline network and repairs for AC, CI, and PVC water pipelines. Areas of liquefaction effects are also shown in Figure 3.4. RR correlations were performed using repairs and pipelines located in the zone defined by the intersection of liquefaction effects and LiDAR area.

The differential vertical ground surface movements were used to calculate angular distortion,  $\beta$ , at the ground surface and evaluate the effects of differential vertical ground movement on pipeline damage. As discussed by O'Rourke et al. [3.2], angular distortion is the gradient of settlement between two adjacent LiDAR points

$$\beta = \frac{\delta z_1 - \delta z_2}{l_{12}} \quad (3.4)$$

where  $\delta z_1$  and  $\delta z_2$  are the vertical movements of points 1 and 2, respectively, and  $l_{12}$  is the distance between the two points in the horizontal plane.

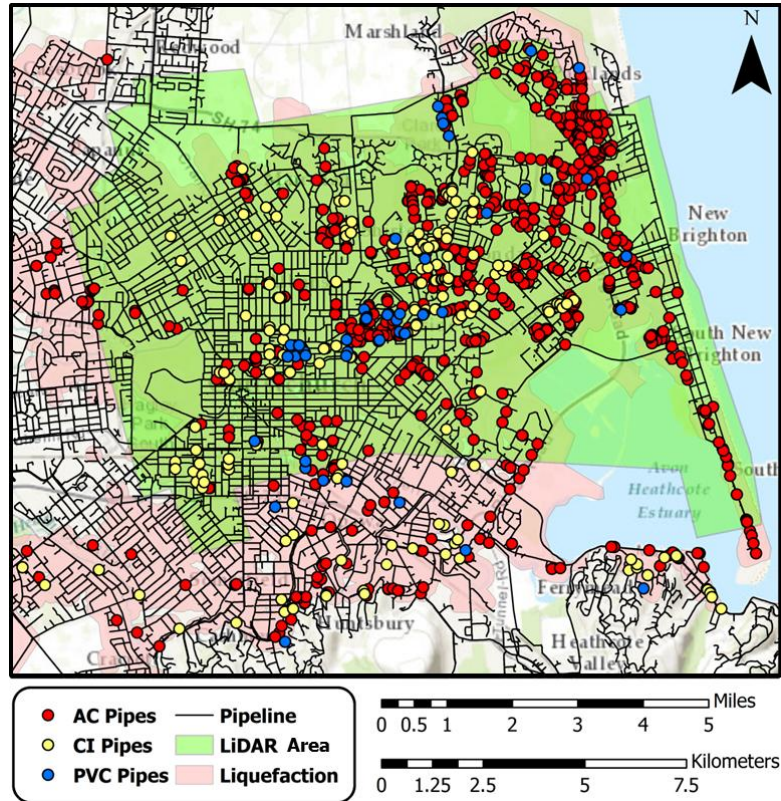


Figure 3.4. 22 Feb. 2011 earthquake water pipeline layout and repairs on AC, CI, and PVC water pipelines; LiDAR area and areas of liquefaction effects are shown in the background.

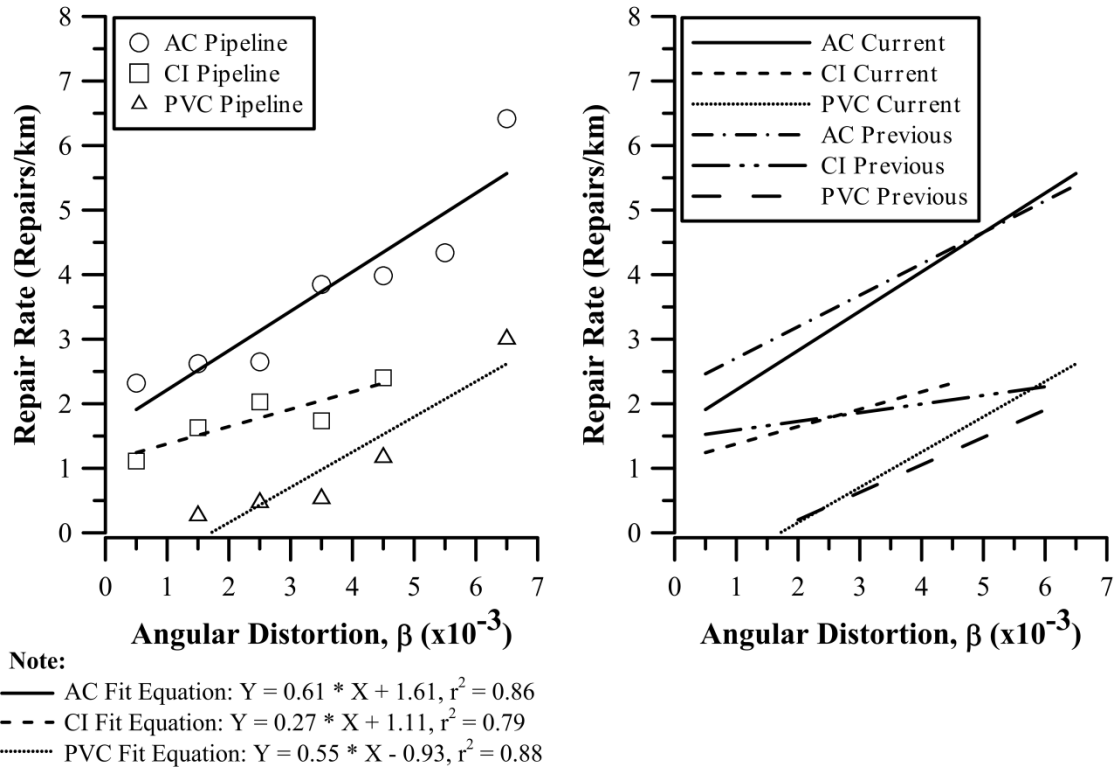
Angular distortion,  $\beta$ , is a dimensionless parameter that allows for calculation of relative vertical movement between LiDAR points, eliminating inherent errors in the measurements such as GPS network error and approximations with the reference surface. In this study it was calculated on a 5-m grid with a third order finite difference approach that uses a 3-by-3-cell moving window and weighting factors assigned to each neighboring cell based on their distance from the cell at the center of the window [3.17].

The analytical process for RR correlations with  $\beta$  is described in detail in Appendix B. Vertical ground movements derived from LiDAR surveys were used as input for the calculation of  $\beta$ . Pipelines and repairs inside the areas of observed liquefaction effects were selected for RR correlations with  $\beta$ . As previously described, pipelines affected by landslides and rock falls were excluded from the analytical process for  $\beta$ .

Similar to the linear regression analysis of RR vs GMPGV, RR for a given interval of  $\beta$  was calculated by dividing the number of repairs for a particular type of pipeline by the kilometers of that pipeline type within the same interval. The interval size for  $\beta$  is  $1 \times 10^{-3}$ . The calculated RR was assigned to the appropriate value of  $\beta$ , and used as a single data point in the RR correlations that followed. A similar binning process was followed for RR correlations with lateral ground strain.

The screening criteria in Equation 3.3 were applied to the data points derived by the binning process for AC, CI, and PVC water pipelines. The confidence level during the screening process was adjusted to account for the number of repairs, which declines progressively for AC, CI, and PVC pipelines. By relaxing the confidence interval in the screening criteria, more RR values are provided to develop a linear regression for each pipe type over a suitable range of  $\beta$ . Confidence levels of 95%, 90%, and 75% were used in the screening criteria for correlations of RR with  $\beta$  for AC, CI, and PVC pipelines, respectively. The results from the regression analysis for  $\beta$  are presented in Figure 3.5a. The linear regressions for all three pipe types provide a

good fit of the data with  $r^2$  values of 0.86, 0.79, and 0.88 for AC, CI, and PVC pipelines, respectively. RRs for AC pipelines plot 1.3 to 2.2 times higher than CI, and 2.1 to 9.9 times higher than PVC. The results indicate that the best performance with respect to  $\beta$  is shown by PVC pipelines.



a) Results with updated measurements      b) Comparison of current and previous results  
 Figure 3.5. Repair rate vs angular distortion for AC, CI, and PVC pipelines for the 22 Feb. 2011 earthquake.

Figure 3.5b compares the results of the current investigation, using the most recent and complete repair records, with the results of previous work [3.2]. With the exception of a decreased RR for AC pipelines using the new data, the regressions for each pipe type compare favorably with each other.

### **3.7 Analytical Process for Lateral Ground Strain**

Measurements of lateral ground movement derived from LiDAR surveys in Christchurch area were obtained through CERA [3.3]. The data sets include lateral movements in the east-west (EW) and north- south (NS) directions both for each main seismic event and for sets of consecutive earthquakes as differences between pairs of LiDAR point clouds. The lateral movements for each earthquake combination were calculated using a sub-pixel correlation method developed by Imagin'Labs Corporation, Pasadena, CA, and California Institute of Technology [3.8]. They were calculated on 4-m grids (8-m for the pre-earthquake LiDAR sets) from both ground and non-ground LiDAR points and averaged to provide movements in the EW and NS directions on 56-m grids.

Lateral ground movements at 4-m and 56-m grids were used in this study to calculate lateral ground strains. Similar to the calculation of angular distortion, a dislocation model of the tectonic movements in the EW and NS directions provided by GNS Science [3.4] was applied to lateral ground movements to distinguish ground movements due to PGD from tectonic movements. The spatial extent of the lateral ground movement data set used in this chapter is represented by the LiDAR area shown in Figure 3.4. The analytical process for lateral ground strain correlations based on the 4-m grid of lateral movements is described in additional detail in Appendix C. A similar process was followed for the calculation of lateral strains using the 56-m-grid lateral displacements.

The methodology for calculation of lateral ground strains was based on plane strain conditions for quadrilateral elements. The lateral ground movement data points were used as corners of square elements shown in Figure 3.6. As described by O'Rourke et al. [3.2], finite element formulations were used to determine horizontal ground strains in the center of the elements, according to the method described by Cook [3.18]. Pipeline damage on segmented pipelines, expressed as RR, is assumed to be caused by axial ground strains and related primarily to failure of the joints. The absolute maximum value of lateral ground strain,  $\epsilon_{HP}$ , in each elemental area of ground was used as a metric for RR correlations with lateral ground strain. Lateral ground strain  $\epsilon_{HP}$  is equal to the absolute maximum value of principal strains given by

$$\epsilon_{1,2} = \frac{\epsilon_x + \epsilon_y}{2} \pm \sqrt{\left(\frac{\epsilon_x - \epsilon_y}{2}\right)^2 + \left(\frac{\gamma_{xy}}{2}\right)^2} \quad (3.5)$$

Similar to RR correlations with  $\beta$ , pipelines and repairs inside the areas of liquefaction influence and excluding those above 50 m in elevation subject to landslides in the Port Hills were used for RR correlations with lateral ground strain. The RR for a given interval of strain was calculated similar to the RRs for  $\beta$ , by dividing the number of repairs for a particular type of pipeline by the kilometers of that pipeline type within the same interval. The interval size for lateral strain was adjusted to 0.2% for AC and PVC pipelines, and 0.05% for CI. The RRs were associated with the appropriate value of  $\epsilon_{HP}$  and were used as data points for RR correlations.

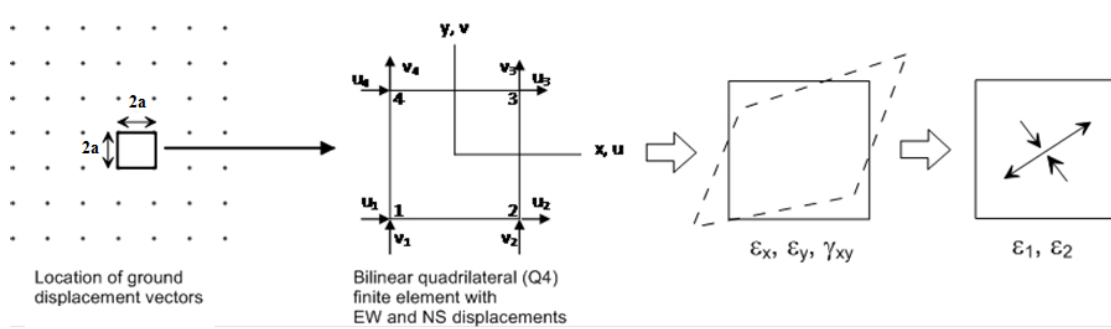


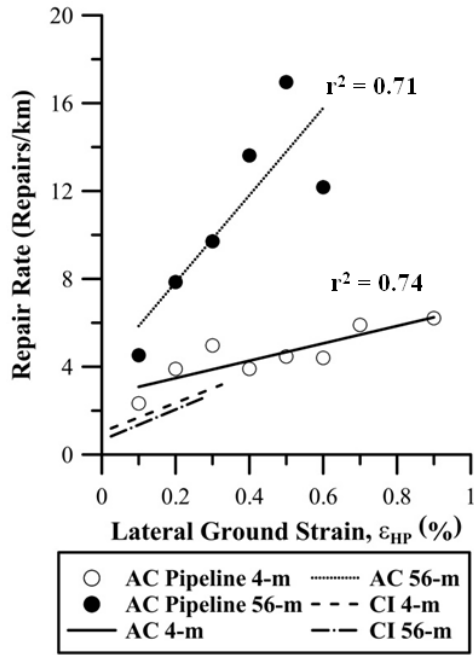
Figure 3.6. Process of calculating lateral ground strains from horizontal ground displacements.

The results for RR correlations with  $\epsilon_{HP}$  for AC, CI, and PVC pipelines are presented in Figure 3.7a through Figure 3.7c. The screening criteria were applied using confidence levels of 95%, 85%, and 75% for AC, CI, and PVC pipelines, respectively. Procedures similar to those for correlations with  $\beta$  were used, in which the confidence interval is relaxed for the progressively smaller number of repairs for AC, CI, and PVC. The linear regressions for all three pipe types provide a good fit of the data with high  $r^2$  values.

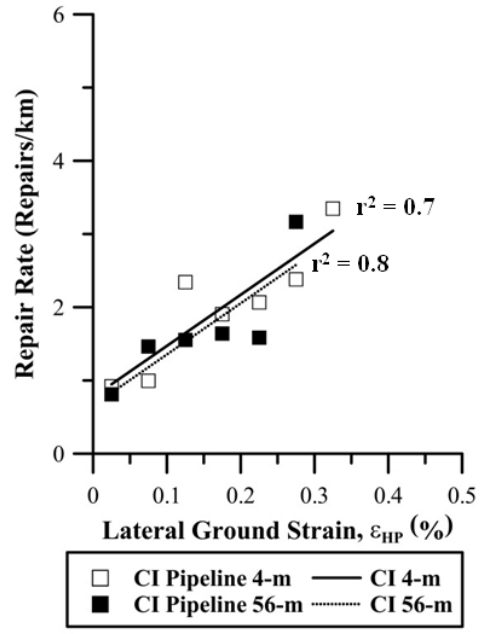
Comparison between RR correlations derived from 4-m and 56-m spacings of lateral strain shows significant differences for AC and PVC pipelines. Lateral strains at 56-m spacing in Figure 3.7a are related to RRs for AC pipelines that are 1.9 to 3.1 times higher than lateral strains at 4-m spacing in Figure 3.7a for the same levels of  $\epsilon_{HP}$ . Similarly, the PVC pipeline RRs for lateral strains at 56-m spacing in Figure 3.7c are up to 2.3 times higher than RRs for lateral strains at 4-m spacing in Figure 3.7c for the same levels of  $\epsilon_{HP}$ . On the contrary, RR correlations for CI pipelines in Figure 3.7b derived from lateral strains at 56-m and 4-m spacing are in good agreement.

The difference in RR correlations with  $\epsilon_{HP}$  between lateral ground strains at 4-m and 56-m spacing reveals the sensitivity of RR correlations to the scale used for discretization of the ground parameters used in the analysis. As shown in Figure 3.7a and Figure 3.7c, for the same level of RR, the value of  $\epsilon_{HP}$  at 4-m spacing is significantly higher than the value of  $\epsilon_{HP}$  at 56-m spacing for AC and PVC pipelines. Lateral movements at 56-m spacing result in a relatively coarse lattice of lateral ground strains that does not capture local effects with high horizontal strain.

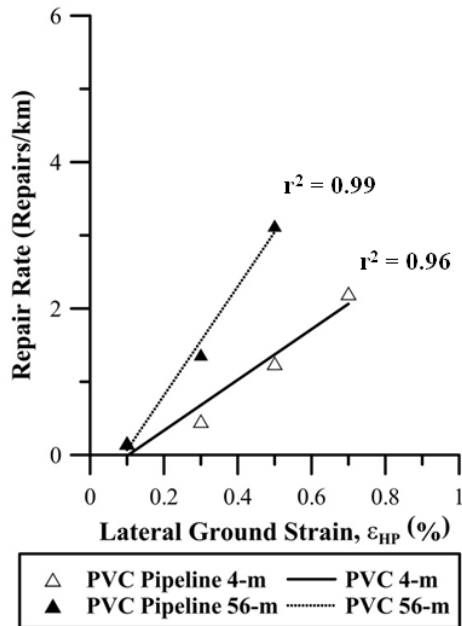
If pipelines traverse areas of locally high strain, the associated levels of pipeline repair will be correlated with lower strains averaged at 56-m spacing. Pipelines with un-cemented joints vulnerable to pullout, such as AC and PVC pipelines, were concentrated in the eastern areas of Christchurch where locally high strain fields developed in response to liquefaction. As a result, higher levels of repair are correlated with lower strains using a 56-m spacing, which does not capture many of the locally high strain fields that are covered by a 4-m spacing. This bias is reflected in the higher regression slopes of RR vs  $\epsilon_{HP}$  for AC and PVC pipelines because RRs are correlated with  $\epsilon_{HP}$  that is often too low with a 56-m spacing.



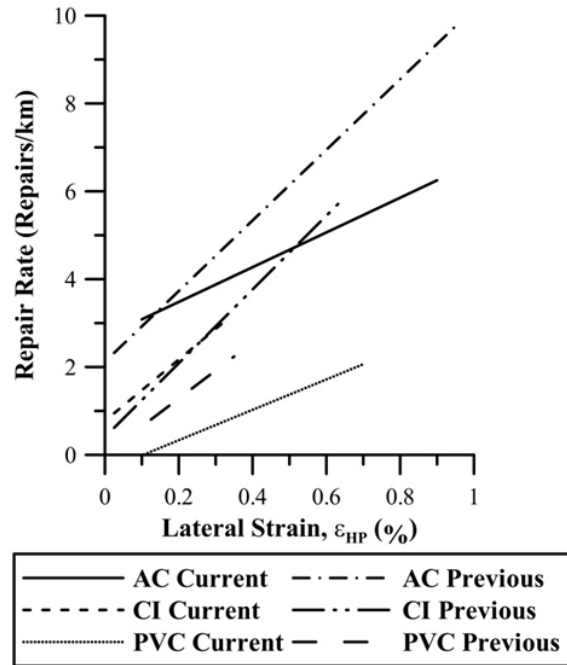
a)



b)



c)



d)

Figure 3.7. Correlations of repair rate with lateral ground strain at 4-m and 56-m spacing for a) AC, b) CI, and c) PVC pipe materials for the 22 Feb. 2011 earthquake, and d) comparison between current and previous investigations.

A similar increase in regression slope is not shown for CI pipelines, which typically have substantial resistance to axial pullout on the order of 450 kN for a nominal 150-mm-diameter CI main with lead-caulked joints [3.19]. An examination through GIS of CI pipeline repair locations relative to lateral ground strain patterns shows that CI pipelines were located in areas with significantly more uniform strains than AC and PVC pipelines. Uniform strain fields will reduce the effects of grid size on the resulting RR vs  $\epsilon_{HP}$  correlations.

Using the correlations of RR with  $\epsilon_{HP}$  at 4-m spacing in Figure 3.7a through Figure 3.7c, comparison among the results for AC, CI, and PVC pipelines indicates that AC pipelines sustained 1.4 to 2.1 times greater damage than CI, and 2.7 to 10.5 times greater than PVC pipelines.

Figure 3.7d compares the results of the current investigation with the results of previous work [3.2]. The regressions for AC and PVC pipelines based on 4-m LiDAR spacing plot lower with a reduced regression slope than those developed in previous work with 56-m LiDAR spacing. The regressions for CI pipelines compare favorably because the pipelines were located in relatively uniform strain fields for which the higher resolution at 4-m spacing does not show significant difference compared to 56-m spacing.

Of particular importance is that scale effects have a substantial impact on the inferred relationship between pipeline damage and lateral ground strain, and depend

on local variations in the strain field. High resolution data are needed to capture the influence of localized ground deformation. Computational modeling that utilizes regressions, such as those in Figure 3.7a through Figure 3.7c, need to account for scale effects, and should strive for the highest resolution possible at a scale equivalent to that of the structure being investigated.

### **3.8 Combined Effects of Differential Vertical Ground Movement and Lateral Ground Strain**

For a comprehensive procedure to evaluate pipeline damage, one must account simultaneously for the effects of lateral strain and differential vertical movement. Such a procedure was developed by Boscardin and Cording [3.20] for masonry and timber buildings subject to underground construction and mining-induced ground movements. Following this approach, pipeline RRs are correlated with both  $\beta$  and  $\epsilon_{HP}$ . Using the probabilistic criteria in Equation 3.3, there are sufficient repairs to develop correlations among RR,  $\beta$ , and  $\epsilon_{HP}$  for AC and CI pipelines. There is an insufficient number of repairs, however, to develop correlations with PVC pipelines even if the confidence interval is relaxed to a relatively low value when screening the data.

Lateral ground strains at 4-m spacing were used to correlate RR with  $\epsilon_{HP}$ . Pipelines and repairs were spatially intersected with  $\beta$  and  $\epsilon_{HP}$ , and RR was calculated for a given pair of  $\beta$  and  $\epsilon_{HP}$  intervals by dividing the number of repairs for a particular type of pipeline by the kilometers of that pipeline type within the same pair of intervals.

The interval for  $\beta$  was  $1 \times 10^{-3}$ , and for  $\epsilon_{HP}$  was 0.2%. The RRs were associated with the appropriate pair of  $\beta$  and  $\epsilon_{HP}$  and were used as data points for RR correlations.

The screening criteria were applied for each set of data points and the confidence level was adjusted to 75% and 60% for AC and CI pipelines, respectively, to develop reasonably dense distribution of data across the largest  $\beta$  vs  $\epsilon_{HP}$  space. The data points that passed the screening process are shown in Figure 3.8a and Figure 3.8b for AC and CI pipelines, respectively.

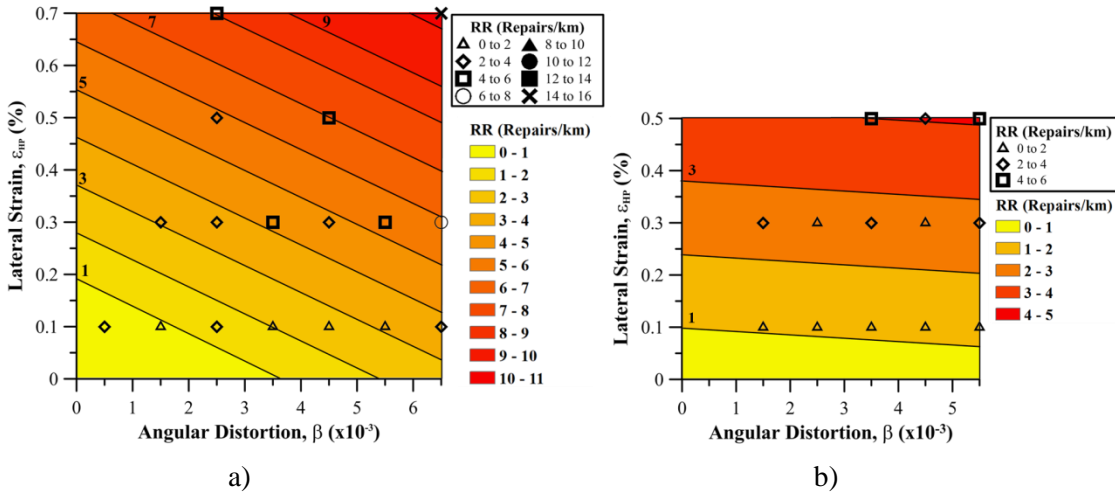


Figure 3.8. Repair rate vs lateral strain, and angular distortion for a) AC and b) CI pipelines.

The global polynomial interpolation method in ArcMap 10.1 [3.14] was used to fit a smooth surface of RR contours as illustrated in Figure 3.8. A first-order polynomial model was applied to the data. The resulting contour surfaces are presented in Figure 3.8a and Figure 3.8b for AC and CI pipelines, respectively. The extent of the data for CI pipelines is smaller than the extent of data for AC pipelines due to the higher

number of AC pipeline repairs that provide a more extensive database for sampling with respect to combined  $\epsilon_{HP}$  and  $\beta$ . Similar to Figure 3.5 and Figure 3.7, the results for AC and CI pipelines in Figure 3.8 show that AC pipelines sustained more damage compared to CI pipelines.

The correlations in Figure 3.8 represent a marked improvement over those presented previously by O'Rourke et al. [3.2], where the interval chosen for  $\epsilon_{HP}$  is too large. The selection of  $\epsilon_{HP}$  intervals in Figure 3.8 was guided by a study of the statistical distribution of lateral ground strains associated with the water pipeline network that is described in Chapter 5. The study shows that approximately 90% of the 4m x 4m  $\epsilon_{HP}$  cells overlying the pipeline network is associated with values of  $\epsilon_{HP} \leq 1\%$ . Similarly, 90% of the 5m x 5m  $\beta$  cells overlying the pipeline network is associated with values of  $\beta \leq 1 \times 10^{-2}$ . Based on these observations, the  $\epsilon_{HP}$  and  $\beta$  intervals in the sampling process were selected to reflect combined  $\epsilon_{HP}$  and  $\beta$  effects at a scale that is consistent with the actual ground deformations experienced by the majority of pipelines.

### **3.9 Conclusions**

The performance of the Christchurch water distribution system is evaluated through spatial analysis in this chapter. This chapter expands on work by O'Rourke et al. [3.2] by using the most recent and complete repair records, incorporating high resolution LiDAR measurements of lateral movements on 4-m spacing, applying refinements for

anisotropy in the geo-statistical interpolation of geometric mean peak ground velocity (GMPGV), and using the higher resolution data and improved screening criteria to provide better correlations among pipeline damage and liquefaction-induced lateral ground strains and differential vertical ground movements. The principal findings are:

- The Christchurch data for repair rate (RR) over GMPGV provide for more robust regressions for future fragility analyses of water distribution pipeline performance during earthquakes. The regressions in this study compare favorably with those previously reported by O'Rourke et al. [3.2].
- The regressions between RR and ground angular distortion,  $\beta$ , show a slightly lower level of damage for AC pipelines at relatively small  $\beta$  compared to the regressions reported by O'Rourke et al. [3.2] but otherwise for AC, CI, and PVC pipelines compare favorably with the previous work.
- The regressions between RR and lateral ground strain,  $\epsilon_{HP}$ , using the 4-m LiDAR measurement spacing are significantly different for AC and PVC pipelines than those previously reported for LiDAR measurements on 56-m spacing. The RR vs  $\epsilon_{HP}$  regressions for CI pipelines compare favorably because the pipelines were located in relatively uniform strain fields for which there is no significant difference between 4-m and 56-m resolution.
- The correlations among RR,  $\epsilon_{HP}$ , and  $\beta$  for AC and CI pipelines in this work are a significant improvement over those previously presented [3.2]. These

correlations for the first time provide the means to predict RR on the basis of the combined effects of lateral ground strain and differential vertical ground movement.

The regressions provided in this chapter quantify the relative performance of different types of pipelines under different levels of lateral ground strain and differential vertical ground movement. RRs vs  $\beta$  for AC pipelines plot approximately two times higher than those for CI pipelines, and 5 to 10 times higher than those for PVC pipelines. RRs vs  $\varepsilon_{HP}$  for AC pipelines are approximately 50% to 100% higher than those for CI pipelines, and approximately 3 to 11 times higher than those for PVC pipelines. The segmented pipelines most resilient to permanent and transient (PGD and TGD, respectively) ground deformation effects are PVC pipelines, for which substantial improvements in earthquake performance are quantified in this work with respect to AC and CI pipelines.

Scale effects have a substantial impact on the inferred relationship between pipeline damage and lateral ground strain, and depend on local variations in the strain field. High resolution data are needed to capture the influence of localized ground deformation. Computational modeling that utilizes regressions, such as those of RR vs  $\varepsilon_{HP}$ , need to account for scale effects, and should strive for the highest resolution possible at a scale equivalent to that of the structure being investigated.

Correlations among pipeline repair rates (RR), lateral ground strains, and differential vertical ground surface movements provide the means to predict pipeline damage on the basis of the combined effects of lateral ground strain and differential vertical ground movement. These correlations may be used in future planning, design, and loss estimation to assess limiting deformations for pipelines subjected to both PGD-induced lateral and vertical differential displacements.

This chapter provides flow charts with detailed steps in the geospatial analysis applied to LiDAR, transient ground motions, pipelines, and pipeline repair data sets. The flow charts document the methods used for analyzing the data for clarity of process and to assist in future investigations with data of similar size and complexity.

## REFERENCES

- [3.1] Elwood KJ, Comerio M, Cubrinovski M, Davis C, Johnston D, O'Rourke TD, Pampanin S. Special issue on the 2010-2011 CES. *Earthquake Spectra* 2014; **30**: p. 605.
- [3.2] O'Rourke TD, Jeon S-S, Toprak S, Cubrinovski M, Hughes M, van Ballegooy M, Bouziou D. Earthquake response of underground pipeline networks in Christchurch, NZ. *Earthquake Spectra* 2014; **30**(1):183-204.
- [3.3] Canterbury Earthquake Recovery Authority (CERA). Geotechnical database for Canterbury Earthquake Sequence, NZ, available at: <https://canterburygeotechnicaldatabase.projectorbit.com>. [accessed June 2012]
- [3.4] Geonet. Processed strong ground motions. Available at: <ftp://ftp.geonet.org.nz/strong/processed/Proc/2011/>. [accessed June 2013]
- [3.5] O'Rourke TD, Jeon S-S, Toprak S, Cubrinovski M, Jung JK. Underground lifeline system performance during the Canterbury Earthquake Sequence. *Proceedings of the 15th world conference on earthquake engineering*, 2012, Lisbon, Portugal.
- [3.6] Canterbury Geotechnical Database. Liquefaction interpreted from aerial photography, map layer CGD0200 - 11 Feb 2013. Available at: <https://canterburygeotechnicaldatabase.projectorbit.com/>. [accessed June 2012]
- [3.7] O'Rourke MJ, Liu X. *Response of buried pipelines subject to earthquake effects*. Monograph No.3: Multidisciplinary Center for Earthquake Engineering Research, Buffalo, NY, 1999.
- [3.8] Beavan J, Levick S, Lee J, Jones K. Ground displacements and dilatational strains caused by the 2010-2011 Canterbury earthquakes. *GNS Science Consultancy Report 2012/67*: GNS Science, 2012; p. 59.

- [3.9] Canterbury Geotechnical Database. Horizontal ground movements, map layer CGD0700 - 23 July 2012. Available at: <https://canterburygeotechnicaldatabase.projectorbit.com/>. [accessed June 2012]
- [3.10] Cubrinovski M, Hughes M, Bradley B, Noonan J, Hopkins R, McNeil S, English G. Performance of horizontal infrastructure in Christchurch city through the 2010-2011 Canterbury Earthquake Sequence. *Civil & Natural Resources Engineering Research Report 2014-02*: University of Canterbury, New Zealand, 2014.
- [3.11] Trautmann CH, O'Rourke TD, Grigoriu M, Khater MM. Systems model for water supply following earthquakes. *Lifeline Seismic Risk Analysis—Case Studies*, ASCE 1986; pp. 30-50.
- [3.12] Hwang MH, Huijie L, Shinozuka M. Seismic performance assessment of water delivery systems. *Journal of Infrastructure Systems*, ASCE 1998; **4**(3):118-125.
- [3.13] Jeon S-S, O'Rourke TD. Northridge earthquake effects on pipelines and residential buildings. *Bulletin of the Seismological Society of America* 2005; **95**(1): 294-318.
- [3.14] ArcMap 10.1. Environmental Systems Resource Institute (ESRI): Redlands, California, 2012.
- [3.15] Jeon S-S. *Earthquake performance of pipelines and residential buildings and rehabilitation with cast-in-place pipe lining systems*. Ph.D. Dissertation: Cornell University, Ithaca, NY, 2002.
- [3.16] Canterbury Geotechnical Database. LiDAR and digital elevation models, map layer CGD0500 - 23 July 2012, Available at: <https://canterburygeotechnicaldatabase.projectorbit.com/>. [accessed August 2012]
- [3.17] Burrough PA, McDonell RA. *Principles of geographical information systems*. Oxford University Press: New York, NY, 1998; p. 190.

- [3.18] Cook RD. *Finite element modeling for stress analysis*. John Wiley and Sons: New York, NY, 1995.
- [3.19] O'Rourke TD, Netravali AN, Pendharkar SM, Tonkinson A, Chaudhuri D, Toprak S. Evaluating service life of anaerobic joint sealing products and techniques. *Final Report*, No. GRI-96/0318: NASA, 1996.
- [3.20] Boscardin MD, Cording, EJ. Building response to excavation-induced settlement. *Journal of Geotechnical Engineering* 1989; **115**(1):1-21.
- [3.21] Manifold System Release 8. Manifold Software Limited: Wanchai, Hong Kong, 2013.
- [3.22] MATLAB and Statistics Toolbox Release 2012a. The MathWorks, Inc.: Natick, Massachusetts, US, 2012.

## CHAPTER 4

### A PROBABILISTIC APPROACH TO AXIAL PIPELINE STRAIN CAUSED BY PERMANENT GROUND DEFORMATIONS

#### **Abstract**

Underground pipelines, especially segmented pipelines, are vulnerable to earthquake-induced lateral, or horizontal, ground strains that cause pullout or compression at the pipeline joints. Although damage statistics, ground motion records, and ground deformation measurements from previous earthquakes have been used to correlate pipeline repair rates with ground strain, these methods do not account for the orientation of the pipeline within the ground strain field. A probabilistic approach is proposed in which the expected value of the ground strain in the axial direction of the pipeline is calculated by assuming that the probability of a given pipeline orientation relative to the direction of principal strain is uniformly distributed. High resolution Light Detection and Ranging (LiDAR) ground surface measurements acquired before and after the 22 February 2011 Christchurch earthquake in New Zealand are used to determine the expected value of ground strain caused by permanent ground deformations. Geocoded repair records for the Christchurch water distribution system are used to evaluate repair rates (RR), expressed as repairs/km, for different types of pipeline. These repair regressions have good statistical characteristics, and compare favorably with regressions developed previously between RR and the absolute value

of the maximum ground strain within the strain field. The relative vulnerability of different types of pipeline to tensile and compressive ground strain is explored, with little difference in the level of pipeline damage shown when the effects of both tension and compression are evaluated within a probabilistic context.

#### **4.1 Introduction**

Earthquake-induced lateral, or horizontal, ground strains affect underground pipelines, and especially segmented pipelines which are vulnerable to pullout or compression at the pipeline joints. Previous methods that use damage statistics from pipeline networks, ground motion records, and ground deformation measurements from previous earthquakes to correlate pipeline repair rates with ground deformation either do not account for the orientation of the pipeline within the ground strain field [4.1] [4.2], or provide only for an approximation of orientation [4.3]. A probabilistic approach is presented in this work to estimate earthquake-induced ground strains affecting segmented pipelines in the axial direction.

This chapter begins with a review of previous correlations between pipeline damage and various parameters for earthquake-induced deformation. Next, an expression for the expected value of the ground strain,  $\varepsilon_e$ , is derived by assuming that the probability of pipeline orientation relative to the direction of principal strain is uniformly distributed. The expression accounts for the potential difference between tension and compression on pipeline damage through the use of a weighting factor.

Water distribution repair records for the 22 February 2011 earthquake in Christchurch, NZ, are used to correlate repair rate (RR), in terms of repairs/km, for different types of pipelines with  $\varepsilon_e$ . Linear regressions between RR and  $\varepsilon_e$  are compared with the correlations between RR and maximum absolute ground strain,  $\varepsilon_{HP}$ , developed in Chapter 3. The linear regressions are further investigated for the potential effects of tensile and compressive ground strain by varying the weighting factor and comparing the various regressions for different pipeline types. Conclusions are drawn with respect to the use of  $\varepsilon_e$  and the choice of appropriate horizontal ground strain for estimating pipeline damage.

## **4.2 Background**

Pipeline repair regressions have been developed to relate pipeline damage caused by earthquakes with some measure of earthquake hazard intensity. Early correlations between repair rate (RR) and Modified Mercalli Intensity (MMI) were developed by Eguchi [4.4]. Other investigators studied the relationship between pipeline damage and transient ground deformation (TGD). For example, Katayama et al. [4.5] developed one of the first relations where RR was correlated with peak ground acceleration (PGA) as a metric for both TGD and permanent ground deformation (PGD) effects. Barenberg [4.6] developed empirical correlations between RR and peak horizontal ground velocity (PGV). This data set was later expanded by O'Rourke and Ayala [4.7] and used to develop more comprehensive regressions. Jeon and O'Rourke

[4.8] used worldwide data and data from the 1994 Northridge earthquake to explore correlations between RR and various seismic parameters, such as PGA, PGV, transient displacement, spectral acceleration and velocity, Arias Intensity, and Spectrum Intensity. They found that the most robust correlation was the one relating pipeline damage to PGV. Most recently, O'Rourke et al. [4.2] used ground motion data collected during the CES to expand on the correlations between RR and PGV developed by Jeon and O'Rourke [4.8].

Pipeline damage due to PGD effects was addressed by the American Lifelines Alliance (ALA) [4.9] through regressions between RR and permanent ground displacements that reflect landslide, settlement, fault offset, and liquefaction movements during previous earthquakes. As discussed by O'Rourke and Deyoe [4.1], this approach results in a considerable amount of scatter, which is reduced significantly when PGD effects are addressed with respect to ground strain as opposed to permanent ground deformation. O'Rourke and Deyoe [4.1], and O'Rourke [4.3] proposed RR relationships with both TGD- and PGD-induced ground strains. In these relationships, PGD-induced ground strains were derived from photogrammetric analyses of 1994 Northridge earthquake ground deformation by Sano et al. [4.10] as well as PGD data from Hamada and Akioka [4.11].

Using geocoded data collected during the Canterbury Earthquake Sequence (CES), O'Rourke et al. [4.2] developed RR regressions on the basis of 1) spatial distribution of peak ground velocity outside liquefaction areas, and 2) differential ground surface

vertical movement and lateral ground surface strain within areas affected by liquefaction. The combined effects of differential vertical ground movement and lateral ground strain were also addressed by O'Rourke et al. [4.2] with a damage assessment chart for asbestos cement (AC) and cast iron (CI) pipelines that allows for RR prediction as a function of differential vertical ground movement and lateral ground strain.

Differential lateral ground movements can be resolved into strains parallel to pipelines if the orientations of the pipelines and movements are known. O'Rourke et al. [4.12], for example, calculated ground strain by considering relative PGD along the axes of sewer and water transmission pipelines from the vectors of lateral ground movements during the 1999 Kocaeli earthquake, using pre- and post-earthquake aerial photogrammetric measurements.

Although ground movements can be resolved for specific pipelines with appropriate measurements, the resolution of either ground movement or ground strain for thousands of pipeline segments in a large geographically distributed network is subject to several limitations. The process, even when facilitated by Geographic Information Systems (GIS), results in computationally and time-wise expensive calculations and database manipulations. In addition, there may be considerable uncertainties with respect to segment orientation for very large numbers of pipeline segments resulting in collective error throughout an entire network.

To address the numerous orientations of pipelines in large networks, an expression for the expected value of strain,  $\epsilon_e$ , is developed in the following section that provides an estimate of ground strain in the axial direction of any pipeline segment. This probabilistically based approach takes into consideration pipeline orientation within the ground strain field.

### 4.3 Axial Ground Strain Affected by Pipeline Orientation

It is often assumed that segmented pipelines consist of joints with lower resistance against pullout when affected by tensile strains than compression when affected by compressive ground strains. To account for the difference in resistance to both tension and compression in RR correlations, RR was related to ground strain,  $\epsilon$ , by including a weighting factor,  $k$ , as

$$RR = a + k\epsilon \quad (4.1)$$

for which  $k = 1.0$  when  $\epsilon \geq 0$ , and  $k \leq 1.0$  when  $\epsilon < 0$ , given that tensile ground strain corresponds to  $\epsilon \geq 0$ . In this way, a lower level of damage can be potentially attributed to compressive ground strains relative to tensile ones.

Consider a pipeline as shown in Figure 4.1a oriented with respect to the principal directions of strain,  $\epsilon_1$ , at  $\theta$ . At any  $\theta$  the net strain,  $\epsilon$ , in the ground parallel to the pipeline is

$$\varepsilon = \varepsilon_1 \cos\theta + \varepsilon_2 \sin\theta \quad (4.2)$$

It is assumed that the axial pipeline strain will be related directly to  $\varepsilon$  and that compression and pullout at the joints of a segmented pipeline will be affected by the pipeline axial strain. It is assumed that the pipeline has an equal chance of being oriented at any  $\theta$  for orientations of the pipeline that vary from 0 to  $\pi$ . The probability density function for  $\theta$  is shown in Figure 4.1b and is

$$f(\theta) = \begin{cases} \frac{1}{\pi}, & \text{for } 0 \leq \theta \leq \pi \\ 0, & \text{otherwise} \end{cases} \quad (4.3)$$

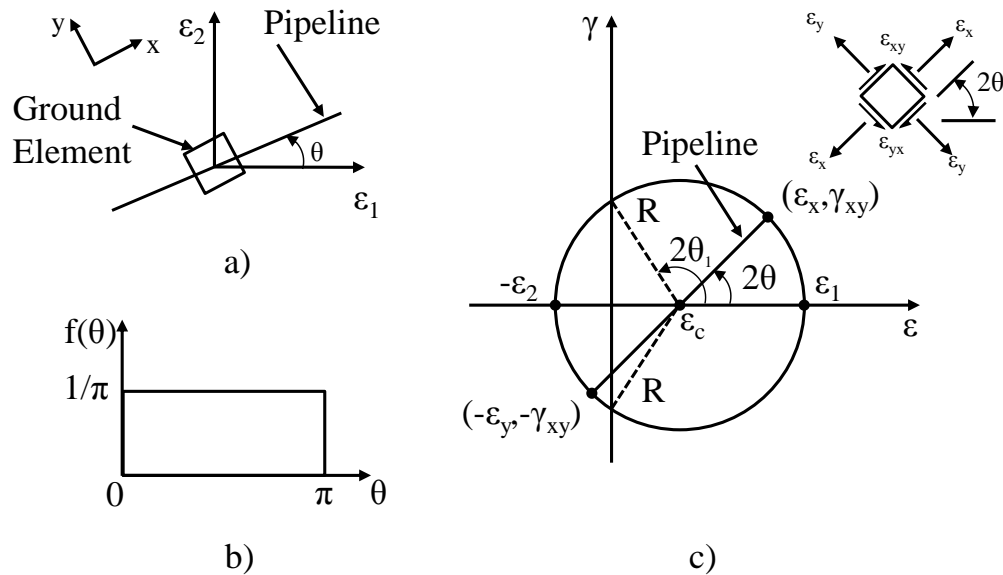


Figure 4.1. a) Pipeline orientation relative to principal strain directions. b) Probability density function of pipeline orientation,  $\theta$ . c) Mohr circle of strains for tensile,  $\varepsilon_1$ , and compressive,  $\varepsilon_2$ , strains.

The weighted average, or mean, strain affecting the pipeline is provided by combining Equations 4.2 and 4.3 and recognizing that the combinations of net strains from 0 to  $\pi$  are twice the combinations of net strains from 0 to  $\pi/2$ . The mean strain,  $\epsilon_m$ , is, thus, determined as

$$\epsilon_m = \frac{2}{\pi} \int_0^{\pi/2} (\epsilon_1 \cos \theta + \epsilon_2 \sin \theta) d\theta \quad (4.4)$$

and

$$\epsilon_m = \frac{2}{\pi} (\epsilon_1 + \epsilon_2); \quad \epsilon_2 \geq 0 \quad (4.5)$$

which applies when the principal strains are both in tension.

When the principal strains are both in compression and a weighting factor,  $k$ , is applied, the weighted value of the mean strain, or expected value of strain,  $\epsilon_e$ , is

$$\epsilon_e = \frac{2k|\epsilon_1 + \epsilon_2|}{\pi}; \quad \epsilon_1 \leq 0 \quad (4.6)$$

in which  $|\epsilon_1 + \epsilon_2|$  is the absolute value of the sum of the two negative compressive strains.

When tensile and compressive ground strains are present, the Mohr circle of strains is shown in Figure 4.1c. For this condition, the net ground strain at any  $\theta$  is

$$\varepsilon = \varepsilon_1 \cos \theta - \varepsilon_2 \sin \theta \quad (4.7)$$

The angle,  $\theta_1$ , at which the net strain,  $\varepsilon$ , is zero is given by

$$\varepsilon_1 \cos \theta = \varepsilon_2 \sin \theta \quad (4.8)$$

from which

$$\theta_1 = \tan^{-1} \left( \frac{\varepsilon_1}{\varepsilon_2} \right) \quad (4.9)$$

Taking  $k$  into account, the expected value of ground strain influencing the pipeline performance,  $\varepsilon_e$ , is

$$\varepsilon_e = \frac{2}{\pi} \int_0^{\theta_1} (\varepsilon_1 \cos \theta - \varepsilon_2 \sin \theta) d\theta - \frac{2k}{\pi} \int_{\theta_1}^{\pi/2} (\varepsilon_1 \cos \theta - \varepsilon_2 \sin \theta) d\theta \quad (4.10)$$

in which the integral from 0 to  $\theta_1$ , accounts for net tensile strains, and the integral from  $\theta_1$  to  $\pi/2$  accounts for net compressive strains.

Integration of Equation 4.10 results in

$$\varepsilon_e = \frac{2}{\pi} [(1+k)(\varepsilon_1 \sin \theta_1 + \varepsilon_2 \cos \theta_1) - (k\varepsilon_1 + \varepsilon_2)] \quad (4.11)$$

Recognizing that  $\varepsilon_2 = \varepsilon_1 \cot \theta_1$  and substituting this expression into Equation 4.11, results in

$$\varepsilon_e = \frac{2\varepsilon_1}{\pi} [(1+k)(\sin \theta_1 + \cot \theta_1 \cos \theta_1) - (k + \cot \theta_1)] \quad (4.12)$$

Normalizing Equation 4.12 with respect to  $(\varepsilon_1 - \varepsilon_2)$ , the diameter of the Mohr circle of strains, gives

$$\frac{\varepsilon_e}{\varepsilon_1 - \varepsilon_2} = \frac{2}{\pi(1 + \cot \theta_1)} [(1+k)(\sin \theta_1 + \cot \theta_1 \cos \theta_1) - (k + \cot \theta_1)] \quad (4.13)$$

where  $\varepsilon_2$  in Equation 4.13 is  $-\varepsilon_2$  in the Mohr circle of strain shown in Figure 4.1c so that  $(\varepsilon_1 - \varepsilon_2) = (\varepsilon_1 + \varepsilon_2) = (1 + \cot \theta_1)$ .

Equation 4.13 is plotted in Figure 4.2 for various  $k$ . As the Mohr circle of strain migrates from right to left in Figure 4.1c, the value of  $\varepsilon_1$  decreases from a value equal to the Mohr circle diameter at  $\theta_1 = \pi/2$  to 0 at  $\theta_1 = 0$ . The value of  $\theta_1$  defines the ratio of  $\varepsilon_1/\varepsilon_2 = \tan \theta_1$ . The horizontal axis in Figure 4.2, therefore, represents all the different combinations of  $\varepsilon_1$  and  $\varepsilon_2$  when the principal ground strains are both tensile and compressive. For  $k=1.0$ , Equation 4.13 plots symmetrically on either side of  $\theta_1 = 45^\circ$ , indicating that tensile and compressive strains have the same effect in the expression for expected value of ground strain in the axial direction of the pipeline. For  $k < 1.0$ , Equation 4.13 plots higher for  $\theta_1 > 45^\circ$  than for  $\theta_1 < 45^\circ$  due to smaller effect of compressive strains on pipelines than tensile strains.

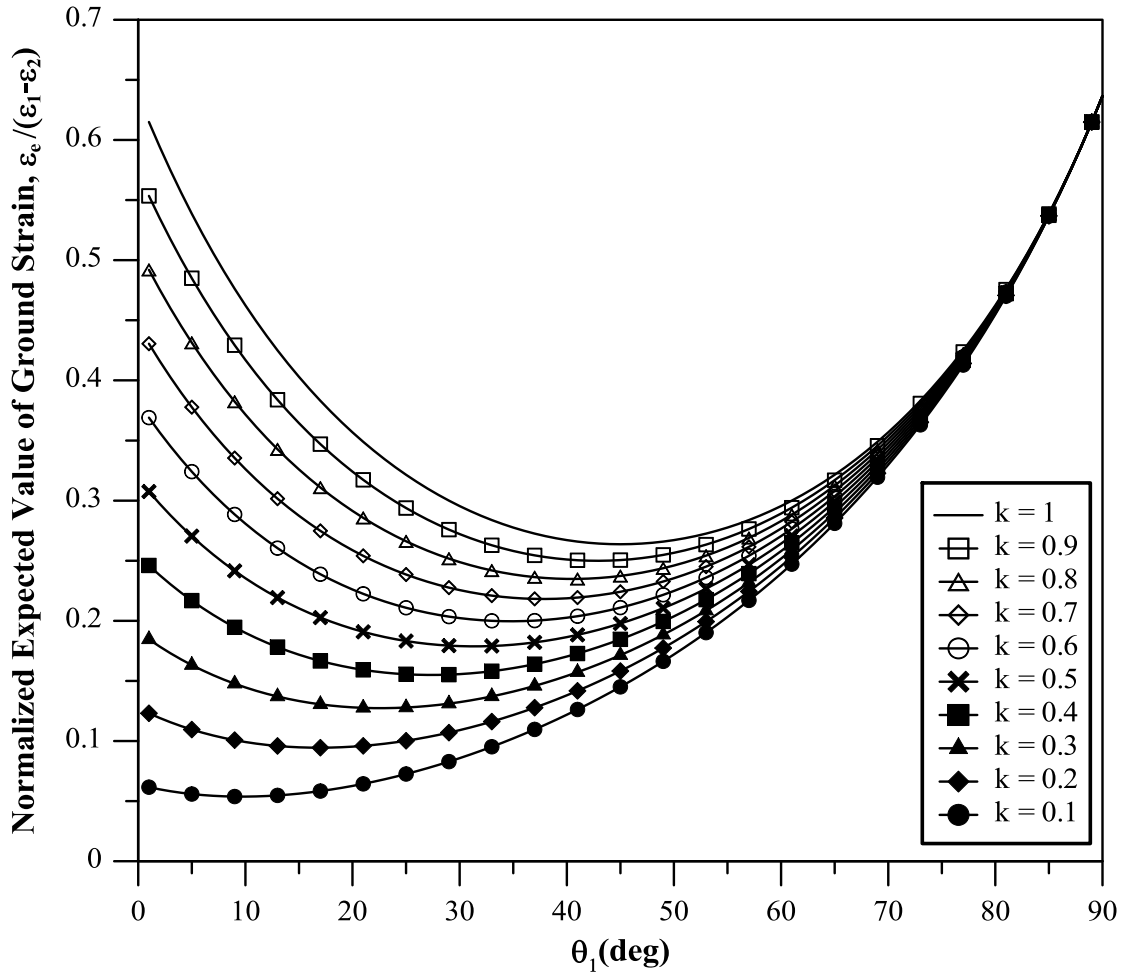


Figure 4.2. Normalized expected value of ground strain as a function of  $\theta_1$ .

#### 4.4 Geospatial Data for the 22 February 2011 Christchurch Earthquake

Zones of liquefaction were interpreted from aerial photography as well as surface observations and mapping for the 22 February 2011 earthquake in Christchurch, New Zealand. Observed liquefaction effects include sand ejecta, as well as ground cracking, lateral spreading and differential surface settlement. The areas of documented liquefaction were obtained through the Canterbury Geotechnical Database [4.13].

These zones were expanded to account for the effects of liquefaction on buried pipelines not visible by surface observations. The dimension used to estimate the zone of influence was taken as 125 m, which is approximately one-half a typical street length in a residential neighborhood and is consistent with the distance that significant pullout forces can be transmitted longitudinally along underground pipelines [4.14]. The resulting area of liquefaction effects on pipelines, covering approximately 96 km<sup>2</sup> within Christchurch area shown in Figure 4.3, involves approximately 952 km of water distribution pipelines and approximately 1290 repairs in the water distribution network, as discussed in Chapter 3.

The water distribution system under study consists of approximately 1700 km of water mains and trunk lines. Spatial data of the water distribution system were developed by the Christchurch City Council (CCC) and the Stronger Christchurch Infrastructure Rebuild Team (SCIRT) and provide the most complete picture of the system as of 4 Sept. 2010 [4.15]. The data sets include information about the type, diameter, material, length, and year of installation for each individual pipe in the network. The water distribution system under study includes water mains and trunk lines with diameters between 75 and 600 mm, conveying the largest flows in the system. It does not include repairs to smaller diameter submains and customer service laterals. Water distribution pipelines located within areas affected by liquefaction during the 22 Feb. 2011 earthquake are used in this study to develop repair regressions with lateral ground strains caused by PGD for the three most common pipeline types

found in the Christchurch water distribution system; AC (~50%), CI (~11%), and polyvinyl chloride (PVC) (~12%) pipelines. Figure 4.3 shows the distribution of AC, CI, and PVC water mains within the areas affected by liquefaction during the 22 Feb. 2011 earthquake.

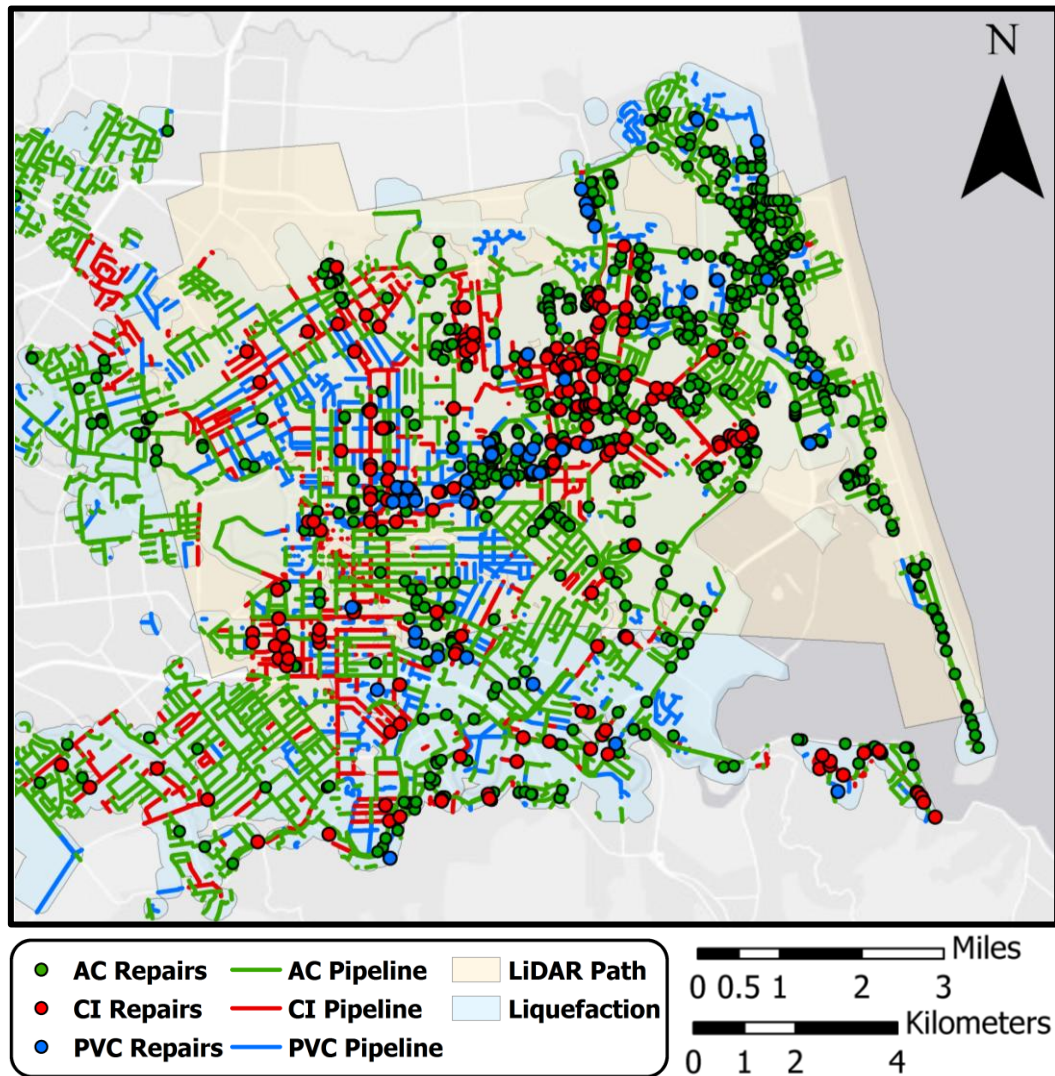


Figure 4.3. Repairs to AC, CI, and PVC pipelines within the areas affected by liquefaction during the 22 February 2011 earthquake and LiDAR area covering Christchurch.

The water repair database provided by SCIRT and used in this study includes information about the continuous daily repair records for re-establishment of services between the period from February 23, 2011 to March 11, 2013. As discussed in Chapter 3, O'Rourke et al. [4.2] studied the cumulative frequency of repairs in the water distribution system during the CES and determined the end of repair activities directly related to each main seismic event. Similar to the study by O'Rourke et al. [4.2], repair records for AC, CI, and PVC water pipelines located in the areas of liquefaction effects, and dating from February 23, 2011 to April 15, 2011, were related to PGD effects during the 22 Feb. 2011 earthquake and used in this study. Figure 4.3 shows the distribution of AC, CI, and PVC pipeline repairs within the areas of liquefaction effects during the 22 Feb. 2011 earthquake.

Airborne Light Detection and Ranging (LiDAR) data were collected before and after the 22 February 2011 earthquake, and were used by GNS Science under contract with Tonkin & Taylor Ltd (T&T), Christchurch, New Zealand, to determine horizontal and vertical ground movements developed during the 22 Feb. 2011. A dislocation model of lateral tectonic movement for the 22 Feb. 2011 available through GNS Science [4.16] was applied to the LiDAR data set of lateral ground surface movement to correct lateral ground measurements for tectonic movement. LiDAR lateral movements were originally calculated at 4-m and 8-m spacing, and were averaged to provide lateral movements at 56 m spacing. Lateral ground movements at 4-m spacing pertaining to the 22 Feb. 2011 earthquake were used to calculate lateral ground strain

in areas affected by PGD and develop repair regressions discussed in this work. Figure 4.3 shows the LiDAR area of lateral ground movements. Lateral ground strains caused by PGD were calculated in the areas intersected both by the areas of liquefaction effects and the LiDAR area shown in Figure 4.3.

#### **4.5 Regression Analysis with Expected Value of Ground Strain**

Lateral ground strains were calculated using LiDAR lateral ground movements at 4-m spacing, and assuming plane strain conditions for quadrilateral elements. Finite element formulations were used to determine horizontal ground strains according to the method described by Cook [4.17] using LiDAR lateral movements that were provided in the east-west (EW) and north- south (NS) directions. The calculation process for lateral ground strains using LiDAR lateral ground measurements has been described in detail in Chapter 3.

Using the principal ground strains from the LiDAR measurements for each elemental area of ground, the expected value of ground strain,  $\epsilon_e$ , was determined from Equations 4.9 and 4.13 when both tensile and compressive ground strains are present. When the strain field involves all tensile or all compressive ground strains, Equations 4.5 and 4.6, respectively, are used to calculate  $\epsilon_e$ , recognizing that  $\epsilon_m = \epsilon_e$  in Equation 4.5.

The screening criteria proposed by O'Rourke et al. [4.2] and discussed in Chapter 3 were used in the regression analysis in this study to ensure that pipeline intervals of sufficient length were chosen. Similar to repair rate (RR) correlations with the absolute maximum lateral ground strain,  $\epsilon_{HP}$ , pipelines and repairs inside the areas of liquefaction influence and excluding those above 50 m in elevation subject to landslides in the Port Hills were used for RR correlations with  $\epsilon_e$ . RR for a given interval of  $\epsilon_e$  was calculated similar to RRs for  $\epsilon_{HP}$ , by dividing the number of repairs for a particular type of pipeline by the kilometers of that pipeline type within the same interval. The interval size and confidence level for  $\epsilon_e$  was similar to the interval size for  $\epsilon_{HP}$  to provide direct comparison among repair regressions with different lateral ground strain metrics. Hence, interval size was adjusted to 0.2% for AC and PVC pipelines, and 0.05% for CI. Similarly, the confidence level,  $\beta_c$ , during the screening process was adjusted to 95%, 85%, and 75% for AC, CI, and PVC pipelines, respectively. Four different values for k were considered in the calculation of  $\epsilon_e$  ranging from 0.25 to 1.0 at 0.25 intervals to evaluate the sensitivity of the RR vs  $\epsilon_e$  regressions to the difference in response to tension and compression. As previously discussed, a weighting factor  $k=1.0$  reflects no difference in pipeline joint response to tensile and compressive ground strains, whereas  $k<1.0$  represents greater resistance to compression than tension.

The results for RR vs  $\epsilon_e$  with  $k=1.0$  and RR vs  $\epsilon_{HP}$  for AC, CI, and PVC pipelines are presented in Figure 4.4a through Figure 4.4c. Comparison among linear

regressions of RR vs  $\epsilon_e$  with  $k = 1.0$  for AC, CI, and PVC pipelines is presented in Figure 4.4d and shows that RR vs  $\epsilon_e$  for AC pipelines plots 1.3 to 1.7 times higher than RR vs  $\epsilon_e$  for CI pipelines, and 2 to 12 times higher than PVC pipelines.

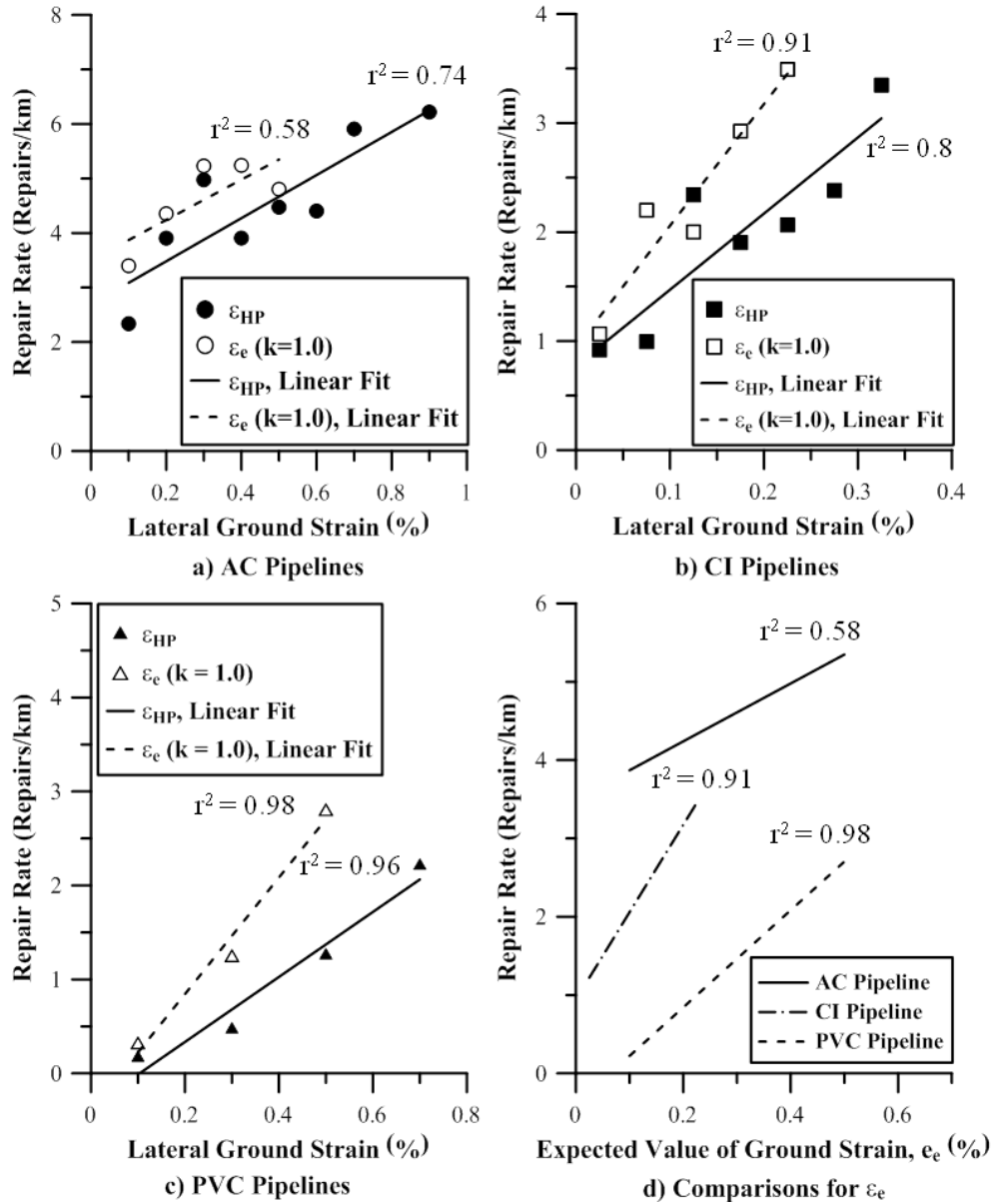


Figure 4.4. RR regressions with expected value for ground strain,  $\epsilon_e$ , with  $k=1.0$  and absolute maximum ground strain for a) AC, b) CI, and c) PVC pipelines, and d) comparison of RR vs  $\epsilon_e$  with  $k = 1.0$  for the three pipeline types.

Using  $\varepsilon_e$  results in low values of ground strain relative to  $\varepsilon_{HP}$  for equivalent RR. The linear regressions for  $\varepsilon_e$ , therefore, plot above those for  $\varepsilon_{HP}$  in all cases. The reduced levels of  $\varepsilon_e$  relative to  $\varepsilon_{HP}$  result in regressions that are constrained to a lower range of strain. The linear regressions for  $\varepsilon_e$  and  $\varepsilon_{HP}$  are similar with respect to  $r^2$  and distribution of residuals. The use of  $\varepsilon_e$  is therefore comparable to  $\varepsilon_{HP}$  as a metric for correlations with RR. The use of  $\varepsilon_{HP}$ , however, has the advantage of being a more straightforward approach with less computational demands.

RR vs  $\varepsilon_e$  for weighting factors,  $k = 1.0, 0.75, 0.5,$  and  $0.25$  are presented in Figure 4.5a and Figure 4.5b for AC and CI pipelines, respectively. There are insufficient data for PVC pipelines for a comparative analysis of the regressions for different  $k$  values. With respect to AC pipelines, the highest  $r^2$  values are for  $k = 1.0$  and  $k = 0.75$ , with a notable reduction in  $r^2$  associated with  $k = 0.5$  and  $k = 0.25$ . For CI pipelines, the highest  $r^2$  is associated with  $k = 1.0$ . Overall, there is little evidence on the basis of the regressions for a reduction in the level of damage because of compression. When evaluated in terms of  $\varepsilon_e$ , the AC and CI pipelines appear to be equally affected by tensile and compressive ground strains.

#### **4.6 Combined Effects of Expected Value of Lateral Ground Strain and Differential Vertical Ground Movement**

Repair rates were correlated with  $\varepsilon_e$  and angular distortion,  $\beta$ , using the procedures described in Chapter 3. For a comprehensive approach to evaluate pipeline damage,

one must account simultaneously for lateral ground strain and differential vertical movements. As described in Chapter 3, the dimensionless parameter,  $\beta$ , is determined as

$$\beta = \frac{\delta z_1 - \delta z_2}{l_{12}} \tag{4.14}$$

where  $\delta z_1$  and  $\delta z_2$  are vertical movements of points 1 and 2, respectively, and  $l_{12}$  is the distance between them.

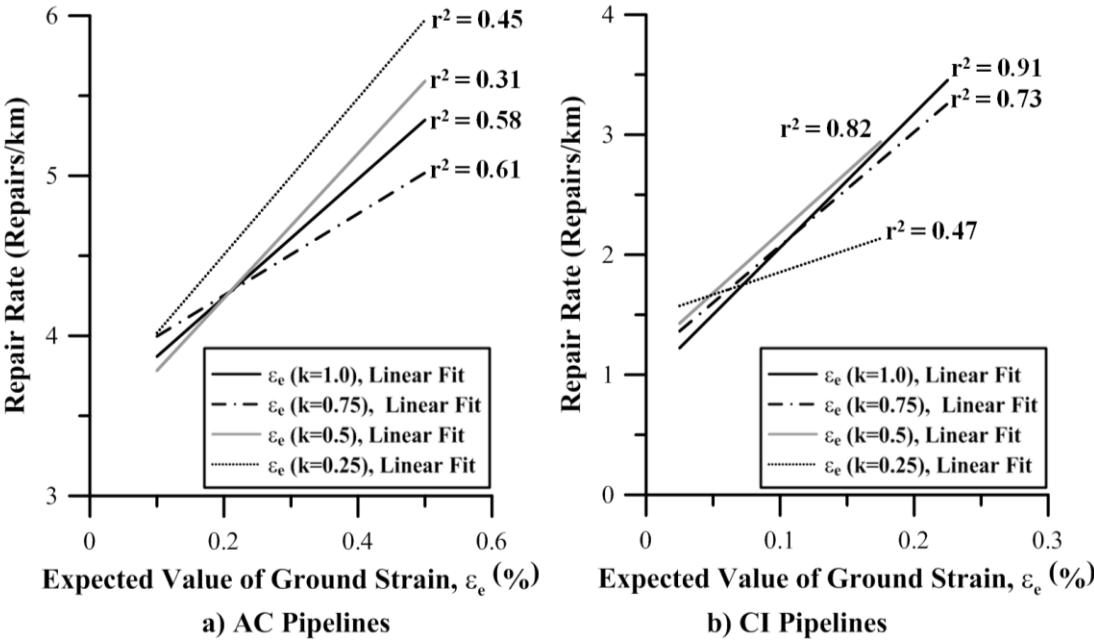


Figure 4.5. RR regressions with expected value for ground strain considering four different values for  $k$  ( $k=1.0$ ,  $k=0.75$ ,  $k=0.5$ ,  $k=0.25$ ) for a) AC and b) CI pipelines.

Angular distortion was calculated from high resolution LiDAR data on 5-m spacing by computing the differences in the LiDAR digital elevation models before and after the 22 February 2011 Christchurch earthquake [4.18]. Using the same

approach described in Chapter 3 for  $\epsilon_e$ , pipelines and repairs were spatially intersected with  $\beta$  and  $\epsilon_e$ , and RR was calculated for a given pair of intervals of  $\beta$  and  $\epsilon_e$  by dividing the number of repairs for a particular type of pipeline by the kilometers of that pipeline within the same pair of intervals. The interval for  $\beta$  was  $10^{-3}$ , and for  $\epsilon_e$  was 0.2%. The RRs were associated with appropriate pair of  $\beta$  and  $\epsilon_e$  and were used as data points for RR correlations. The screening criteria described in Chapter 3 were applied for each set of data points and the confidence interval was adjusted to 75% and 60% for AC and CI pipelines, respectively, to develop reasonably dense distribution of data across the largest  $\beta$  vs  $\epsilon_e$  space. The global polynomial interpolation method in ArcMap 10.1 [4.19] was used to fit a smooth surface of RR contours as illustrated in Figure 4.6. A first order polynomial was applied to the data.

The contours for RR vs  $\beta$  and  $\epsilon_e$  are presented in Figure 4.6a and Figure 4.6b, where they are compared with the contours for RR vs  $\beta$  and  $\epsilon_{HP}$  in Figure 4.6c and Figure 4.6d. Figure 4.6a and Figure 4.6c are for AC pipelines, and Figure 4.6b and Figure 4.6d are for CI pipelines. The contours of RR vs  $\beta$  and  $\epsilon_e$  are similar to those of RR with respect to  $\beta$  and  $\epsilon_{HP}$  for both AC and CI pipelines. Developing RR contours for  $\epsilon_e$  involves a strain parameter that is lower than  $\epsilon_{HP}$  for all RRs. One result of using the lower magnitude  $\epsilon_e$  is that less data points are available to develop the multiple regression contours. The lower value  $\epsilon_e$  regressions result in a lower density of RR contour lines. Although  $\epsilon_e$  accounts for pipeline orientation more rigorously than  $\epsilon_{HP}$ ,

its lower value leads to a reduction in granularity and geographic detail when estimating spatially distributed pipeline damage.

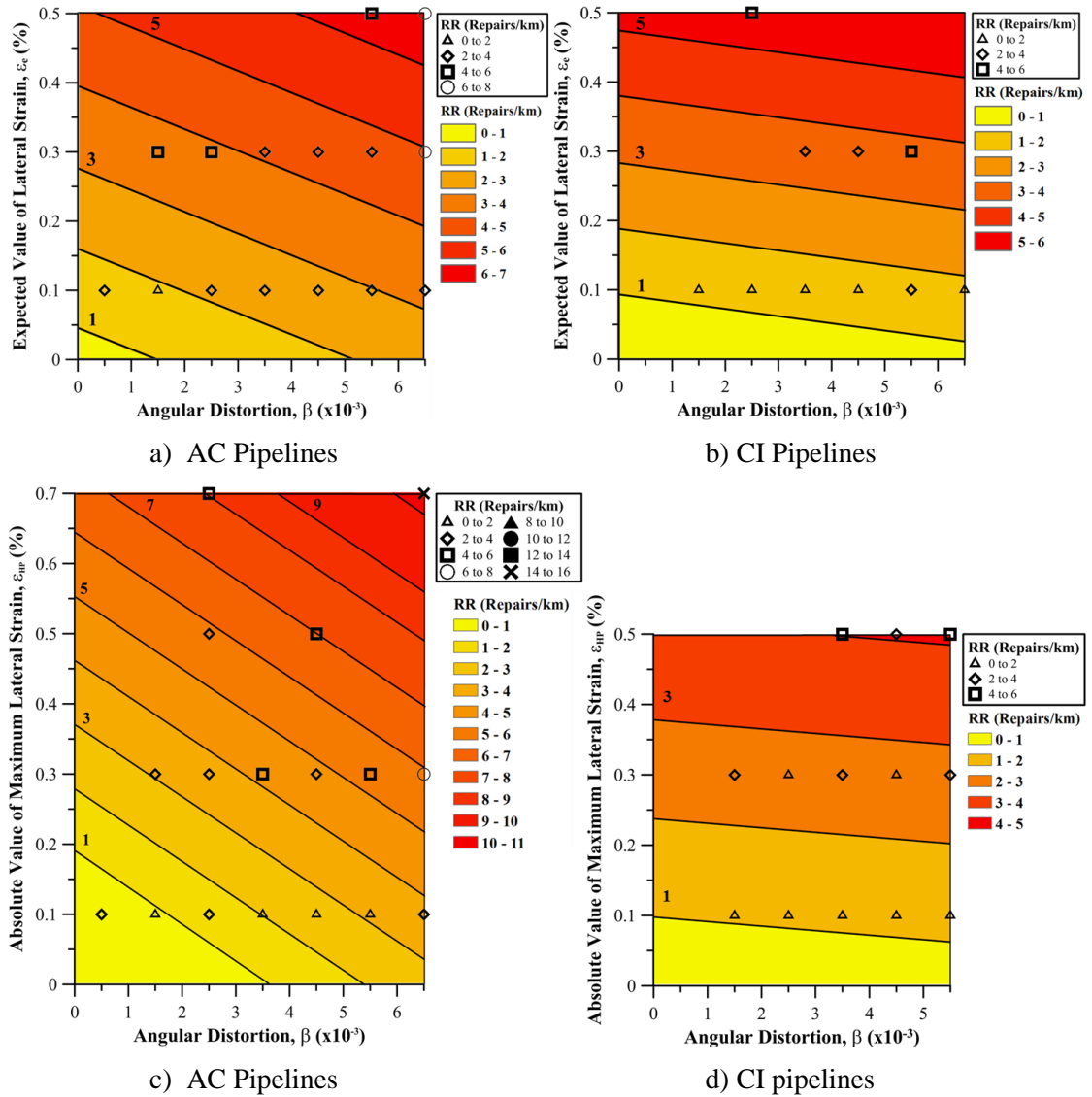


Figure 4.6. Repair rate vs expected value of lateral strain and angular distortion for a) AC and b) CI pipelines, and repair rate vs absolute maximum value of lateral strain and angular distortion for c) AC and d) CI pipelines.

## 4.7 Conclusions

In Chapter 3 pipeline damage was related to the absolute maximum value of ground strain,  $\varepsilon_{HP}$ , as a unique indicator of horizontal ground distortion. Although statistically sound regressions were developed between repair rate (RR) and  $\varepsilon_{HP}$ , it is recognized that  $\varepsilon_{HP}$  does not account for pipeline orientation within the strain field. To account for pipeline orientation, a rigorous derivation is presented for the expected value of ground strain in the axial direction of the pipeline,  $\varepsilon_e$ . The use of  $\varepsilon_e$  provides an alternative probabilistic parameter for ground strain effects, which accounts for pipeline orientation, as well as the relative effects of tension and compression through the use of a weighting factor,  $k$ .

Geocoded water distribution system repair records and Light Detection and Ranging (LiDAR) ground movement measurements for the 22 February 2011 earthquake in Christchurch, New Zealand, were used to correlate RR, expressed as repairs/km, for different types of pipeline with  $\varepsilon_e$  for various  $k$  with the following findings:

- When compared with  $\varepsilon_{HP}$ ,  $\varepsilon_e$  provides a parameter that results in RR regressions with similar  $r^2$  and distribution of residuals. There is no apparent advantage of  $\varepsilon_e$  with respect  $\varepsilon_{HP}$  for the Christchurch database. The use of  $\varepsilon_{HP}$  is more straightforward and results in less computational demands.

- A comparative assessment of RR vs  $\epsilon_e$  regressions for different weighting factors,  $k$ , shows that AC and CI pipeline damage is equally affected by tensile and compressive ground strains.
- Correlations of RR with respect to  $\epsilon_e$  and angular distortion,  $\beta$ , result in relationships that are similar to those developed for  $\epsilon_{HP}$  and  $\beta$ . Because  $\epsilon_e$  is lower in value than  $\epsilon_{HP}$  for all RRs, the relationships among RR,  $\beta$ , and  $\epsilon_e$  are developed from fewer data points than their  $\epsilon_{HP}$  counterparts, with the result that there is less range and variation in  $\epsilon_e$  and RR for comparable values of  $\beta$ .

Because the expected value of ground strain accounts for pipeline orientation in a probabilistic way, it has intrinsic value as an estimator of pipeline damage. Even though  $\epsilon_e$  does not show clear advantages over  $\epsilon_{HP}$  on the basis of the Christchurch data, its value may be realized in the future for complex pipeline network analyses.

For the level of uncertainty associated with the lateral LiDAR measurements used in this study, it is not possible to distinguish AC and CI pipeline vulnerability as being more or less sensitive to tensile vs compressive ground strains. The equivalent vulnerability of AC and CI pipelines to both tensile and compressive ground strains, when averaged over an entire network, helps explain why the maximum absolute ground strain,  $\epsilon_{HP}$ , is an effective metric for pipeline seismic damage regressions. Because  $\epsilon_{HP}$  is an unbiased indicator with respect to tension and compression, it is not sensitive to either tension or compression, and, thus, it is consistent with the

equivalent vulnerability of segmental pipelines to tensile and compressive ground strains. The absolute value of maximum ground strain,  $\varepsilon_{HP}$ , is well suited for repair correlations when pipelines have equivalent vulnerability to tensile and compressive ground strains, and such correlations have similar statistical properties to correlations of pipeline damage with the expected value of ground strain.

## REFERENCES

- [4.1] O'Rourke MJ, Deyoe E. Seismic damage to segmented buried pipe. *Earthquake Spectra* 2004; **20**(4):1167-1183.
- [4.2] O'Rourke TD, Jeon S-S, Toprak S, Cubrinovski M, Hughes M, van Ballegooy S, Bouziou D. Earthquake response of underground pipeline networks in Christchurch, NZ. *Earthquake Spectra* 2014; **30**(1):183-204.
- [4.3] O'Rourke MJ. Analytical fragility relations for buried segmented pipe. *Proceedings of 2009 TCLEE Conference, Lifeline Earthquake Engineering in a Multihazard Environment, ASCE*, 2009, Oakland, California.
- [4.4] Eguchi RT. Seismic vulnerability models for underground pipes. *Earthquake behavior and safety of oil and gas storage facilities, buried pipelines and equipment*, PVP-77: ASME, New York, NY, 1983.
- [4.5] Katayama T, Kubo K, Sato N. Earthquake damage to water and gas distribution systems, *Proceedings of U.S. National Conference on Earthquake Engineering*, 1975, Oakland, California.
- [4.6] Barenberg ME. Correlation of pipeline damage with ground motions. *Journal of Geotechnical Engineering, ASCE* 1988; **114**(6):706-711.
- [4.7] O'Rourke MJ, Ayala, G. Pipeline damage due to wave propagation. *Journal of Geotechnical Engineering, ASCE* 1993; **119**(9):1490-1498.
- [4.8] Jeon S-S, O'Rourke TD. Northridge earthquake effects on pipelines and residential buildings. *Bulletin of the Seismological Society of America* 2005, **95**(1):294-318.
- [4.9] Eidinger JM, Avila EA, Ballantyne DB, Cheng L, Der Kiureghian A, Maison BF, O'Rourke TD, Power MS. Seismic fragility formulations for water systems, *Part I: Guideline*. American Lifelines Alliance, 2001.

- [4.10] Sano Y, O'Rourke TD, Hamada M. GIS evaluation of Northridge earthquake ground deformation and water supply damage. *Proceedings of the 5<sup>th</sup> U.S. Conference on Lifeline Earthquake Engineering*, 1999, Seattle, WA; pp. 832–839.
- [4.11] Hamada M, Akioka Y. Liquefaction induced ground strain and damage to buried pipes. *Proceedings of Japan Society of Civil Engineers Earthquake Engineering Symposium*, 1997, Kobe, Japan; 1:1353–1356 (in Japanese).
- [4.12] O'Rourke M, Filipov E, Uçkan E. Towards robust fragility relations for buried segmented pipe in ground strain areas. *Earthquake Spectra* 2014 In-Press, available at <http://dx.doi.org/10.1193/032311EQS076M>.
- [4.13] Canterbury Earthquake Recovery Authority (CERA). Geotechnical database for Canterbury Earthquake Sequence, NZ0, available at: <https://canterburygeotechnicaldatabase.projectorbit.com>. [accessed June 2012]
- [4.14] O'Rourke MJ, Liu X. *Response of buried pipelines subject to earthquake effects*. Monograph No.3: Multidisciplinary Center for Earthquake Engineering Research, Buffalo, NY, 1999.
- [4.15] Cubrinovski M, Hughes M, Bradley B, Noonan J, Hopkins R, McNeil S, English G. Performance of horizontal infrastructure in Christchurch city through the 2010-2011 Canterbury Earthquake Sequence. *Civil & Natural Resources Engineering Research Report 2014-02*: University of Canterbury, New Zealand, 2014.
- [4.16] Geonet. Processed strong ground motions. Available at: <http://www.geonet.org.nz/>. [accessed June 2013]
- [4.17] Cook RD. *Finite element modeling for stress analysis*. John Wiley and Sons: New York, 1995.
- [4.18] Canterbury Geotechnical Database. LiDAR and digital elevation models, map layer CGD0500 - 23 July 2012, available at:

<https://canterburygeotechnicaldatabase.projectorbit.com>. [accessed August 2012]

[4.19] ArcMap 10.1. Environmental Systems Resource Institute (ESRI): Redlands, California, 2012.

## CHAPTER 5

### EVALUATION OF GROUND DEFORMATIONS DURING THE 2010-2011 CANTERBURY EARTHQUAKE SEQUENCE

#### **Abstract**

This chapter presents a statistical analysis of ground deformations caused by liquefaction during the 2010-2011 Canterbury Earthquake Sequence (CES) in New Zealand. Liquefaction-induced differential vertical ground movements and lateral ground strains are calculated from high resolution light detection and ranging (LiDAR) data collected before and after each of the main earthquakes. A special study area is selected to perform statistical evaluations by eliminating areas that contribute to LiDAR error. The locations of highest ground deformation, expressed as differential vertical ground movement and lateral ground strain, are identified throughout Christchurch based on the statistical distributions and are evaluated with respect to various landforms and waterways in the Christchurch alluvial plain. The highest values of differential vertical ground movement align themselves clearly with water courses in Christchurch and provide a remarkably accurate measure for locating all sizes and types of natural water courses. The highest lateral ground strains align themselves at locations adjacent to the Avon River and tend to cluster in locations covered by vegetation, reflecting the contribution of vegetation to LiDAR horizontal measurement errors. Statistical analyses of LiDAR-based differential vertical ground

displacements, lateral ground strains, and lateral and vertical ground movements are performed in the special study area for the 4 Sept. 2010, 22 Feb. 2011, and 13 June 2011 earthquakes. The data are well described by the generalized extreme value distribution and overall indicate that the 4 Sept. 2010 earthquake was accompanied by the most severe liquefaction-induced ground deformation on a local basis, whereas the 22 Feb. 2011 earthquake was accompanied by the most extensive liquefaction-induced ground deformation and damage to underground infrastructure.

Data from detailed damage surveys of 12 residential properties in Christchurch are used to evaluate foundation damage, expressed as lateral strain at concrete perimeter footings and differential vertical ground floor displacement, with respect to liquefaction-induced lateral ground strain and angular distortion, respectively. The correlations between foundation damage and ground deformation depend on data that are too sparse to show clear, definitive trends. They nonetheless are in broad agreement, indicating that LiDAR-based ground deformations may provide a productive method for predicting building damage when evaluated with respect to a larger and geographically more extensive database.

## **5.1 Introduction**

The Canterbury Earthquake Sequence (CES) in New Zealand involved four main earthquake events ( $M_w$  7.1, 4 Sept. 2010;  $M_w$  6.2, 22 Feb. 2011;  $M_w$  6.0, 13 June 2011;  $M_w$  5.9, 23 Dec. 2011), and multiple events of lesser magnitude, including

approximately 60 over  $M_w$  5.0, that caused high levels of transient and permanent ground deformations (TGD and PGD, respectively). Substantial damage to buildings and infrastructure occurred in areas affected by liquefaction due to PGD, and most notably during the 22 Feb. 2011 earthquake [5.1]. Vertical and horizontal differential ground movements resulting from liquefaction ejecta, ground subsidence and lateral spreading caused damage to approximately 20,000 houses in the Christchurch area [5.2].

This chapter presents a statistical analysis of high resolution airborne light detection and ranging (LiDAR) data for vertical and lateral ground surface movements collected before and after each main event. A description of the LiDAR data sets is provided. A special study area is selected for a systematic analysis of LiDAR-based ground deformation, which includes a large part of Christchurch within the catchment area of the Avon River. Using the study area, ground movement patterns are analyzed by developing statistical distributions of ground deformation to identify exceedance values for differential vertical ground movement and lateral ground strain associated with the highest levels of ground distortion. The largest ground deformations, defined on the basis of the statistical exceedance values, are located throughout Christchurch with Geographic Information Systems (GIS) and evaluated with respect to various landforms and waterways in the Christchurch alluvial plain. Various probability distributions are investigated to find the distribution that best fits the distributions of vertical and lateral ground deformation. Finally, the relationship between ground

deformation from LiDAR measurements and the deformation of timber frame residential buildings is investigated by collecting and analyzing survey data for buildings damaged by liquefaction-induced ground movements. The building deformations are compared with differential vertical and lateral ground strain parameters derived from LiDAR measurements at the building locations.

## **5.2 LiDAR Data**

Airborne and terrestrial LiDAR have been used extensively for monitoring and evaluating ground displacements caused by hazards, such as earthquakes, floods, landslides and debris flows [5.3] [5.4] [5.5] [5.6]. Airborne LiDAR data were used to evaluate elevation change in liquefied areas during the 2011 Tohoku-Oki earthquake [5.7]. LiDAR data were also used in conjunction with the 2010-2011 CES for investigating fault kinematics and surface deformations after the 4 Sept. 2010 earthquake [5.8], mapping earthquake induced topographical change and liquefaction in the Avon-Heathcote Estuary [5.9], correlating LiDAR-based ground movements and liquefaction vulnerability indicators [5.10], investigating seismically triggered rockfalls in the Port Hills [5.11], comparing LiDAR-based lateral spreading ground movements with empirical predictions of lateral spreading [5.12], and correlating pipeline [5.13] and building damage [5.14] with LiDAR-based measurements of liquefaction-induced ground movement land damage indices.

Airborne LiDAR surveys were flown before and after each of the main earthquakes in the CES by AAM Brisbane (AAM) and New Zealand Aerial Mapping (NZAM). In addition to LiDAR surveys during the CES, LiDAR measurements acquired on 6-9 July 2003 and 21-24 July 2005 were commissioned by the Christchurch City Council (CCC). Pairs of these data were used by GNS Science (GNS) under contract with Tonkin & Taylor Pty Ltd (T&T) to determine horizontal and vertical ground movements. Information about LiDAR sets used in this study is provided by Beavan et al. [5.15] and is summarized in Table 5.1. The LiDAR measurements acquired on 6-9 July 2003 and 21-24 July 2005 were combined to provide the vertical digital elevation model (DEM) of the Christchurch area before the 4 September 2010 earthquake. Likewise, two sets of LiDAR measurements were obtained after the 22 Feb. 2011 earthquake and are shown in Table 5.1. LiDAR surveys were typically undertaken a month after each main earthquake (with the exception of the post-September 2010 LiDAR which was flown the day after the earthquake). This delay provided time for ejected sand and silt to be removed from most sites to allow the measurement of actual changes to the ground surface level. The extent of LiDAR coverage varied after each earthquake.

The LiDAR elevation point clouds were used to develop bare earth digital elevation models (DEMs) at 5-m spacing by averaging the ground-return elevations within 5 m x 5 m cells. The vertical LiDAR point clouds and the bare earth DEMs measured before and after each earthquake were also calibrated against field survey

data supplied by CCC, Land Information New Zealand (LINZ) and Environment Canterbury from surveys of their benchmark networks [5.16]. The NZAM LiDAR give a fundamental vertical accuracy of  $\pm 10$  cm for areas of open ground with hard surfaces, and the AAM LiDAR give a fundamental vertical accuracy of  $\pm 7$  to  $\pm 15$  cm [5.15]. The accuracy of the LiDAR data after the 4 September 2011 earthquake is  $\pm 7$  cm [5.17]. The pre-earthquake LiDAR has lower accuracy with sparser LiDAR point sets than the post-earthquake sets [5.17].

Table 5.1. LiDAR datasets collected and used in this study.

<b>Name</b>	<b>Code</b>	<b>Acquisition Dates</b>	<b>Contractor</b>
Pre-Earthquake	2003	6-9 July 2003	AAM <sup>1</sup>
	2005	21-24 July 2005	AAM
Post-4 Sept. 2010	2010_central	5 Sept. 2010	NZAM <sup>2</sup>
Post-22 Feb. 2011	2011a	8-10 Mar 2011	NZAM
	2011b	20-30 May 2011	AAM
Post-13 June 2011	2011c	18 July - 3 Sep 2011	NZAM
Post 24 Dec. 2011	2012a	17-18 Feb. 2012	NZAM
<sup>1</sup> Australian Aerial Mapping Ltd.		<sup>2</sup> New Zealand Aerial Mapping Ltd.	

LiDAR lateral movements were originally calculated at 4-m and 8-m spacing, and were averaged to provide lateral movements at 56 m spacing. They were calculated using a sub-pixel correlation method developed by Imagin'Labs Corporation, Pasadena, CA, and California Institute of Technology [5.15]. The AAM LiDAR horizontal accuracy, compared to land survey measurements supplied by CCC, LINZ and Environment Canterbury, is 40 to 55 cm [5.15]. Hence, 2-D displacements greater

than approximately 40 cm can be reliably detected over large parts of each image, except for areas of significant noise.

### 5.3 Study Area

It is well established that areas of heavy vegetation contribute to errors in LiDAR measurements [5.18]. A special study area, therefore, was established to evaluate LiDAR-based measurements of ground deformation from which locations with a high density of vegetation and multi-story building damage were removed. The study area is shown in Figure 5.1 and includes those portions of Christchurch surrounding the Avon River. Areas greater than 0.1 km<sup>2</sup> and covered by vegetation were identified in ArcMap 10.1 [5.19] using geospatial data of land parcels available through LINZ [5.20], and removed from the study area. They are identified in Figure 5.1 as areas No. 2 through 10. Because of errors related to damage, distortion, and demolition of high rise buildings, the Christchurch Central Business District (CBD), identified as area No.1, was also excluded from the study area.

Vertical differential ground movement, expressed in dimensionless terms as angular distortion,  $\beta$ , was selected as the main vertical movement parameter in this work. The horizontal deformation parameter was chosen as the absolute value of maximum ground strain,  $\epsilon_{HP}$ . The methodology for calculation of  $\epsilon_{HP}$  was based on plane strain conditions for quadrilateral elements as described Chapter 3. Finite element formulations were used to determine horizontal ground strains according to

the method described by Cook [5.21] using LiDAR lateral movements in the east-west (EW) and north- south (NS) directions.

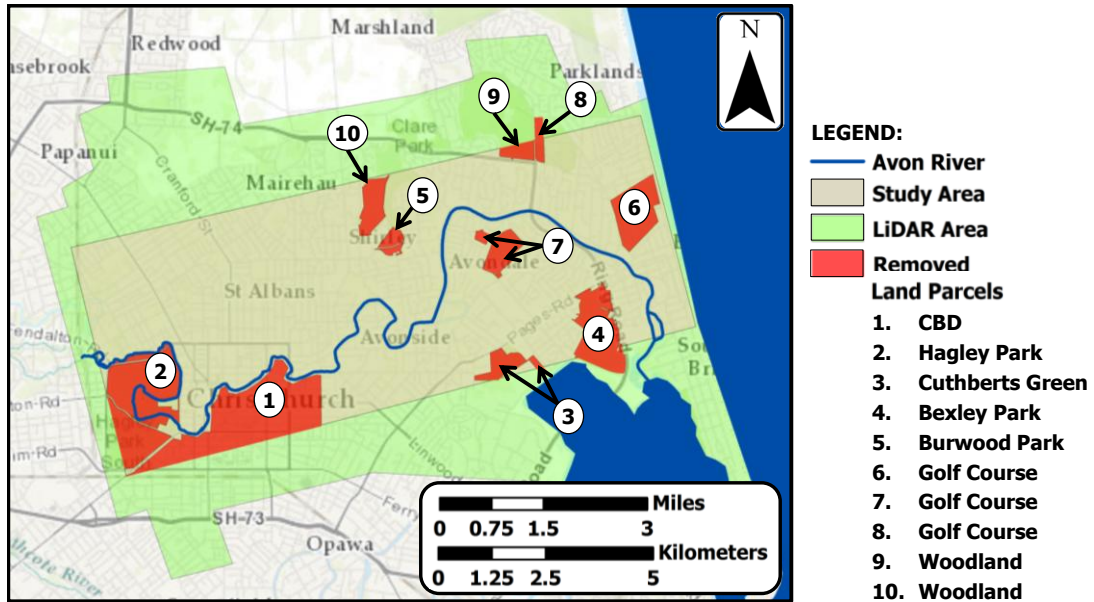


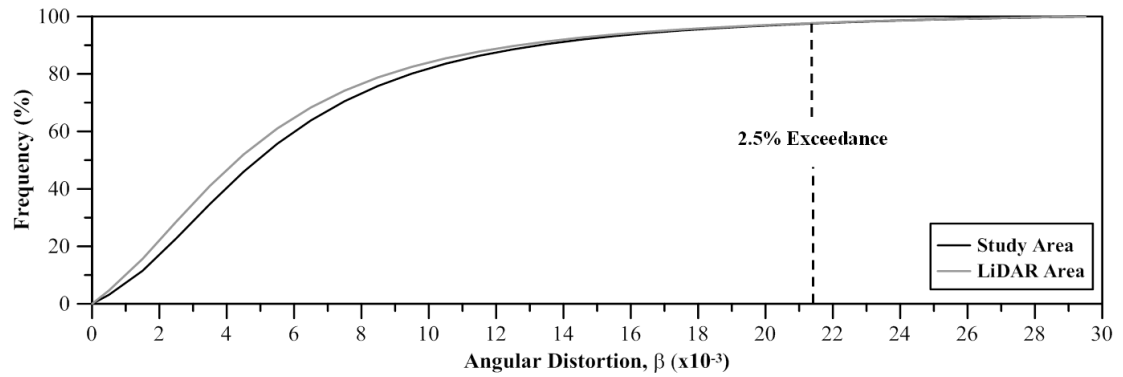
Figure 5.1. Study area and removed land parcels superimposed on the LiDAR area in Christchurch.

The vertical and horizontal ground surface movements developed by pairs of high-resolution LiDAR data sets were used to calculate differential vertical ground movement,  $\beta$ , and lateral ground surface strain,  $\epsilon_{HP}$ , at 5-m and 4-m spacing, respectively. The calculation of  $\beta$  and  $\epsilon_{HP}$  was performed both for each main seismic event and for sets of consecutive earthquakes. Dislocation models of vertical and lateral tectonic movement for each earthquake were applied to the LiDAR sets of vertical and lateral ground surface movement, respectively, to correct the data for

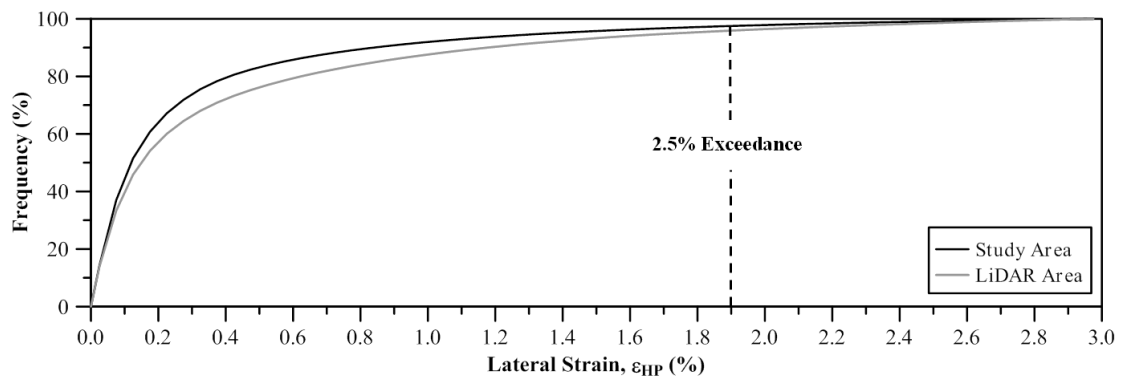
tectonic movement. The dislocation models are available through GNS Science [5.22] and are based on geodetic observations, mainly GPS and satellite radar [5.15].

Very high values of  $\beta$  and  $\varepsilon_{HP}$  were screened from the data for additional reduction of erroneous measurements. Values of  $\beta \leq 30 \times 10^{-3}$  were selected and binned at intervals of  $1 \times 10^{-3}$  to perform statistical analyses. Similarly, values of  $\varepsilon_{HP} \leq 3\%$  were selected and binned at intervals of 0.05% for statistical analyses. Values of  $\beta > 30 \times 10^{-3}$  and values of  $\varepsilon_{HP} > 3\%$  represent approximately 3% to 5%, respectively, of the total population.

Cumulative distributions of  $\beta$  and  $\varepsilon_{HP}$  resulting from the 22 Feb. 2011 earthquake in the study area are shown in Figure 5.2a and Figure 5.2b, respectively, and are compared with the cumulative distributions of  $\beta$  and  $\varepsilon_{HP}$  from all LiDAR measurements in central Christchurch for the same earthquake. The cumulative distributions for  $\beta$  are in close agreement and converge rapidly for large  $\beta$  values. In contrast, the cumulative distributions for  $\varepsilon_{HP}$  diverge at low values of  $\varepsilon_{HP}$  and show a relatively wide gap between the lateral strains from all LiDAR data and the lateral strains for the study area. As  $\varepsilon_{HP}$  increases, the gap between the two cumulative distributions increases. In essence, the cumulative distribution for all LiDAR data is long-tailed with a greater proportion of large  $\varepsilon_{HP}$  values that reflect LiDAR measurement errors associated with vegetation.



a)



b)

Figure 5.2. Cumulative distributions of a) ground angular distortion, and b) lateral ground strain in the LiDAR and study areas.

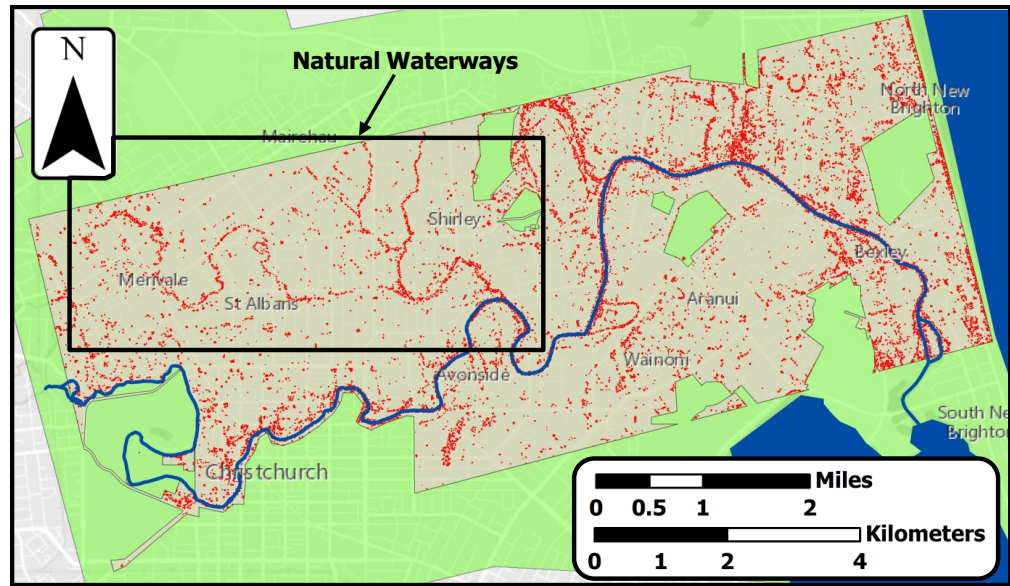
#### 5.4 Statistical Screening for Ground Deformation Patterns

The statistical distributions for  $\beta$  and  $\epsilon_{HP}$  in the study area were used to identify and locate the occurrences of largest ground deformation. Values of  $\beta$  and  $\epsilon_{HP}$ , representing the upper 2.5% of the data in Figure 5.2a and Figure 5.2b, respectively, were located within the study area shown in Figure 5.3a and Figure 5.3b, respectively. Ground angular distortions greater than  $21.3 \times 10^{-3}$ , representing 2.5% of the study area  $\beta$  values, are shown in Figure 5.3a. They are concentrated close to the Avon River and in areas of natural waterways. Similarly, lateral ground strains greater than 1.9%,

representing 2.5% of the  $\epsilon_{HP}$  values, are shown in Figure 5.3b. They are concentrated primarily close to the Avon River, Horseshoe Lake, and areas affected by lateral spreading, such as Porritt Park, Anzac Drive, and Queen Elizabeth II Stadium.

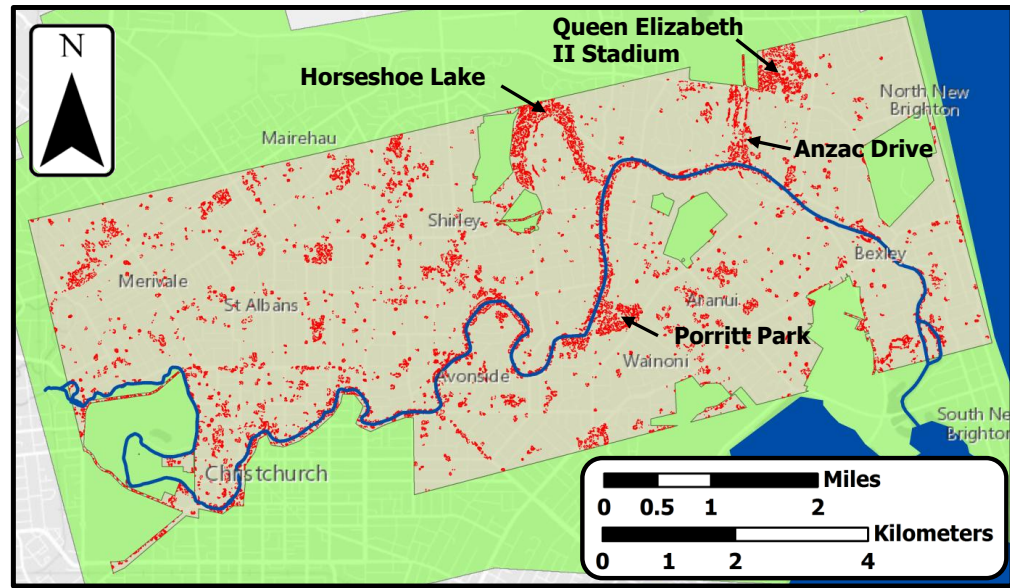
The most notable feature of Figure 5.3a is the way the 2.5% exceedance values of  $\beta$  align themselves clearly with water courses in Christchurch. Even small streams in the area, identified as Natural Waterways in Figure 5.3a, are delineated by the  $\beta$  locations. The 2.5% exceedance values of  $\beta$  provide a remarkably accurate measure for locating all sizes and types of natural water courses and previous meanders of Avon River.

The 2.5% exceedance values of  $\epsilon_{HP}$  in Figure 5.3b align themselves with locations adjacent to the Avon River and its cut-off meanders, such as Horseshoe Lake and Porritt Park. However,  $\epsilon_{HP}$  is not effective in locating streams within the area identified as Natural Waterways. The  $\epsilon_{HP}$  data tend to cluster in small areas of vegetation that were not removed from the study area, as illustrated by the locally high densities of  $\epsilon_{HP}$  throughout the map. Because of local vegetation, the 2.5% exceedance values of  $\epsilon_{HP}$  are clustered around Horseshoe Lake and Porritt Park. They lack the refinement associated with  $\beta$ , which defines the water courses with considerable precision.



— AvonRive    Study Area    LiDAR Area    2.5% Angular Distortion

a)



— AvonRive    Study Area    LiDAR Area    2.5% Lateral Ground Strain

b)

Figure 5.3. Spatial distribution of the 2.5% exceedance values of a) ground angular distortion, and b) lateral ground strain caused by the 22 Feb. 2011 earthquake in the study area.

Figure 5.4 provides an expanded view of the Natural Waterways area identified in Figure 5.3a. Rivers, streams, and open drains were obtained from historic maps of the stormwater drainage system in Christchurch as of 1989 [5.23] and plotted in blue in Figure 5.4. There is very close agreement between the locations of these natural waterways and the 2.5% exceedance values of  $\beta$ .

Figure 5.5 compares the spatially distributed 2.5% exceedance values of both  $\beta$  and  $\varepsilon_{HP}$  in the Saint Albans area, located north of the Christchurch CBD. The stream in the Saint Albans area runs below streets and residential driveway bridges, and its path is followed very closely by the 2.5% exceedance values of  $\beta$ . In contrast, the 2.5% exceedance values of  $\varepsilon_{HP}$  do not follow the path of the stream. Instead, they are concentrated at trees and vegetated areas, as is shown in particular for Abberley Park.

## 5.5 Probability Distributions

When analyzing the statistical distributions of ground movement for the main shocks of the CES, many different mathematical formulations were investigated as candidates for fitting the actual data. It was found that the generalized extreme value distribution (GEV) is the most suitable to describe  $\beta$  and  $\varepsilon_{HP}$ . The probability density function for the GEV is given by

$$f(x|\gamma_{GEV}, \mu_{GEV}, \sigma_{GEV}) = \frac{1}{\sigma_{GEV}} \exp\left(-\left(1 + \gamma_{GEV} \frac{(x - \mu_{GEV})}{\sigma_{GEV}}\right)^{\frac{1}{\gamma_{GEV}}}\right) \left(1 + \gamma_{GEV} \frac{(x - \mu_{GEV})}{\sigma_{GEV}}\right)^{-1 - \frac{1}{\gamma_{GEV}}} \quad (5.1)$$

for  $1 + \gamma_{GEV} \frac{(x - \mu_{GEV})}{\sigma_{GEV}} > 0$  and  $\gamma_{GEV} \neq 0$

in which  $\mu_{GEV}$  is the location parameter that determines the location or shift of the distribution,  $\sigma_{GEV}$  is the scale parameter that determines the statistical dispersion of the distribution, and  $\gamma_{GEV}$  is the shape parameter that affects the shape of the distribution. The GEV is a family of distributions developed within extreme value theory to combine the Gumbel, Fréchet and Weibull families, known as type I, II, and III extreme value distributions, respectively. It has been used as the basic distribution tool in several applications, such as risk management [5.24], flood frequency analysis [5.25], and system reliability [5.26]. The Matlab function `gevfit` was used to estimate the parameters for the GEV distributions of  $\beta$  and  $\varepsilon_{HP}$  and corresponding confidence intervals using maximum likelihood functions.

## **5.6 Ground Angular Distortion and Vertical Movement**

Normalized histograms and cumulative distributions of  $\beta$  for the 4 Sept. 2010, the 22 Feb. 2011, and the 13 June 2011 earthquakes are presented in Figure 5.6. The histograms are binned at  $1 \times 10^{-3}$  intervals. As indicated previously, very high values of  $\beta \geq 30 \times 10^{-3}$  were screened from the data. Vertical LiDAR displacements pertaining to each earthquake were corrected for tectonic movement, respectively, available through GNS Science [5.22].

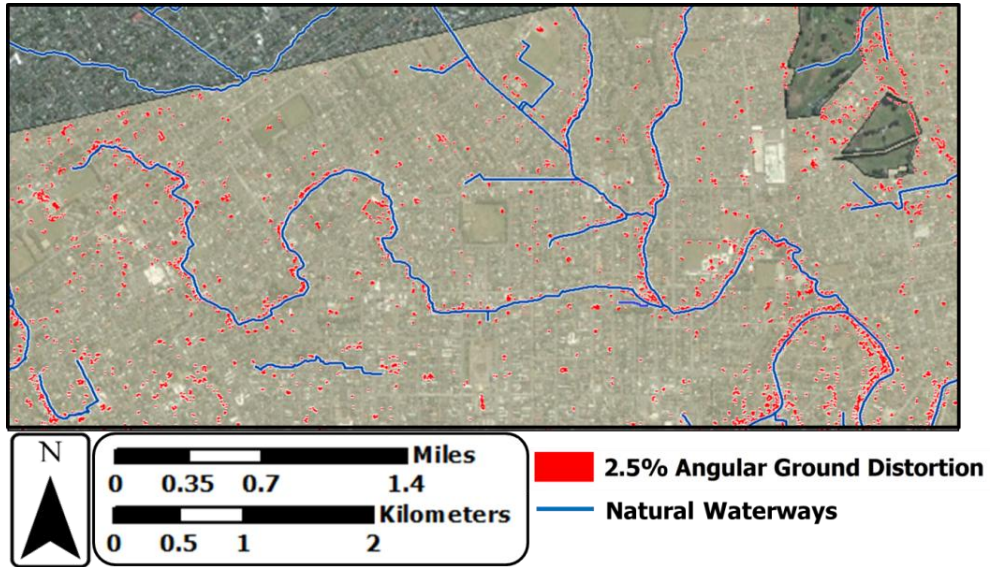


Figure 5.4. Patterns of 2.5% exceedance values of ground angular distortion caused by the 22 Feb. 2011 earthquake superimposed by rivers, streams, and open drains as of 1989 [5.23].

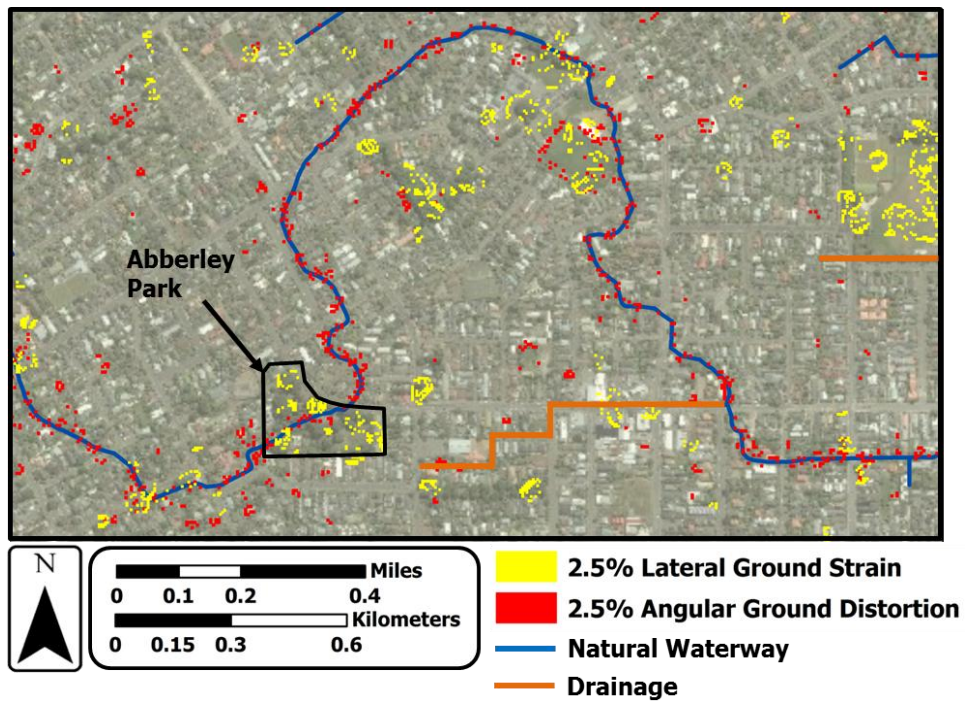


Figure 5.5. Patterns of the 2.5% exceedance values of lateral ground strain and ground angular distortion caused by the 22 Feb. 2011 earthquake in St. Albans area superimposed by existing natural waterways.

The GEV distributions for  $\beta$  related to each earthquake are shown in Figure 5.6. The GEV distribution provides a good fit for each event. There is a remarkable similarity in the histograms and cumulative distributions for the 22 Feb. 2011, and the 13 June 2011 earthquakes, and a marked difference in same for the 4 Sept. 2010 earthquake. As shown in Figure 5.6b, approximately 70% of  $\beta$  population during the 4 Sept. 2010 earthquake in the study area is greater than  $7 \times 10^{-3}$ , whereas this population is reduced to approximately 35% for the 22 Feb. 2011 and 13 June 2011 earthquakes.

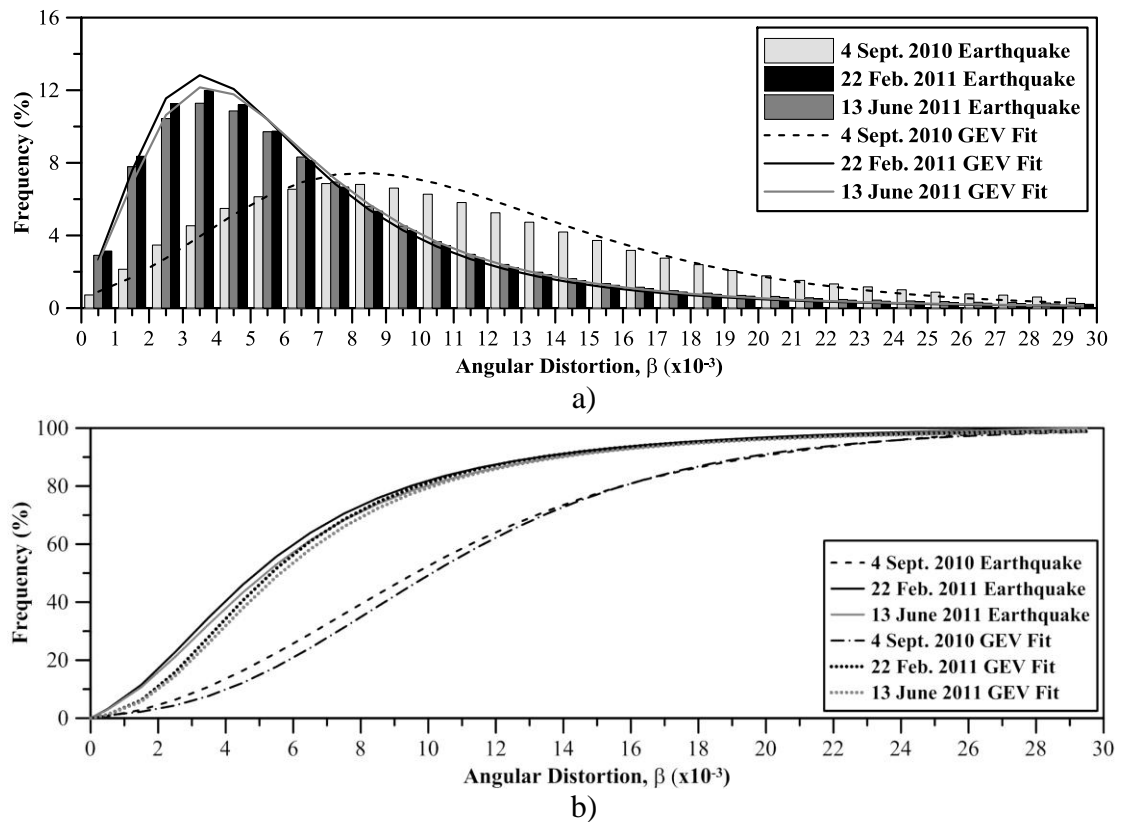


Figure 5.6. a) Normalized histograms, and b) cumulative distributions of LiDAR-based ground angular distortions in the study area during the 4 Sept. 2010, 22 Feb. 2011, and 13 June 2011 earthquakes.

The angular distortion associated with the 4 Sept. 2010 earthquake was locally more severe in comparison with the other two earthquakes. Liquefaction, however, was less extensive in terms of spatial coverage during the 4 Sept. 2010 earthquake. Using areas of documented liquefaction obtained through the Canterbury Geotechnical Database [5.27], liquefaction effects were observed and mapped in approximately 52 km<sup>2</sup>, or 32% of the Christchurch area. In contrast, 96 km<sup>2</sup> and 91 km<sup>2</sup> (66% and 62% of the Christchurch area, respectively) were associated with liquefaction during the 22 Feb. 2011 and 13 June 2011 earthquakes, respectively.

A large portion of liquefaction in 4 Sept. 2010 was concentrated along the Avon River and its cut-off meanders. Slumping and heave in the river and the oxbow lake at Horseshoe Lake may have diminished local slopes and elevation gradients so that liquefaction effects in subsequent earthquakes, although more extensive, were less severe overall with respect to angular distortion.

Figure 5.7a and Figure 5.7b show the normalized histograms and cumulative distributions, respectively, of LiDAR vertical displacements during each earthquake. Negative and positive values refer to settlement and heave, respectively. The histograms are binned at 0.25-m intervals. Based on the cumulative distributions in Figure 5.7b, approximately 21%, 5.4%, and 15% of the populations are associated with heave for the 4 Sept. 2010, 22 Feb. 2011, and the 13 June 2011 earthquakes, respectively.

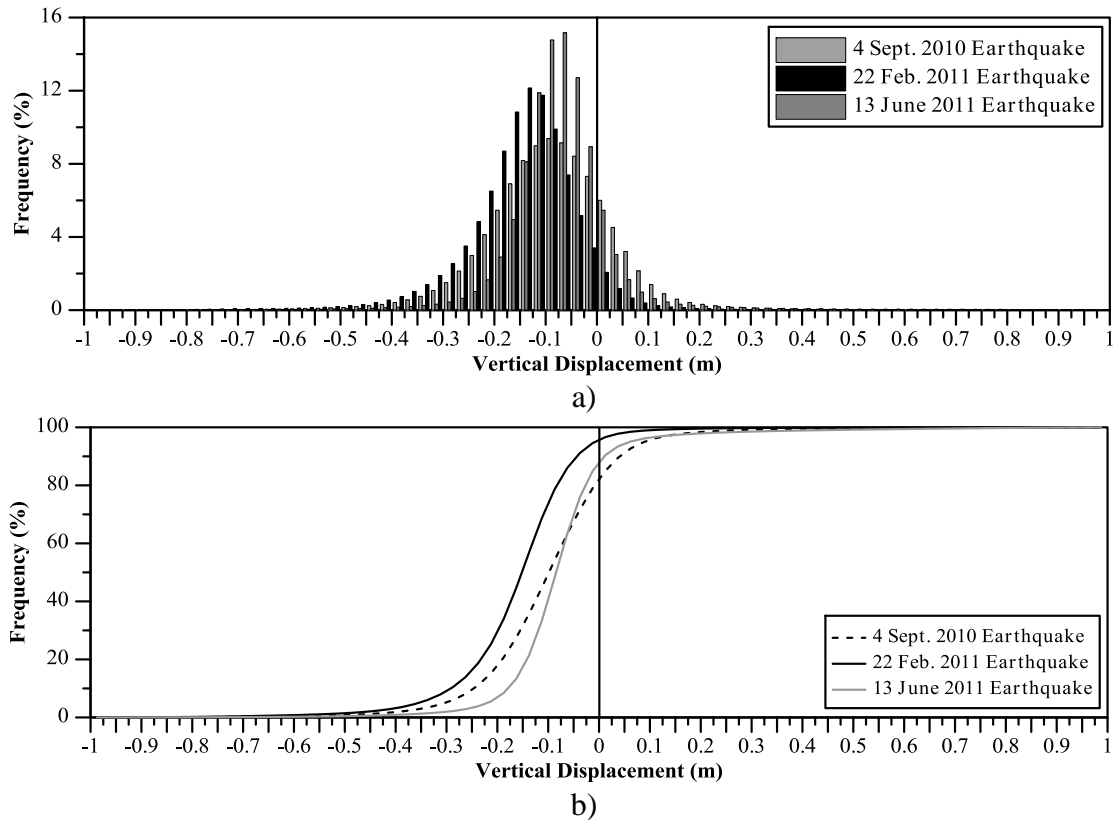


Figure 5.7. a) Normalized histograms, and b) cumulative distributions of LiDAR-based vertical displacements in the study area during the 4 Sept. 2010, 22 Feb. 2011, and 13 June 2011 earthquakes.

## 5.7 Lateral Ground Movement and Lateral Ground Strain

Figure 5.8a and Figure 5.8b show the normalized histograms and cumulative distributions, respectively, of LiDAR lateral displacements during each earthquake. The histograms are binned at 0.25-m intervals. The cumulative distributions of lateral displacement are similar for both the 4 Sept 2010 and 22 Feb. 2011 earthquakes. It appears that overall the severity of lateral spreading was comparable for these two earthquakes, although the area affected by liquefaction in 22 February 2011 was roughly twice as large as that in 4 Sept. 2010. The cumulative distribution of lateral

displacement for the 13 June 2011 earthquake shows substantially lower levels of movement.

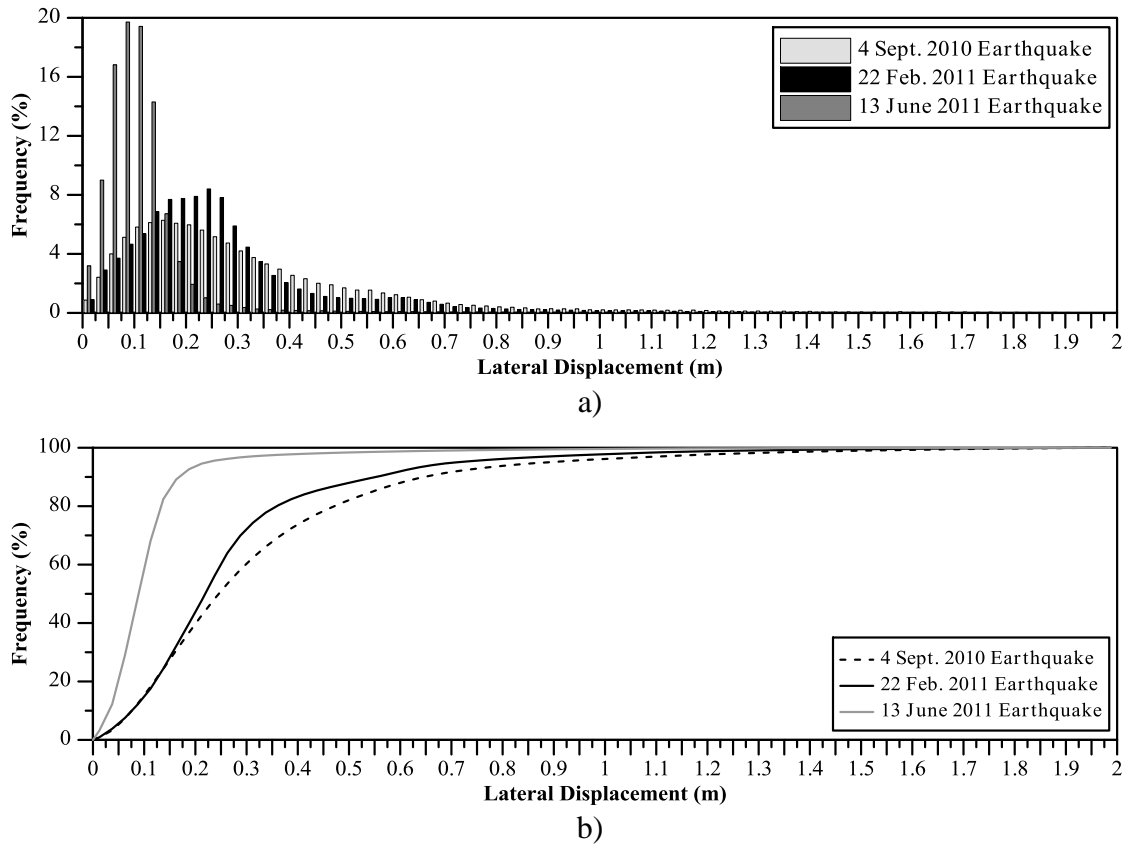


Figure 5.8. a) Normalized histograms, and b) cumulative distributions of LiDAR lateral displacements in the study area during the 4 Sept. 2010, 22 Feb. 2011, and 13 June 2011 earthquakes.

Figure 5.9 shows the normalized histograms and cumulative distributions of LiDAR-based tensile and compressive  $\epsilon_{HP}$  for the 4 Sept. 2010, 22 Feb. 2011, and 13 June 2011 earthquakes. The histograms are binned at 0.05% intervals. For all three earthquakes, LiDAR-based  $\epsilon_{HPS}$  were approximately equally either tensile or compressive strains. The GEV distributions for  $\epsilon_{HP}$  related to each earthquake are shown in Figure 5.9. The GEV distribution provides a good fit for each event.

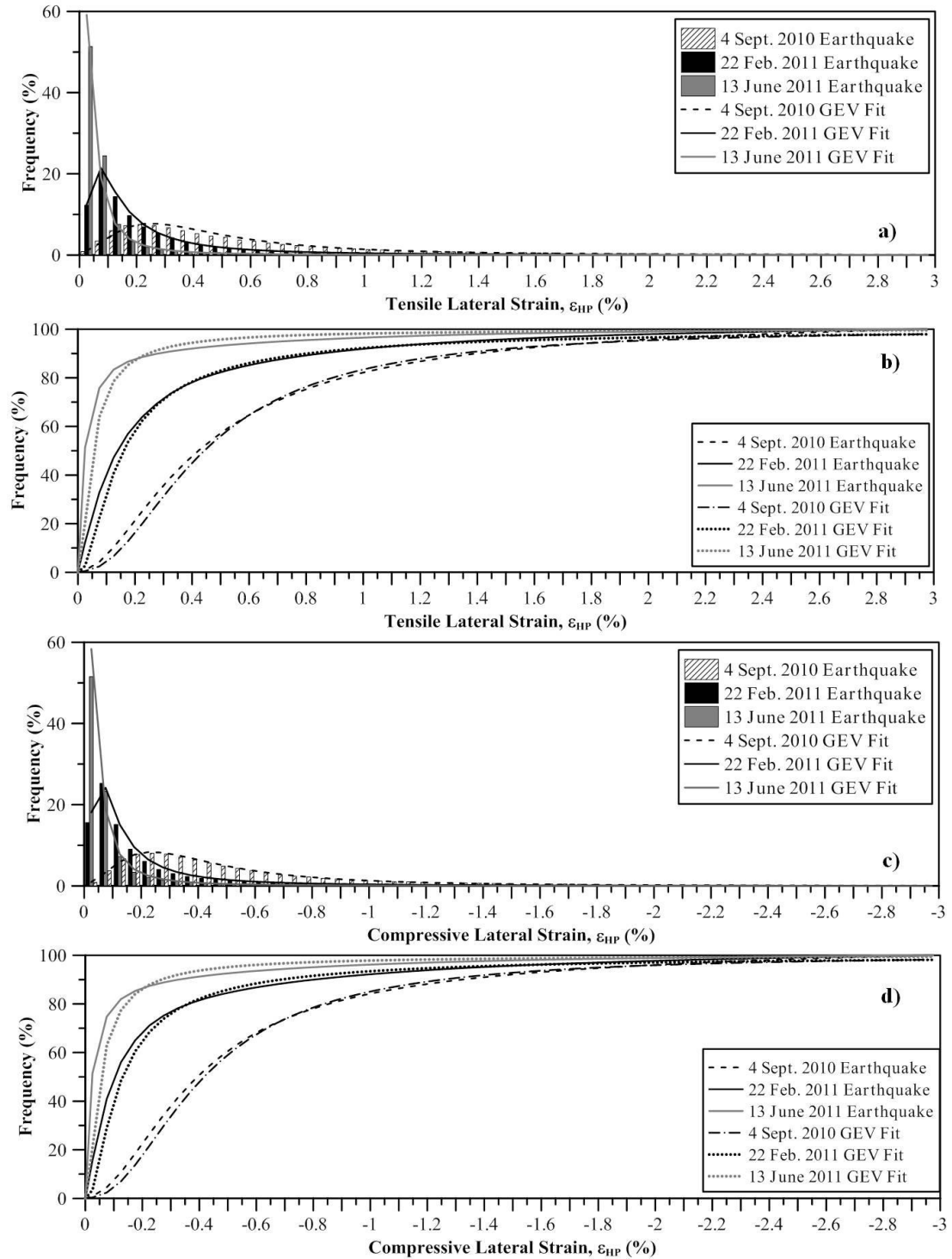


Figure 5.9. Normalized histograms and cumulative distribution of LiDAR-based tensile and compressive lateral ground strains in the study area during the 4 Sept. 2010, 22 Feb. 2011, and 13 June 2011 earthquakes.

The normalized histograms and cumulative distributions are virtually identical for tensile and compressive strains. The largest lateral strains are associated with the 4 Sept. 2010 earthquake. In contrast to the lateral movements, the cumulative distribution of  $\epsilon_{HP}$  for the 22 Feb. 2011 earthquake shows levels of lateral strain significantly less than those for the 4 Sept. 2010 earthquake. This comparison suggests that the largest lateral movements overall were concentrated in narrower zones adjacent to the Avon River and other water courses in 4 Sept. 2010, and that lateral movements were spread over larger horizontal distances in 22 Feb. 2011.

Table 5.2 provides a summary of the mean and standard deviation of each population of  $\beta$ , vertical displacement, lateral displacement, and tensile and compressive  $\epsilon_{HP}$  pertaining to each earthquake. Table 5.3 provides a summary of the GEV estimated parameters for  $\beta$  and tensile and compressive  $\epsilon_{HP}$  pertaining to each earthquake.

Table 5.2. Summary of statistical parameters for each LiDAR-based ground parameter during each earthquake.

<b>Earthquake:</b>	<b>4 Sept. 2010</b>		<b>22 Feb. 2011</b>		<b>13 June 2011</b>	
<b>Statistical Parameter:</b>	<b>Mean</b>	<b>StDev</b>	<b>Mean</b>	<b>StDev</b>	<b>Mean</b>	<b>StDev</b>
Angular Distortion, $\beta$ ( $10^{-3}$ )	11.14	6.28	6.83	5.24	7.13	5.42
Vertical Displacement (m)	-0.09	0.16	-0.15	0.19	-0.07	0.14
Lateral Displacement (m)	0.34	0.28	0.29	0.23	0.12	0.12
Tensile Lateral Strain, $\epsilon_{HP}$ (%)	0.64	0.57	0.34	0.47	0.15	0.35
Compressive Lateral Strain, $\epsilon_{HP}$ (%)	-0.60	0.55	-0.31	0.48	-0.16	0.36

Table 5.3. Summary of GEV estimated parameters for each LiDAR-based ground parameter during each earthquake.

Earthquake:	4 Sept. 2010			22 Feb. 2011			13 June 2011		
GEV Parameter:	$\gamma_{GEV}$	$\mu_{GEV}$	$\sigma_{GEV}$	$\gamma_{GEV}$	$\mu_{GEV}$	$\sigma_{GEV}$	$\gamma_{GEV}$	$\mu_{GEV}$	$\sigma_{GEV}$
Angular Distortion, $\beta$ ( $10^{-3}$ )	0.4817	0.0055	0.0047	0.3137	0.0056	0.0051	0.1691	0.0063	0.0059
Tensile Lateral Strain, $\varepsilon_{HP}$ (%)	0.4304	0.0026	0.0034	0.8019	0.0011	0.0011	0.7950	0.0003	0.0004
Compressive Lateral Strain, $\varepsilon_{HP}$ (%)	0.4362	0.0024	0.0032	0.8411	0.0009	0.0009	0.8350	0.0003	0.0004

## 5.8 LiDAR-Based Ground Deformations vs Foundation Deformations

Liquefaction effects during the CES caused severe damage to approximately 20,000 residential properties and led to evacuation of approximately 7,000 houses in areas that were mostly affected by PGD [5.14]. LiDAR-based lateral ground strains and angular distortions are used in this study to investigate correlations between ground deformation and residential building damage during the CES. Ground deformations, expressed as lateral strain and angular distortion, have been used successfully in geotechnical engineering to evaluate ground movement effects on buildings [5.28] [5.29].

Residential houses in Christchurch are generally light timber-framed one-story structures with weatherboard, unreinforced brick veneer, and stucco used as exterior cladding. Four principal shallow foundation system types have generally been used for residential buildings in Christchurch: concrete perimeter footings with short piers, short piers without perimeter footings, concrete slab on grade, and more recently ridge-rafter or waffle slab with inverted beams [5.2]. Typical slab on grade foundations are

concrete mats, approximately 100 mm thick, sometimes with wire mesh reinforcement.

A detailed damage survey was conducted in June 2013 on five residential properties located in the Mairehau and Shirley neighborhoods of Christchurch. These properties are shown in Figure 5.10 in red color and represent typical residential properties. Three buildings in the field survey had concrete perimeter footings, one had slab-on-grade floor, and one was resting on short piers with concrete footings at the corners. Measurements of cracks at the concrete perimeter footings were performed to evaluate foundation damage due to lateral spreading. Permission to inspect the buildings was given by the Housing New Zealand Corporation. The inspections were performed with assistance from Tonkin & Taylor, Ltd, who provided settlement surveys of the buildings, which were conducted by civil engineering firms working for the Housing New Zealand Corporation.

The inspection of each building with concrete perimeter footings involved locating, mapping, and measuring vertical cracks greater than 2 mm in thickness around the entire building perimeter. It was assumed that the cracks were caused primarily by liquefaction-induced lateral ground movement. The summation of the crack widths for each of the four perimeter footings was assumed to represent the extension displacement of each footing, half of which was allocated to each end of the footing. By allocating horizontal displacements in the same way for the four sides of

the perimeter foundation, orthogonal movements at each corner of the rectangular foundation were estimated.

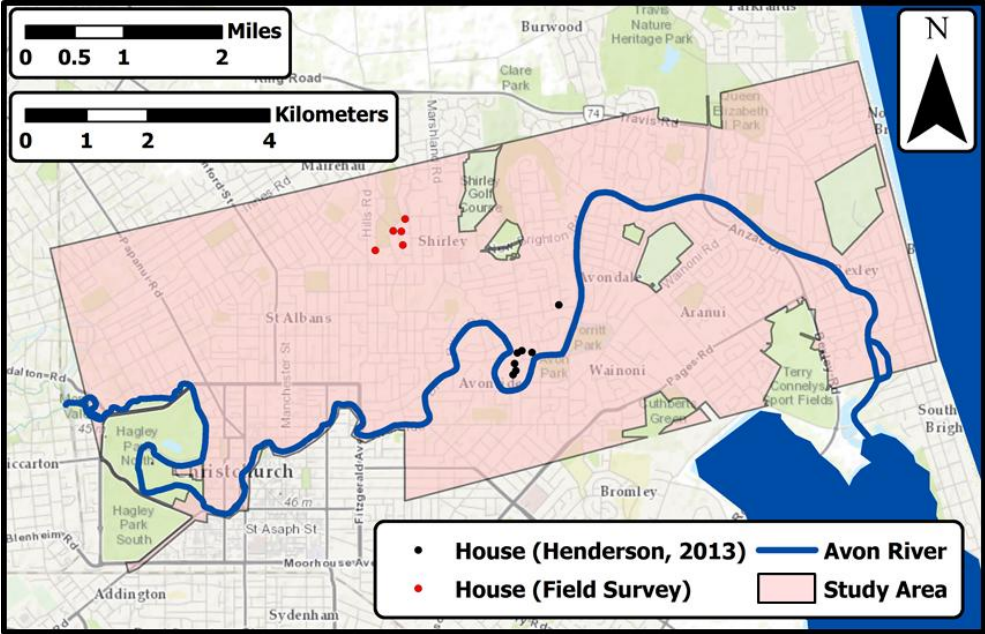


Figure 5.10. Locations of residential properties inspected during field survey, and residential properties inspected by Henderson [5.14] within the study area.

Calculation of lateral strains at the concrete perimeter footings was performed using quadrilateral finite element formulations. Figure 5.11 shows a schematic of the calculation process for lateral strains that was followed. As shown in Figure 5.11, the concrete perimeter footing at the base of the building is assumed to reflect the shape of a quadrilateral element, and the perimeter corners are assumed to be corner points of the elements with displacements in the x- and y- directions. The sum of cracking measurements at the foundation perimeter on each side of the building was evenly distributed at the two corners on either end of each side. Element principal strains were calculated using lateral displacements in the x- and y- directions at the corners of

the element, and the absolute maximum value of principal lateral ground strains,  $\epsilon_{HPB}$ , was used to represent foundation lateral strain in each building.

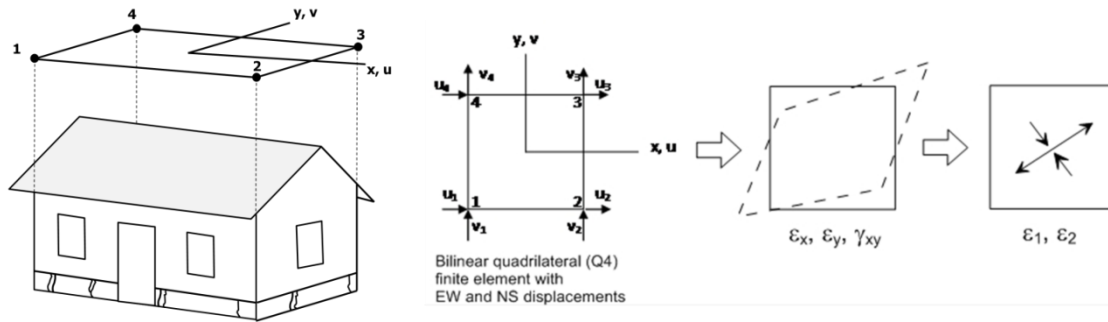


Figure 5.11. Calculation of lateral strains at surveyed residential buildings using quadrilateral finite element formulations.

Lateral ground strains derived from LiDAR measurements collected before the 4 Sept. 2010 and after the 23 Dec. 2011 earthquakes were used to evaluate the LiDAR-based absolute value of the maximum lateral ground strain,  $\epsilon_{HP}$ , associated with each building. The 4-m cells for  $\epsilon_{HP}$  calculation at each building were identified in ArcMap 10.1 [5.19], and the  $\epsilon_{HP}$  was calculated as the average value of  $\epsilon_{HP}$  corresponding to the footprint of the building.

Foundation differential vertical displacements were calculated using data for the ground floor level of each building from the surveys provided by Tonkin & Taylor, Ltd., which were performed after the 13 June 2011 earthquake, but before the 23 December 2011 earthquake. Each measurement was related to a reference point located near the building entrance. Measurement locations, recorded on the floor plans

of each house, were used in the calculation of differential vertical displacement contour plots of the ground floor in each surveyed house.

Contour plots of differential vertical displacement in 10-mm increments were developed in ArcMap 10.1. Figure 5.12 shows the contour plots of differential vertical displacement for the residential building with a slab on grade foundation. As shown in Figure 5.12, the contour plots were developed for each of two residences separated by a central garage. An equivalent floor slope was calculated to represent the predominant ground level slope for each residence, as shown in Figure 5.12. A similar process was followed for the other buildings in Figure 5.10 and the resulting contour plots for the other residential buildings included in the field survey are provided in Appendix D.

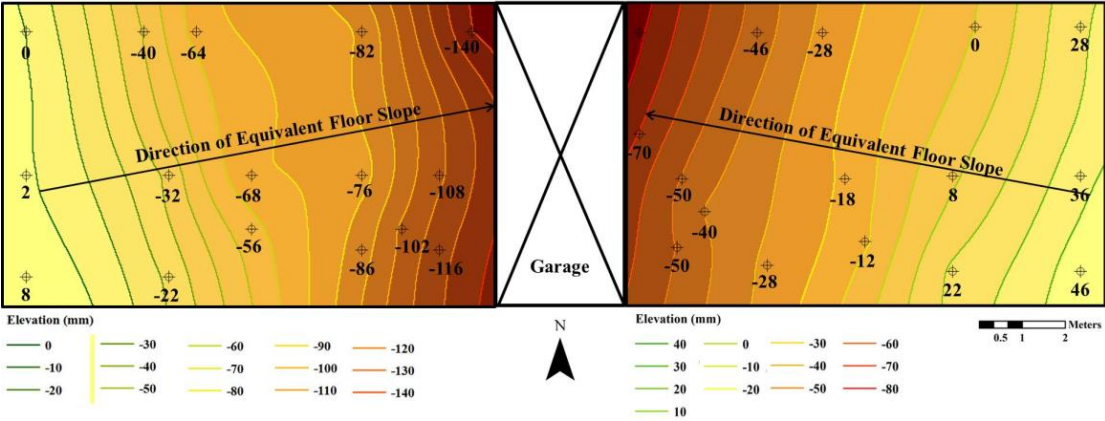


Figure 5.12. Contour plots of differential vertical displacement on the ground floor of a surveyed building with two individual residences and their equivalent floor slopes.

In addition to the five surveyed residential properties, seven additional houses were added to this study. Observations and data for the seven additional houses were

collected and described by Henderson [5.14]. These properties are shown in Figure 5.10 in black. They were located in the Dallington area, which was affected by liquefaction during each major earthquake. Inspections were conducted on the seven residential properties after the 13 June 2011 earthquake through September 2011. Floor level data were collected and contour plots of differential vertical displacement of the ground floors were developed by Henderson [5.14] for each of the seven buildings. The contour plots were used to estimate the equivalent floor slopes following the same process that was used for the five surveyed buildings.

LiDAR measurements for the combined effects of the 4 Sept. 2010, 22 Feb. 2011 and 13 June 2011 earthquakes were used to estimate  $\beta$  and were compared with the equivalent floor slope for the five surveyed buildings and the seven additional buildings inspected by Henderson [5.14]. The effects of the 23 Dec. 2011 earthquake were not taken into account because the surveys were conducted prior to the 23 Dec. 2011 earthquake. The 5-m cells for  $\beta$  calculation for each of the three surveyed buildings were identified in ArcMap 10.1 [5.19], and the  $\beta$  associated with each building was calculated as the average of ground angular distortion values overlaying the approximate footprint of the building.

Foundation lateral strain,  $\epsilon_{HPB}$ , and the absolute value of maximum lateral ground strain,  $\epsilon_{HP}$ , are plotted in Figure 5.13a for the three buildings inspected in this study. Equivalent floor slope and angular distortion,  $\beta$ , are plotted for the 12 buildings under study in Figure 5.13b. It is noted that three of the five buildings surveyed in this study

were divided into two living units with partitioning similar to that shown in Figure 5.12. Because settlement surveys were performed separately for each unit, three of the five surveys produced equivalent floor slopes for six living units, yielding a total of eight data points that were added to the seven from Henderson [5.14] for the 15 points shown in Figure 5.13b.

For the great majority of the data, the strains and distortions of the buildings are within  $\pm 50\%$  of the LiDAR-based ground strains and distortions surrounding the buildings. In most cases the equivalent floor slope is between 50% and 100% of the surrounding LiDAR-based angular distortion of the ground. The timber frame of a residential structure should be able to bridge over locally high settlements, such that its slope most of the time will be less than or equal to the ground angular distortion. This type of bias is shown in Figure 5.13b where 73% of the data are below the 1:1 line.

There are two outliers in the figures. In Figure 5.13a, the data point plotting above the 2:1 line represents a residence where cracking from lateral spreading was observed immediately adjacent to the structure. Such localized deformation would tend to amplify foundation lateral strains above the average lateral ground strains surrounding the building. Another point in Figure 5.13b, represents House #3 in the study by Henderson [5.14] that sustained high to severe foundation damage, where the east and west corners of the concrete perimeter foundation were cracked and completely separated from the rest of the foundation. Localized foundation detachment and

settlement in this case increase the equivalent floor slope well above the average distortion in the surrounding ground.

The data summarized in Figure 5.13, and especially in Figure 5.13a, are too sparse to show clear trends over a relatively wide range of lateral ground strain and angular distortion. Nevertheless, they do show that lateral building strains and floor slopes are in broad agreement with the lateral ground strains and angular distortions from LiDAR measurements at the building locations. It may be possible in the future, therefore, to correlate  $\epsilon_{HP}$  and  $\beta$  with building deformation such that the correlations on average provide a productive method for predicting building damage, and potentially the cost of that damage, for light residential timber-frame structures.

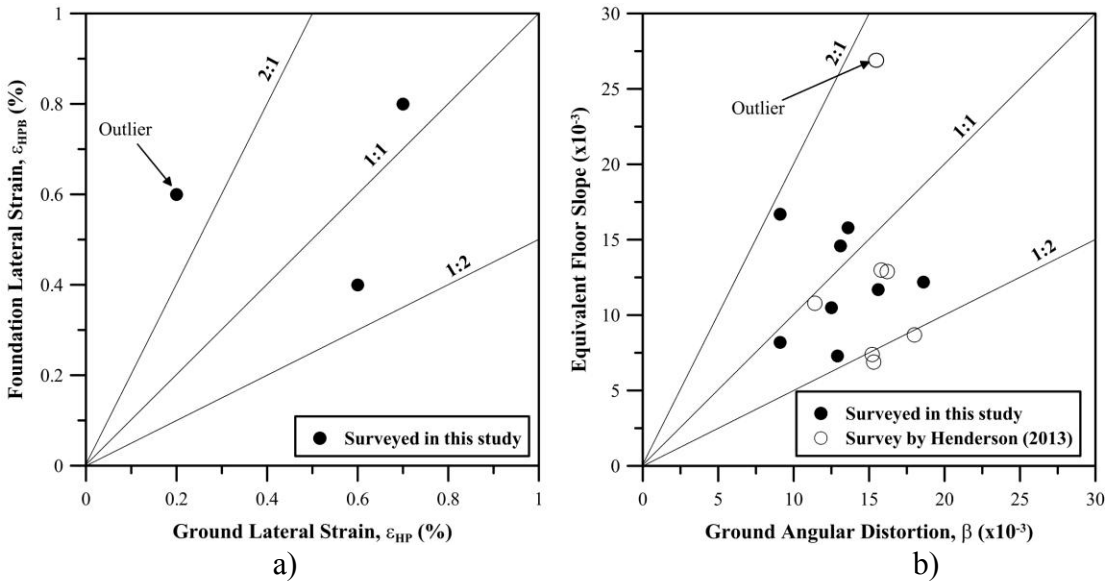


Figure 5.13. Correlations between a) foundation and ground lateral strain, and b) equivalent floor slope and ground angular distortion.

## 5.9 Conclusions

High resolution airborne light detection and ranging (LiDAR) data of vertical and lateral ground surface movement, collected during the Canterbury Earthquake Sequence (CES), were used in this study to evaluate liquefaction-induced ground deformations, expressed as vertical differential ground movement,  $\beta$ , and lateral ground strain,  $\epsilon_{HP}$ . A special study area was selected to perform the statistical evaluations by eliminating areas that contribute to LiDAR errors. The highest values of  $\beta$  and  $\epsilon_{HP}$  were identified throughout Christchurch. Statistical analyses of LiDAR-based  $\beta$  and  $\epsilon_{HP}$ , and lateral and vertical ground movements were performed for the 4 Sept. 2010, 22 Feb. 2011, and 13 June 2011 earthquakes. Finally, data from detailed damage surveys on 12 residential properties in Christchurch were used to evaluate foundation damage, expressed as lateral strain at concrete perimeter footings and differential vertical ground floor displacement, with respect to liquefaction-induced lateral ground strain and angular distortion, respectively. The principal findings of this chapter are:

- The locations of the highest values of  $\beta$  are in remarkable agreement with those of existing water courses in Christchurch and provide an accurate measure for locating all sizes and types of natural water courses and previous meanders of Avon River. On the contrary, the highest values of  $\epsilon_{HP}$  tend to cluster in small vegetated areas, which detract from LiDAR accuracy.

- The generalized extreme value (GEV) distribution provides a suitable fit for  $\beta$  and  $\varepsilon_{HP}$  for the 4 Sept. 2010, 22 Feb. 2011 and 13 June 2011 earthquakes. Statistical analysis using LiDAR-based lateral and vertical displacements during the CES indicates that the GEV may be used as an effective statistical distribution to characterize  $\beta$  and  $\varepsilon_{HP}$ .
- According to statistical analysis of LiDAR ground movements, the 4 Sept. 2010 earthquake was accompanied by the most severe liquefaction-induced ground deformation on a local basis, whereas the 22 Feb. 2011 earthquake was accompanied by the most extensive liquefaction-induced ground deformation and damage to underground infrastructure.
- Liquefaction-induced lateral ground strain and ground angular distortion, interpreted from LiDAR ground movement measurement, are in broad agreement with lateral strains at concrete perimeter footings and differential vertical ground floor displacements, respectively, interpreted from building damage survey data.

This chapter presents a methodology for evaluating liquefaction-induced ground deformations interpreted from LiDAR ground movement data and correlating with building deformation. Suitable statistical models such as the GEV may be used to describe sufficiently LiDAR-based ground deformations, which, in turn, may help in

future investigations to predict building damage and, potentially, to estimate the cost of damage for light timber-framed residential structures.

## REFERENCES

- [5.1] Cubrinovski M, Brendon B, Wotherspoon L, Green R, Bray J, Wood C, Pender M, Allen J, Bradshaw A, Rix G, Taylor M, Robinson K, Henderson D, Giorgini S, Ma K, Winkley A, Zupan J, O'Rourke TD, DePascale G, Wells D. Geotechnical aspects of the 22 February 2011 Christchurch earthquake. *New Zealand Society for Earthquake Engineering Bulletin* 2011; **44**(4):205-226.
- [5.2] Cubrinovski M, Henderson D, Bradley BA. Liquefaction impacts in residential areas in the 2010-2011 Christchurch earthquakes. One Year after 2011 Great East Japan Earthquake. International Symposium on Engineering Lessons Learned from the Giant Earthquake, 2012, Tokyo, Japan.
- [5.3] Oskin ME, Arrowsmith JR, Corona AH, Elliott AJ, Fletcher JM, Fielding EJ, Gold PO, Gonzales-Garcia JJ, Hudnut KW, Liu-Zeng J, Teran, OJ. Near-field deformation from the El Mayor–Cucapah earthquake revealed by differential LIDAR. *Science* 2012; **335**(6069):702-705.
- [5.4] Olsen MJ, Cheung KF, Yamazaki Y, Butcher SM, Garlock M, Yim S, Piakowsky S, Robertson I, Burgos L, Young YL. Damage assessment of the 2010 Chile earthquake and tsunami using ground-based LiDAR. *Earthquake Spectra* 2012; **28**(S1):179-197.
- [5.5] Kayen R, Pack RT, Bay J, Sugimoto S, Tanaka H. Terrestrial-LIDAR visualization of surface and structural deformations of the 2004 Niigata Ken Chuetsu, Japan, earthquake. *Earthquake Spectra* 2006; **22**(S1):147-162.
- [5.6] Chen RF, Chang KJ, Angelier J, Chan YC, Deffontaines B, Lee CT, Lin, ML. Topographical changes revealed by high-resolution airborne LiDAR data: The 1999 Tsaoling landslide induced by the Chi–Chi earthquake. *Engineering Geology* 2006; **88**(3):160-172.
- [5.7] Koarai M, Nakano T, Okatani T, Otoi K, Une H. Liquefaction damage by the 2011 off the Pacific coast of Tohoku Earthquake in Japan and land condition of damaged area detected by time serial geospatial information. *Proceedings of the 26th International Cartographic Conference (ICC)*, 2013, Dresden, Germany.

- [5.8] Duffy B, Quigley M, Barrell DJ, Van Dissen R, Stahl T, Leprince S, McInnes C, Bilderback E. Fault kinematics and surface deformation across a releasing bend during the 2010 MW 7.1 Darfield, New Zealand, earthquake revealed by differential LiDAR and cadastral surveying. *Geological Society of America Bulletin* 2013; **125**(3-4):420-431.
- [5.9] Measures R, Hicks M, Shankar U, Bind J, Arnold J, Zeldis J. Mapping earthquake induced topographical change and liquefaction in the Avon-Heathcote Estuary. *Technical Report No. U11/13*: Environment Canterbury Regional Council, 2013; p. 32.
- [5.10] Tonkin & Taylor Ltd (T&T). Liquefaction vulnerability study. *Report*: Earthquake Commission, 2013 (T&T Ref: 52020.0200/v1.0).
- [5.11] Brideau MA, Massey CI, Archibald G, Jaboyedoff M. Terrestrial photogrammetry and LiDAR investigation of the cliffs associated with the seismically triggered rockfalls during the February and June 2011 Christchurch earthquakes. *Landslides and Engineered Slopes: Protecting Society through Improved Understanding* 2012.
- [5.12] Bowen HJ, Jacka ME, van Ballegooy S, Sinclair, TJE, Cowan HA. Lateral spreading in the Canterbury earthquakes—Observations and empirical prediction methods. *Proceedings of the 15th World Conference on Earthquake Engineering*, 2012, Lisbon, Portugal.
- [5.13] O'Rourke TD, Jeon S-S, Toprak S, Cubrinovski M, Hughes M, van Ballegooy M, Bouziou D. Earthquake response of underground pipeline networks in Christchurch, NZ. *Earthquake Spectra* 2014; **30**(1):183-204.
- [5.14] Henderson DRK. *The Performance of House Foundations in the Canterbury Earthquakes*. M.Eng. Thesis. University of Canterbury: Christchurch, New Zealand, 2013.
- [5.15] Beavan J, Levick S, Lee J JK. Ground displacements and dilatational strains caused by the 2010-2011 Canterbury earthquakes. *GNS Science Consultancy Report 2012/67*, 2012: p. 59.

- [5.16] Canterbury Geotechnical Database. LiDAR and digital elevation models, map layer CGD0500 - 23 July 2012, available at: <https://canterburygeotechnicaldatabase.projectorbit.com/>. [accessed August 2012]
- [5.17] Canterbury Earthquake Recovery Authority (CERA). Verification of LiDAR acquired before and after the Canterbury Earthquake Sequence. *Canterbury Geotechnical Database Technical Specification 03*, 2014.
- [5.18] Hodgson ME, Bresnahan P. Accuracy of Airborne Lidar-Derived Elevation. *Photogrammetric Engineering & Remote Sensing* 2004; **70**(3):331-339.
- [5.19] ArcMap 10.1. Environmental Systems Resource Institute (ESRI): Redlands, California, 2012.
- [5.20] Land Information New Zealand (LINZ). <http://www.linz.govt.nz/>. [accessed March 2013]
- [5.21] Cook RD. *Finite element modeling for stress analysis*. John Wiley and Sons: New York, NY, 1995.
- [5.22] GNS Science. <http://www.gns.cri.nz/>. [accessed 2011].
- [5.23] Wilson, J. *Christchurch: Swamp to city: a short history of the Christchurch Drainage Board, 1875-1989*. Te Waihora Press for the Christchurch Drainage Board: Christchurch, New Zealand, 1989.
- [5.24] Gilli M. An application of extreme value theory for measuring financial risk. *Computational Economics* 2006; **27**(2-3):207-228.
- [5.25] Sinclair CD, Ahmad MI. Location-invariant plotting positions for PWM estimation of the parameters of the GEV distribution. *Journal of Hydrology* 1988; **99**(3):271-279.

- [5.26] Grigoriu M, Samorodnitsky G. Reliability of dynamic systems in random environment by extreme value theory. *Probabilistic Engineering Mechanics* 2014; **38**:54-69.
- [5.27] Canterbury Geotechnical Database. Liquefaction interpreted from aerial photography, map layer CGD0200 - 11 Feb 2013, available at: <https://canterburygeotechnicaldatabase.projectorbit.com/>. [accessed June 2012]
- [5.28] Boscardin MD, Cording EJ. Building response to excavation-induced settlement. *Journal of Geotechnical Engineering* 1989; **115**(1):1-21.
- [5.29] Clough GW, O'Rourke TD. Construction induced movements of in situ walls. *Proceedings of the ASCE Conference on Design and Performance of Earth Retaining Structures*, Geotech. Spec. Publ. No. 25, ASCE, New York, 1990: p. 439–470.

## CHAPTER 6

### CONCLUSIONS AND RECOMMENDATIONS

This thesis deals with earthquake-induced transient and permanent ground deformation and the performance of pipelines and pipeline systems when affected by this type of hazard. Numerical simulations, large-scale experiments, and spatial analysis with Geographic Information Systems (GIS) are used to investigate the seismic performance of pipelines reinforced with in situ polymeric linings; analyze the performance of the Christchurch, NZ, water distribution system in response to the 2010-2011 Canterbury Earthquake Sequence (CES); develop and evaluate a probabilistic approach for characterizing pipeline performance that accounts for orientation within earthquake-induced ground strain fields; and perform a statistical assessment of ground movements measured by high resolution Light Detection and Ranging (LiDAR) surveys during the CES. The main conclusions of this thesis are presented in this chapter and recommendations for future research are discussed in the following sections.

#### **6.1 Seismic Wave Interactions with Buried Pipelines Before and After Rehabilitation With In Situ Linings**

A numerical model was developed to investigate seismic body wave interactions with pipelines with locally weak joints or circumferential cracks. The numerical results

indicate that the most prominent form of deformation caused by seismic wave propagation occurs in the axial pipeline direction. Non-axial deformations have negligible effect on the seismic performance of pipelines before and after rehabilitation and, thus, simplify the problem of seismic wave interaction with pipelines containing round cracks, and segmented pipelines with locally weak joints, by considering only pipeline axial response. Based on these findings, numerical models and experimental design involved in future research may likewise be simplified by focusing on ground movements in the axial pipeline direction.

Numerical analyses and full-scale tests on pipelines with weak joints and circumferential cracks before and after rehabilitation with cast-in-place pipes (CIPP) and CIPP linings show that this type of reinforcement is able to accommodate high intensity ground motions and improve pipeline response to seismic wave interaction. Pipelines retrofitted with two different types of linings, representing relatively rigid and flexible products, were able to sustain substantial seismic velocity pulses. CIPP lining technology, therefore, provides significant benefits for seismic retrofitting in addition to the repair and increased longevity of aging, in situ pipelines, and should be considered in seismic design and retrofit practices.

The numerical models and testing procedures presented in this thesis are for pipelines buried in uniform ground conditions subject to near-source velocity pulses during seismic shear wave propagation. Further research is needed to investigate seismic surface wave (Rayleigh and Love waves) interactions with pipelines crossing

variable ground conditions, including abrupt transitions across soils with large differences in strength and shear stiffness.

Debonding between the lining and pipeline during dynamic testing allows the liner to stretch and accommodate axial movements as long as it is confined locally and does not propagate for long distances between joints. Further experimental and analytical research should focus on the mechanisms that control debonding. The research should investigate pipe cleaning and installation methods that permit separation between the lining and interior pipe surface while restraining it from propagating to service lines and other connections where leakage can occur.

## **6.2 Regression Analysis of Pipeline Damage During the 22 February 2011 Christchurch Earthquake**

Repair rate (repairs/km) regressions were developed for different types of pipelines with respect to: 1) peak ground velocity in areas affected by transient ground deformation (TGD), and 2) lateral ground strain and differential vertical ground movement in areas affected primarily by permanent ground deformations (PGD). Data collected for the 22 February 2011 earthquake in Christchurch, NZ, involve high resolution LiDAR surveys that are used to determine PGD-induced lateral ground strains and differential vertical ground surface movements. In addition, screening criteria are developed in this work for selecting statistically robust data used to

develop linear regressions between pipeline repair rates and various metrics for both TGD and PGD.

The repair regressions indicate that polyvinyl chloride (PVC) pipelines are substantially more resistant to earthquake-induced PGD than asbestos cement (AC) and cast iron (CI) pipelines. Further research is recommended to provide more robust regressions and to extend the databases for such correlations.

Correlations among pipeline repair rates (RR), lateral ground strains, and differential vertical ground surface movements in this work provide the means to predict pipeline damage on the basis of the combined effects of lateral ground strain and differential vertical ground movement. These correlations may be used in future planning, design, and loss estimation to assess limiting deformations for pipelines subjected to both PGD-induced lateral and vertical differential displacements.

The regressions between pipeline repair rates and lateral ground strain, using the 4-m LiDAR measurement spacing are significantly different for AC and PVC pipelines than those previously reported for LiDAR measurements on 56-m spacing. Scale effects have a substantial impact on the inferred relationship between pipeline damage and lateral ground strain, and depend on local variations in the strain field. High resolution LiDAR data are needed to capture the influence of localized ground deformation. Computational modeling that utilizes regressions, such as those of repair rate vs horizontal ground strain, need to account for scale effects, and should strive for

the highest resolution possible at a scale equivalent to that of the structure being investigated.

### **6.3 Probabilistic Approach to Axial Pipeline Strain Caused by Permanent Ground Deformations**

A probabilistic approach was proposed for the assessment of ground strains affecting segmented pipelines. The probabilistic model accounts for pipeline orientation and the relative effects of tension and compression in joint response, and calculates the expected value of the ground strain in the axial pipeline direction. It provides an alternative probabilistic parameter for ground strain effects that can be used in future work for a more comprehensive assessment of lateral ground strains affecting pipelines in large complex networks.

Comparisons between repair regressions pertaining to the 22 February 2011 Christchurch earthquake, NZ, with the expected value of ground strain, and repair regressions with the absolute maximum value of lateral strain, do not show an apparent advantage of the probabilistic approach over the use of the absolute maximum value of ground strain, which is more straightforward and computationally less expensive. The probabilistic model, however, may prove useful in future work related to large and complex pipeline networks and in cases where pipeline orientation with respect to the lateral strain field must be addressed.

The expected value of ground strain also accounts for the relative effects of tension and compression in pipeline joint response through the use of a weighting factor. For the lateral LiDAR measurements and data sets used in this study, AC and CI pipelines are shown to be equally vulnerable to tensile and compressive ground strains.

The absolute value of maximum ground strain is an unbiased indicator with respect to tension and compression and, thus, it is well suited for repair correlations when pipelines have equivalent vulnerability to tensile and compressive ground strains. The use of the absolute maximum value of ground strain is therefore consistent with the equivalent vulnerability of segmental pipelines to tensile and compressive ground strains. This characteristic helps explain similarities in the statistical properties between correlations of pipeline damage with the expected value of ground strain and the absolute maximum value of ground strain.

#### **6.4 Statistical Analysis of Ground Deformations During the 2010-2011 Canterbury Earthquake Sequence**

Statistical analysis of ground deformations caused by liquefaction during the 2010-2011 CES was performed using data collected during LiDAR surveys and provides useful insight into the statistical characteristics of liquefaction-induced ground displacements and deformations within the Christchurch area. The generalized extreme value (GEV) distribution fits favorably the distributions of ground angular distortion and lateral ground strain for the 4 Sept. 2010, 22 Feb. 2011 and 13 June

2011 earthquakes, and may be used in future work as an effective distribution to describe these ground parameters. According to the statistical analysis of LiDAR ground movements, the 4 Sept. 2010 earthquake was accompanied by the most severe liquefaction-induced ground deformation on a local basis, whereas the 22 Feb. 2011 earthquake was accompanied by the most extensive liquefaction-induced ground deformation and damage to underground infrastructure.

The locations of the highest angular distortion (i.e., using the 2.5% exceedance values from the statistical distribution of the data) are in remarkable agreement with locations of existing water courses in Christchurch and provide an accurate measure for identifying all sizes and types of natural water ways and previous meanders within and adjacent to the Avon River flood plain. On the contrary, the highest values of the absolute value of lateral ground strain tend to cluster in small vegetated areas, which detract from LiDAR accuracy.

LiDAR ground measurements can also be used to predict foundation damage due to PGD provided there are adequate LiDAR data with sufficient accuracy. Liquefaction-induced lateral ground strain and angular distortion, interpreted from high resolution LiDAR measurements, are in broad agreement with lateral strain estimated from field investigations of concrete perimeter footings as well as angular distortion determined from optical surveys of differential vertical ground floor displacement. It may be possible in the future, therefore, to correlate lateral ground strain and angular distortion with building deformation such that the correlations on

average will predict building damage, and potentially the cost of that damage, for residential timber-frame structures. It is recommended that further research be conducted on correlating residential building damage and associated costs of repair with lateral ground strains and angular distortion estimated from the LiDAR surveys.

## APPENDIX A

### **Repair Rate (RR) Correlations with the Geometric Mean Peak Ground Velocity (GMPGV)**

The strong motion stations were initially imported and projected in ArcMap, and were subsequently used as input data for the spatial interpolation process. The output of the spatial interpolation process was the GMPGV surface in raster format which was reclassified to intervals of 10 cm/sec and converted to a polygon feature class to allow for spatial correlation with the pipeline network and pipe repairs. The areas of observed liquefaction were imported in ArcMap 10.1 [3.14] and were subsequently expanded by 125 m using the “buffer” tool to account for a zone of influence at the perimeter of the liquefaction areas that affects underground pipelines. Pipelines and repairs were also imported and projected in ArcMap 10.1 [3.14], and their locations were identified with respect to the expanded areas of observed liquefaction. Pipelines and repairs inside these areas were excluded from the analytical process for PGV using the “erase” tool based on the assumption that they were associated with PGD effects. Pipelines affected by landslides and rock falls during the 22 Feb. 2011 earthquake were also removed in a similar manner assuming that pipelines at elevation above 50 m in the Port Hills were primarily affected by widespread PGD. Pipelines and repairs outside the expanded areas of observed liquefaction and at elevation below 50 m were spatially intersected by the GMPGV contour layer using the “intersect” tool

in ArcMap 10.1 [3.14] to correlate them with the estimated GMPGV. Using the spatially located pipelines and repairs, the repair rate (RR) for a given interval of GMPGV was calculated by dividing the number of repairs for a particular type of pipeline by the kilometers of that pipeline type within a contour interval of 10 cm/s. The resulting RR was then associated with a value of GMPGV and was used as a single data point in RR correlations. The screening criteria were applied to produce RR vs GMPGV.

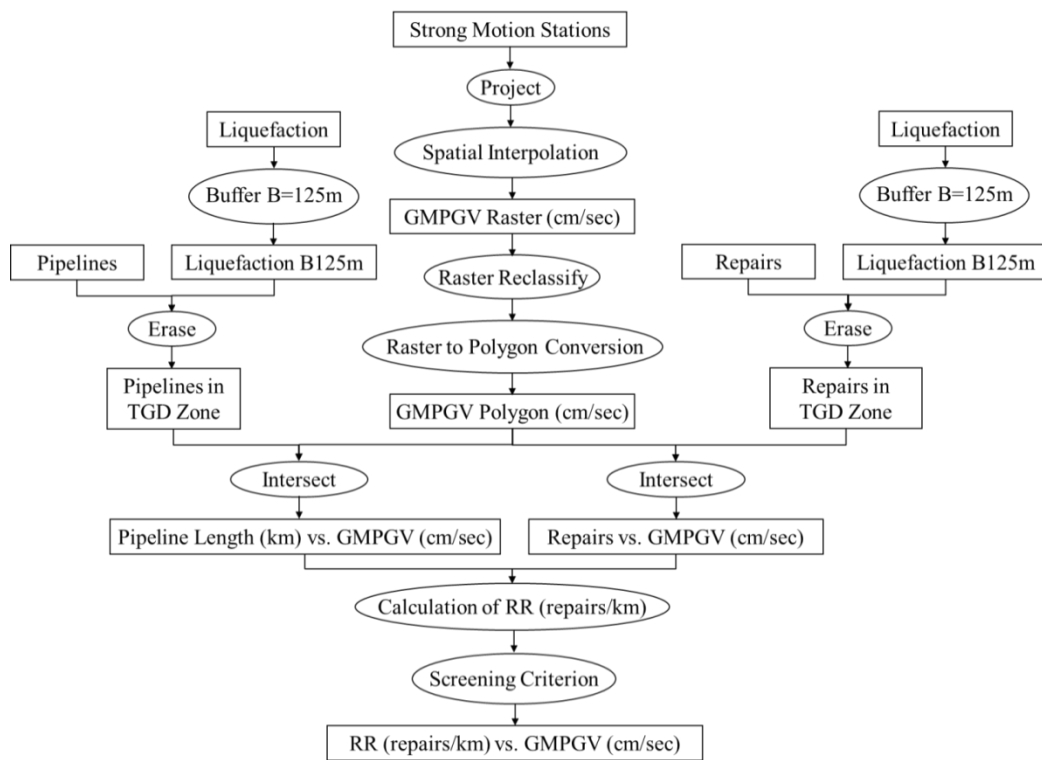


Figure A.1. Flow chart for RR correlation with GMPGV.

## APPENDIX B

### **Repair Rate (RR) Correlations with Ground Angular Distortion $\beta$**

Vertical ground movements derived from LiDAR measurements were imported and projected in the ArcMap 10.1 [3.14] software as raster layers. The LiDAR datasets of vertical movement were large, containing approximately 3 million data points in the LiDAR area and 2.4 million points in the zone of observed liquefaction effects. The process that was followed to calculate angular distortion,  $\beta$ , using this large dataset was successfully performed within the ArcMap 10.1 [3.14] environment.

The “slope” tool in ArcMap 10.1 [3.14] was used to calculate  $\beta$  using the LiDAR data set of vertical movement in the liquefied zone and the output of the process was a surface of values of  $\beta$  in raster format. The raster layer of  $\beta$  was converted into a polygon feature class to allow for spatial correlation with the pipeline network and pipe repairs. The areas of observed liquefaction were buffered by 125 m and pipelines and repairs inside the area of liquefaction were selected using the “clip” tool. Pipelines affected by landslides and rock falls during the 22 Feb. 2011 earthquake were removed in a similar manner. The selected sets of pipelines and repairs inside the areas of liquefaction effects and at elevation below 50 m were spatially intersected by the surface of  $\beta$  layer using the “intersect” tool in ArcMap 10.1 [3.14]. RR for a given interval of  $\beta$  was calculated by dividing the number of repairs for a particular type of pipeline by the kilometers of that pipeline type within the same interval. The interval

size for  $\beta$  was  $1 \times 10^{-3}$ . The calculated RR was associated with the appropriate value of  $\beta$  and was used as a single data point in RR correlations. The screening criteria were applied to produce RR vs  $\beta$ .

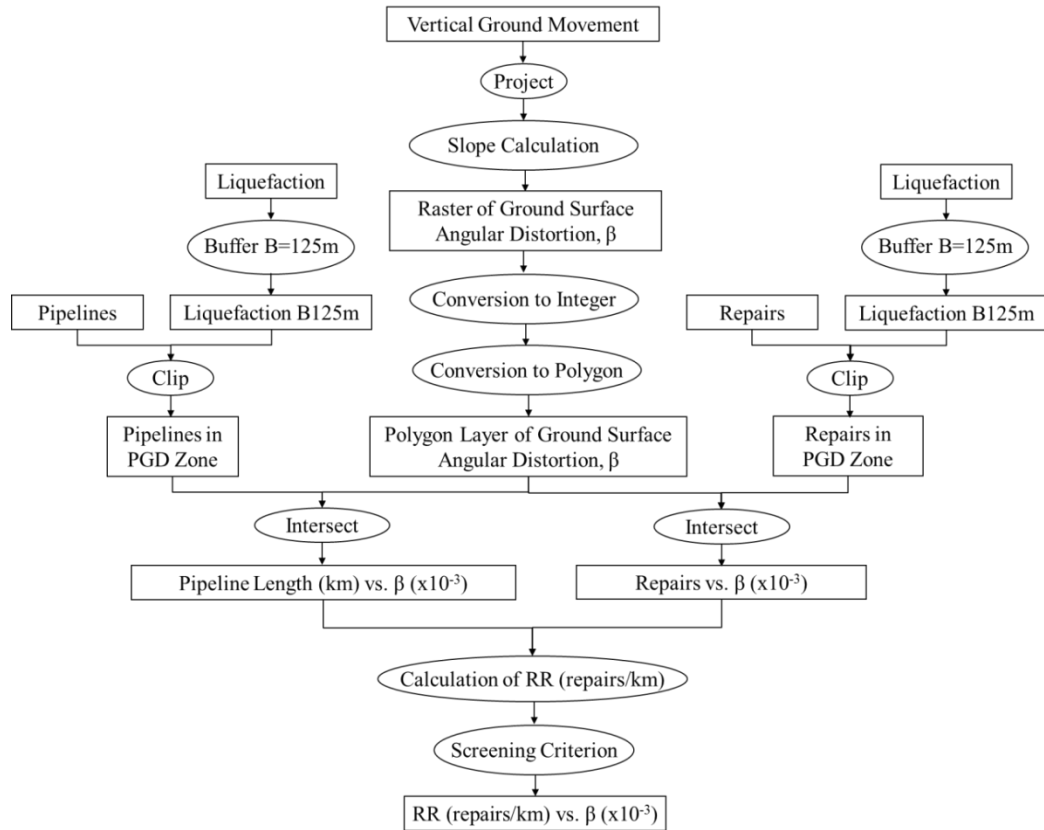


Figure B.1. Flow Chart for RR Correlations with Angular Distortion,  $\beta$ .

## APPENDIX C

### **Repair Rate (RR) Correlations with Lateral Ground Strain $\epsilon_{HP}$**

The lateral ground movements in the EW and NS directions at 4-m and 56-m grid spacing were imported and projected in ArcMap 10.1 [3.14] as raster layers. They were subsequently converted to point layers using the conversion tool in ArcMap 10.1 [3.14] to create lateral displacements at 4-m and 56-m spacing, respectively, in the EW and NS directions. The LiDAR datasets with lateral movements in the EW and NS directions at 4-m grid spacing were large, containing approximately 4.7 million data points in the LiDAR area and 3.7 million points in the zone of observed liquefaction effects. The manipulation of the datasets for calculating lateral ground strains was not possible within the ArcMap 10.1 [3.14] environment due to constraints in the maximum memory usage cap for analysis in ArcMap 10.1. The Manifold® System Release 8 GIS package [3.21] was used to perform subsequent manipulation of the dataset and the Matlab and Statistics Toolbox Release 2012a software [3.22] was used for the calculation of lateral strains.

The data points of lateral displacement at 4-m and 56-m spacing were considered as corner points of two sets of square quadrilateral elements. Using the “create fishnet” tool in ArcMap 10.1 [3.14], point data at 4-m and 56-m spacing were created the centers of the quadrilateral elements in each set. Each element was uniquely identified with an ID in ArcMap 10.1 [3.14]. The Manifold® System Release 8 GIS

package [3.21] was used to correlate each element center point to the appropriate set of four corner points using a structured query language (SQL) statement for each grid size. Spreadsheets of the resulting intersection at 4-m and 56-m spacing were exported to Matlab and Statistics Toolbox Release 2012a software [3.22] for calculation of lateral strains. The calculated lateral strains were imported and projected in ArcMap 10.1 [3.14] in 4 m x 4 m and 56 m x 56 m polygons to allow for spatial correlation with the pipeline network and pipe repairs.

The areas of observed liquefaction were buffered by 125 m and pipelines and repairs inside the area of liquefaction were selected using the “clip” tool. Pipelines affected by landslides and rock falls during the 22 Feb. 2011 earthquake were removed in a similar manner. The selected sets of pipelines and repairs inside the areas of liquefaction effects and at elevation below 50 m were spatially intersected by the surface of  $\varepsilon_{HP}$  layer using the “intersect” tool in ArcMap 10.1 [3.14]. RR for a given interval of  $\varepsilon_{HP}$  was calculated by dividing the number of repairs for a particular type of pipeline by the kilometers of that pipeline type within the same interval. Pipeline sand repairs were initially binned at intervals of  $\varepsilon_{HP}$  equal to 0.05%, and the interval size of  $\varepsilon_{HP}$  was adjusted during the screening process to develop meaningful correlations. The calculated RR was associated with the appropriate value of  $\varepsilon_{HP}$  and was used as a single data point in RR correlations. The screening criteria were applied to produce RR vs  $\varepsilon_{HP}$ .

During the regression analysis, repair data were projected in ArcMap 10.1 [3.14] and their location with respect to adjacent repairs was identified. Repairs at distance less than 6m of each other were assumed to be representative of a single pipe repair, not multiple repairs, and, thus, were reduced to one single repair event.

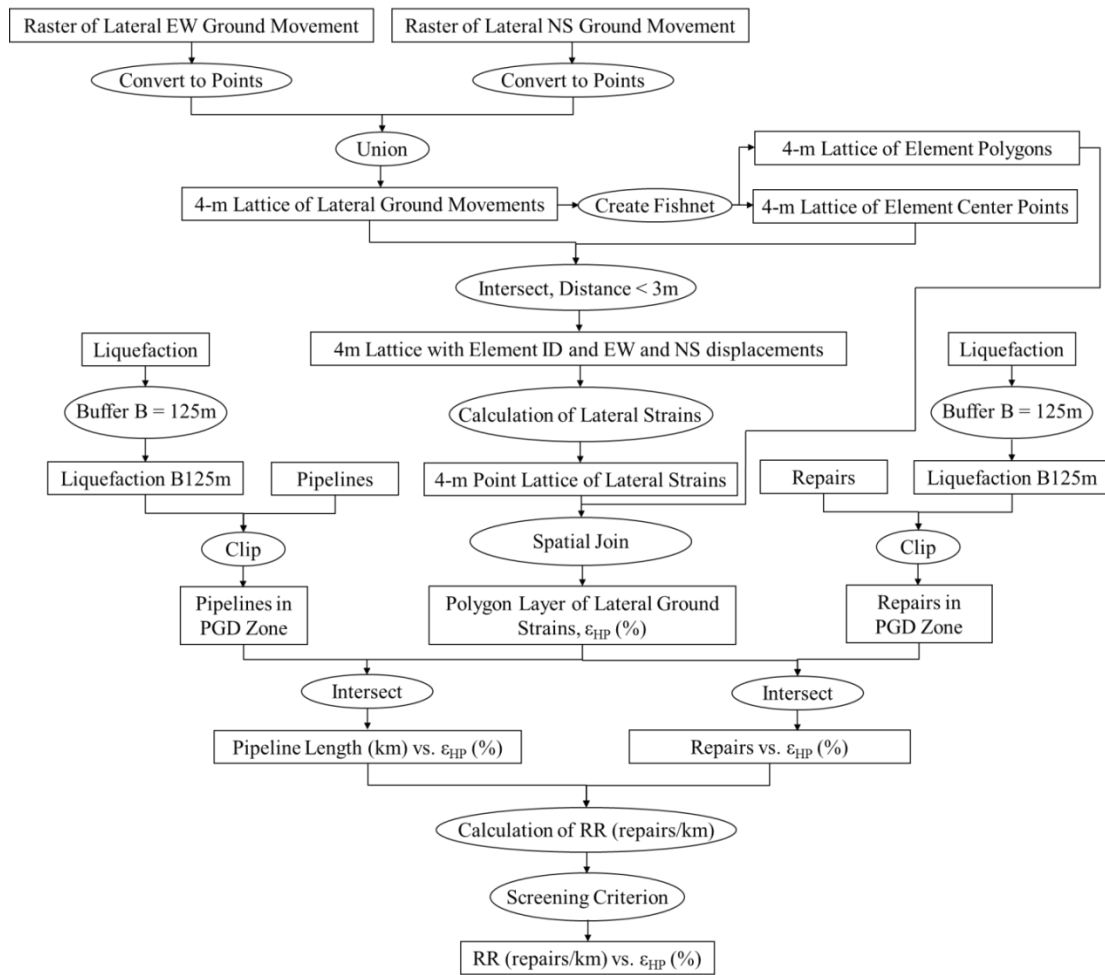


Figure C.1 Flow Chart for RR Correlations with  $\epsilon_{HP}$ .

## APPENDIX D

### **Contour Plots of Differential Vertical Displacement**

As discussed in Chapter 5, measurements of vertical movement on the ground floor level of each building that were collected by Tonkin & Taylor, Ltd., after the 13 June 2011 and before the 23 December 2011 earthquake were used to calculate foundation differential vertical displacements. Each measurement was related to a reference point located near the building entrance. The location of each measurement was recorded on the floor plan of each house and used to develop differential vertical displacement contour plots of the ground floor in each surveyed house.

Contour plots of differential vertical displacement on the ground floor in each surveyed house were developed using the global polynomial interpolation tool in ArcMap 10.1 [5.19]. The contour plots were developed in 10-mm increments. An equivalent floor slope was calculated to represent the predominant ground level slope for each residence based on the contours of differential vertical displacement. The resulting contour plots and equivalent floor slope for each surveyed building are presented below.

#### **D.1. Building No.1**

Building No.1 is a duplex single-story dwelling property located in Shirley. It was constructed after 1980. The building has a slab on grade foundation and unreinforced

brick veneer as exterior cladding. As shown in Figure D.1., the two residences in the duplex property are separated by a central garage.

According to aerial observations of liquefaction, Building No.1 was located in an area that was subjected to minor liquefaction during the 4 Sept. 2010 earthquake, and moderate to severe liquefaction during the 22 Feb. 2011 and 13 June 2011 earthquakes. Minor damage to the exterior cladding and the interior of the two houses was observed during the survey, and the interior floors in both houses were out of level by approximately 110 mm and 148 mm. Settlement was observed at the center of the building at the garage floor where there were also signs of liquefaction ejecta.

The locations of vertical measurements on the building ground floor, the contour plots of differential vertical displacement, and the equivalent floor slope for Building No.1 are presented in Figure D.1.

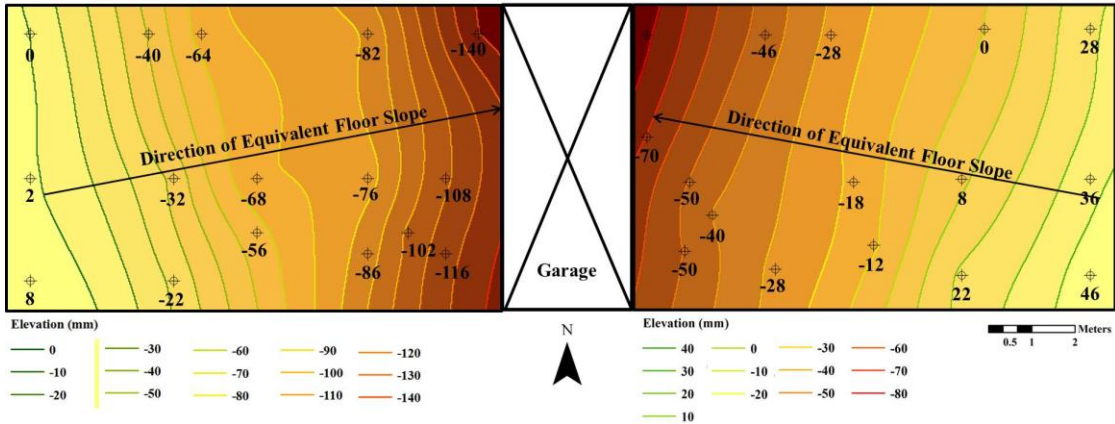


Figure D.1. Contour plots of differential vertical displacement on the ground floor of Building No.1.

## **D.2. Building No.2**

Building No.2 is a single-story dwelling property located in Shirley. It was constructed between 1960 and 1979. The building is supported on short piers and has fiber cement exterior cladding.

According to aerial observations of liquefaction, Building No.2 was located in an area that was not subjected to liquefaction during the 4 Sept. 2010 earthquake, but it was subjected to moderate to severe liquefaction during the 22 Feb. 2011 and 13 June 2011 earthquakes. Extensive cracking in the walls and extensive liquefaction at the east side of the building were observed during the survey. Settlement was concentrated at the northeast corner of the building, the concrete pier at the northeast corner was displaced outwards, and the floor was out of level by approximately 116 mm.

The locations of vertical measurements on the building ground floor, the contour plot of differential vertical displacement, and the equivalent floor slope for Building No.2 are presented in Figure D.2.

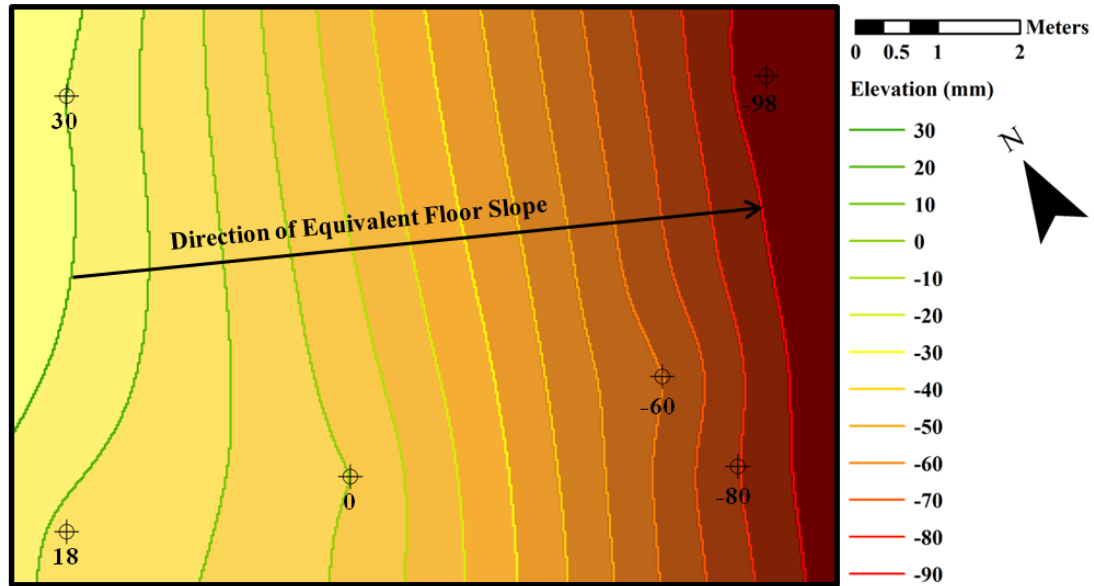


Figure D.2. Contour plots of differential vertical displacement on the ground floor of Building No.2.

### D.3. Building No.3

Building No.3 is a single-story duplex dwelling property located in Shirley. It was constructed between 1960 and 1979. The building is supported on concrete perimeter and has unreinforced brick veneer as exterior cladding. The two houses are separated by a party wall.

According to aerial observations of liquefaction, Building No.3 was located in an area that was not subjected to liquefaction during the 4 Sept. 2010 earthquake, but was subjected to moderate to severe liquefaction during the 22 Feb. 2011 and 13 June 2011 earthquakes. Extensive cracking to the exterior cladding, the interior of the house and the concrete perimeter wall were observed at all sides of the building during the

survey. The floors in the west and east residences were out of level by approximately 50 mm and 86 mm, respectively.

The locations of vertical measurements on the building ground floor, the contour plots of differential vertical displacement, and the equivalent floor slope for Building No.3 are presented in Figure D.3.

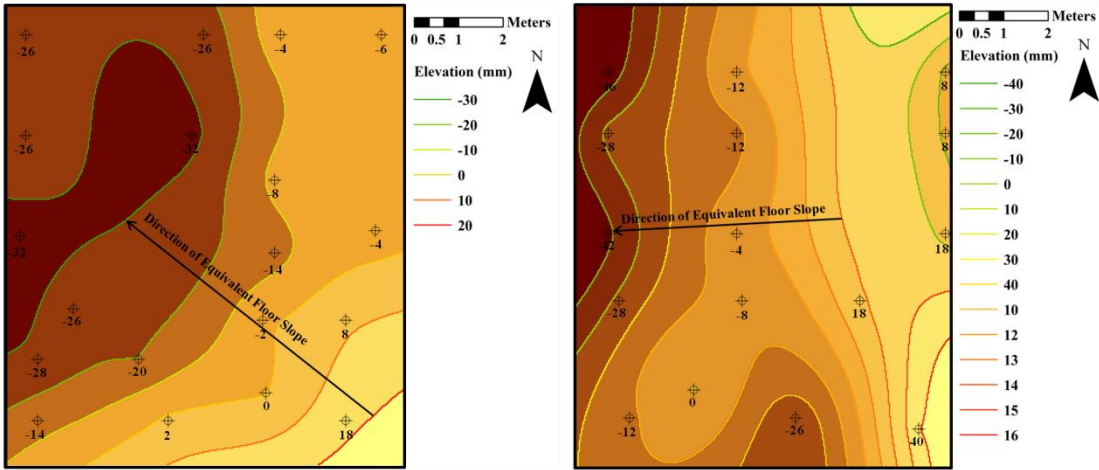


Figure D.3. Contour plots of differential vertical displacement on the ground floor of Building No.3.

**D.4. Building No.4**

Building No.4 is a single-story dwelling property located in Shirley. It was constructed between 1940 and 1959. The building is supported on concrete perimeter and has unreinforced brick veneer as exterior cladding.

According to aerial observations of liquefaction, Building No.4 was located in an area that was not subjected to liquefaction during the 4 Sept. 2010 earthquake, but it was subjected to moderate to severe liquefaction during the 22 Feb. 2011 and 13 June

2011 earthquakes. Liquefaction was observed at the east and northeast side of the building. The building was subjected to severe lateral spreading during the 22 Feb. 2011 earthquake, resulting in extensive cracking to the exterior cladding on the north and the south walls, the interior of the house and the concrete perimeter wall. The ground floor was out of level by approximately 114 mm.

The locations of vertical measurements on the building ground floor, the contour plot of differential vertical displacement, and the equivalent floor slope for Building No.4 are presented in Figure D.4.

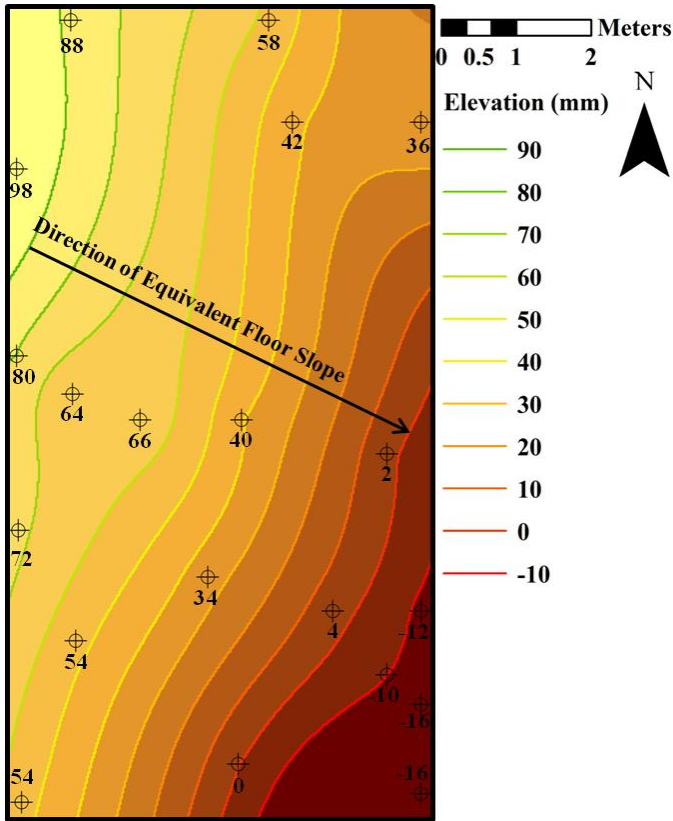


Figure D.4. Contour plots of differential vertical displacement on the ground floor of Building No.4.

### **D.5. Building No.5**

Building No.5 is a two-story duplex dwelling property located in Shirley. It was constructed between 1960 and 1979. The building is supported on short piers with timber cladding foundation walls and a concrete and masonry perimeter footing. The two residences are separated by a party wall.

According to aerial observations of liquefaction, Building No.5 was located in an area that was not subjected to liquefaction during the 4 Sept. 2010 earthquake, but was subjected to moderate to severe liquefaction during the 22 Feb. 2011 and 13 June 2011 earthquakes. Extensive cracking was observed at all sides of the concrete perimeter footing, with settlement of the party wall. There were multiple areas of exterior cladding with cracks, and there were signs of minor liquefaction at the subfloor. The ground floors of the west and east residences were out of level by approximately 94 mm and 60 mm, respectively.

The locations of vertical measurements on the building ground floor, the contour plots of differential vertical displacement, and the equivalent floor slope for Building No.5 are presented in Figure D.5.

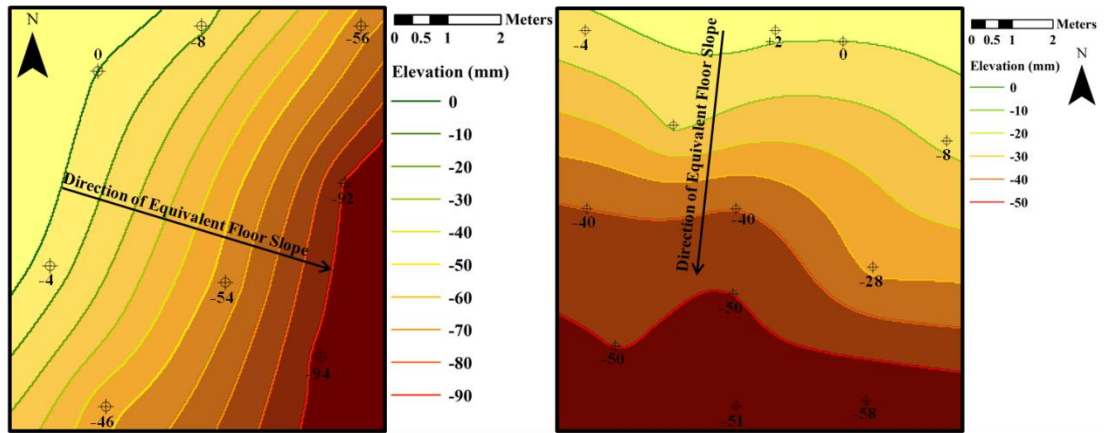


Figure D.5. Contour plots of differential vertical displacement on the ground floor of Building No.5.